Towards Room-Temperature deterministic ferroelectric control of ferromagnetic thin films

THÈSE N^{O} 6904 (2015)

PRÉSENTÉE LE 17 DÉCEMBRE 2015
À LA FACULTÉ DES SCIENCES ET TECHNIQUES DE L'INGÉNIEUR
LABORATOIRE DE CÉRAMIQUE
PROGRAMME DOCTORAL EN SCIENCE ET GÉNIE DES MATÉRIAUX

ÉCOLE POLYTECHNIQUE FÉDÉRALE DE LAUSANNE

POUR L'OBTENTION DU GRADE DE DOCTEUR ÈS SCIENCES

PAR

Zhen HUANG

acceptée sur proposition du jury:

Prof. W. Curtin, président du jury
Dr I. Stolichnov, Prof. N. Setter, directeurs de thèse
Prof. J. Petzelt, rapporteur
Dr R. Gysel, rapporteur
Prof. J.-Ph. Ansermet, rapporteur

ÉCOLE POLYTECHNIQUE
FÉDÉRALE DE LAUSANNE

Suisse
2015

Abstract

The persisting demand of higher computing power and faster information processing keeps pushing scientists and engineers to explore novel materials and device structures. Within emerging functional materials, there is a focus on multiferroics materials and material-systems possessing both ferroelectric and ferromagnetic orders. Multiferroics with two order parameters coupled through a magnetoelectric interaction are of particular interest for novel information processing technologies. This thesis explores a promising concept of magnetoelectric multiferroic heterostructure incorporating separate ferroelectric and ferromagnetic thin layers with field-effect-mediated coupling through the heterointerface.

The major issues related to ferroelectric control of ferromagnetism in multiferroic heterostructures addressed in this thesis include non-volatile magnetoelectric coupling at room temperature, deterministic switching of magnetization via polarization reversal, ferroelectric control of dynamics of magnetic domains and integration of ferroelectric gates on magnetic channels.

The major accomplishments of this thesis are the following:

- Non-volatile ferroelectric control of magnetic properties has been demonstrated in ultra-thin Co layers at room temperature. The ferromagnetic transition Curie temperature, magnetic anisotropy energy and magnetic coercivity are shown to be switchable via the persistent field effect associated with the ferroelectric polarization. The magnitude of the effect is comparable or exceeds the results observed using the conventional (non-ferroelectric) gates.

- Local control of individual magnetic domain nucleation and propagation in Co channels by creating new ferroelectric domains has been achieved at the ambient conditions. The microscopic ferroelectric domains written on poly(vinylidene fluoride-trifluoroethylene) [P(VDF-TrFE)] ferroelectric polymer gate projected onto the magnetic channel changing locally the magnetic anisotropy energy, and consequently altering magnetic domain dynamics. Therefore it was possible to promote/impede magnetic domain nucleation and significantly change the domain wall velocity using a non-destructive and reversible procedure of ferroelectric domain writing.

- Non-volatile control of anisotropic magnetoresistance (AMR) has been demonstrated on diluted magnetic semiconductor (Ga,Mn)(As,P) thin films with integrated P(VDF-TrFE) ferroelectric gate. The field effect induced by the ferroelectric gate has shown the capability to strongly modulate the

AMR behavior. Profound qualitative changes of the nature of AMR has been observed, including complete on/off switching of the crystalline component of AMR in (Ga,Mn)(As,P).

- A workflow for fabrication of integrated FET-type structures comprising a magnetic metal or semiconductor magnetic channel and ferroelectric polymer gate has been successfully developed. Different approaches for enhancement of ferroelectric gate operation were explored including integration of highly resistive hydrophobic interfacial layer and change of polymer composition for lower leakage. A significant increase of the non-volatile gate effect magnitude compared to the state of art was reached via improved quality of the ferroelectric/ferromagnetic interface.

Keywords: Multiferroics, Ferroelectricity, Ferromagnetism, magnetoelectric coupling, FeFET, P(VDF-TrFE), (Ga,Mn)As, ultra-thin Co film, anisotropy, domain kinetics.

Résumé

La demande persistante d’une puissance de calcul plus élevée et le traitement plus rapide de l'information continuent à pousser les scientifiques et ingénieurs à explorer de nouveaux matériaux et structures. Au sein de ces nouveaux matériaux fonctionnels, l’accent est mis sur les matériaux multiferroïques et les systèmes matériau possédant deux paramètres d’ordre, ferroélectriques et ferromagnétiques. Les multiferroïques avec ces paramètres d’ordre couplés à travers une interaction magnétoélectrique ont un intérêt particulier pour les nouvelles technologies informatiques. Cette thèse étudie le concept prometteur d'hétéro structures magnétoélectriques multiferroïques incorporant des couches minces ferroélectriques et ferromagnétiques distinctes couplées par effet de champ.

Les grandes questions ayant trait au contrôle ferroélectrique du ferromagnétisme dans les hétérostructures multiferroïques abordées dans cette thèse incluent le couplage magnétoélectrique non volatile à température ambiante, le renversement déterministe de l'aimantation par l’inversion de polarisation ferroélectrique, le contrôle ferroélectrique de la dynamique des domaines magnétiques et l’intégration de grilles ferroélectriques sur des canaux magnétiques.

Les principales réalisations de cette thèse sont les suivantes

- Le contrôle ferroélectrique non-volatile des propriétés magnétiques a été démontré dans des couches ultra-minces de Co à température ambiante. La température de Curie de transition ferromagnétique, l'énergie d'anisotropie magnétique et la coercivité magnétique semblent être modifiables via l'effet de champ persistant associé à la polarisation ferroélectrique. L'amplitude de l'effet est comparable ou supérieur aux résultats observés à l'aide de grilles conventionnelles (non-ferroélectriques).

- Le contrôle local de la nucléation et de la propagation de domaine magnétique individuel dans les canaux de Co en créant de nouveaux domaines ferroélectriques a été démontré en condition ambiante. Les domaines ferroélectriques microscopiques écrits sur la grille à base du polymère ferroélectrique poly(fluorure de vinylidène-trifluoroéthylène) [P(VDF-TrFE)] changent localement l'énergie d'anisotropie magnétique dans le canal magnétique et par conséquent altère la dynamique de domaines magnétiques. Il fut donc possible de promouvoir/entraver la nucléation de domaines magnétiques et changer de façon significative la vitesse de paroi de domaine à l'aide d'une procédure d’écriture non-destructive et réversible de domaine ferroélectrique.

- Le contrôle non-volatile de la magnétorésistance anisotrope (AMR) a été démontrée dans des semi-conducteurs magnétiques dilués (Ga,Mn)(As,P) en couche mince avec P(VDF-TrFE) comme grille ferroélectrique. L'effet de champ induit par la grille ferroélectrique a démontré la capacité de moduler fortement le comportement de l'AMR. D'importants changements qualitatifs sur la nature de l'AMR a été observée, y compris une commutation ON/OFF complète de la composante cristalline de l'AMR dans les films de (Ga,Mn)(As,P).
- Un flux de travail pour la fabrication de structures de FET-type comprenant comme canal un métal magnétique ou un semi-conducteur magnétique et une grille polymère ferroélectrique a été développé avec succès. Des approches différentes pour l'amélioration du fonctionnement de la grille ferroélectrique ont été explorées notamment l'intégration de couche d'interface hydrophobe très résistive ou le changement de composition du polymère d'étanchéité inférieure. Une augmentation significative de l'amplitude de l'effet de la grille non-volatile par rapport à l'état de l'art a été atteint par l'amélioration de la qualité de l'interface ferroélectrique/ferromagnétique.

Mots clés: Multiferroïque, ferroélectricité, ferromagnétisme, couplage magnéto-électrique, FeFET, P(VDF-TrFE), (Ga,Mn)As, film de Co ultra-mince, anisotropie, cinétique de domaine.

Contents

Preface

Motivation of the research

In the field of novel functional materials for future information processing technologies, multiferroics attract much attention promising innovative device concepts. Multiferroics possessing two coupled ferroic orders, which are in the most important cases ferroelectric and ferromagnetic arrangements, can be classified as single phase or composite systems. Most research efforts have been focused on single phase multiferroics; however, the progress in the field was impeded by the weakness of the multiferroic coupling, the very limited number of suitable materials and the very difficult integration with semiconductor technology. In composite multiferroics, which consist of two or more separate phases possessing ferroelectricity or ferromagnetism, the multiferroic coupling requires an interaction across the interface between the different phases. There have been extensive studies exploring the strain-induced coupling that relies on the piezoelectric effect and magnetostriction. This approach has been efficient in development of magnetoelectric sensors, however in thin film geometry, which is preferred for memory and logic devices, mechanical clamping of the film to the substrate limits the magnetostrictive coupling effect. This constraint is avoided in another class of multiferroic structures which relied on electric-field mediated coupling. In general these structures can be implemented based on the field effect transistor (FET) architecture, which offers an advantage of close compatibility with CMOS circuitry.

The materials choice for multiferroic heterostructures with field-effect-mediated coupling is mainly dictated by the processing compatibility between the ferroelectric and ferromagnetic components. In the FET-like architecture, the ferromagnetic part forms a channel while the ferroelectric plays role of a gate that induces the non-volatile field effect. Ferroelectric control of ferromagnetism using such a structure has been successfully demonstrated in a series of works using diluted magnetic semiconductor (Ga,Mn)As channel combined with the ferroelectric polymer P(VDF-TrFE) gate. It was shown that the strength of the ferromagnetic interaction, ferromagnetic Curie temperature and magnetotransport can be tuned via non-volatile change of hole concentration in the channel by reversing the spontaneous polarization of the gate.

On the other hand, the general drawback of diluted magnetic semiconductors is very low ferromagnetic Curie temperature always residing within cryogenic range. Therefore, in order to reach field-effect control of ferromagnetism at ambient conditions; metallic magnetic channels with a high Curie temperature are required. First reports of modulating magnetism in such channels using conventional (non-ferroelectric) gates suggested that such control was possible. However there are major issues involving fundamentals of multiferroic coupling and materials integration that need to be addressed in order to reach strong ferroelectric control of ferromagnetism at ambient conditions.

Goal of the thesis

The scope of this thesis is to explore magneto-electric coupling in multiferroic heterostructures and identify physical mechanisms suitable for strong, ideally deterministic change of the magnetic state in response to polarization reversal. The major goal is to achieve such a strong coupling at room temperature by implementing a heterostructure that combines an ultra-thin metal channel and a ferroelectric polymer gate. The other focus is to demonstrate and explore the local character of the interplay between the individual ferroelectric and ferromagnetic domains and control ferromagnetism locally by individual polarization domain writing.

Thesis outline

Understanding multiferroic heterostructures requires an insight in both fields of ferroelectricity and ferromagnetism, which are separately addressed in Chapters 1 and 2 respectively. Chapter 1 begins with an overview of basics of ferroelectricity, then the focus is shifted on ferroelectric copolymers used as a gate material in this study. The chapter is concluded by analysis of the ferroelectric gate concept and the most important phenomena determining the ferroelectric gate performance.

Chapter 2 is an introduction into ferromagnetic materials suitable for multiferroic FET applications. This part starts with a discussion of fundamentals of ferromagnetism, including magnetic domains and anisotropy. The magnetic properties of the chosen materials: (Ga,Mn)As and Co in the thin film form, are presented in the context of possible FET applications. Then a review of field effect control of magnetic thin film channels describes the development in the field from first proof-of-concept experiments to more advanced non-volatile ferroelectric gate devices.

Chapter 3 addresses characterization methods and multiferroic device fabrication workflows. The techniques to probe and interpret ferroelectric polarization behavior, magnetization strength and the reversing magnetic domains are discussed. The fabrication of device prototypes and integration of ferroelectric gate is described. Different approaches for ferroelectric gate enhancement are discussed and examined experimentally.

Chapters 4-6 contain the main body of experimental results of this thesis. Chapter 4 is dedicated to anisotropic magnetoresistance (AMR) in (Ga,Mn)(As,P) channel. Among other results, we demonstrate the deterministic control of the crystalline component of AMR via reversing ferroelectric polarization.

Chapter 5 addresses the magnetotransport behavior in ultra-thin cobalt film under ferroelectric control at room temperature. The macroscopic characterization using magnetotransport methods clearly demonstrates the non-volatile change of the magnetic states at the room temperature.

Magnetic domain behavior under ferroelectric control is explored in Chapter 6. We analyze the magnetic domain nucleation and growth in relationship with local reversal of ferroelectric domains. Combining magneto-optical, magneto-electrical and scanning probe techniques, we gain an insight into the ferroelectric control of individual magnetic domains in the ultra-thin cobalt channel at the ambient conditions.

Chapter 1
Ferroelectric materials and their application in field effect devices

In this first chapter, ferroelectricity and ferroelectric materials are introduced. The chapter begins with overview on basic phenomena in ferroelectricity with attention to issues relevant to the thesis. After a general introduction to ferroelectric materials, the discussion is focused on ferroelectric copolymers, PVDF & P(VDF-TrFE), the gate materials used for the research. The chapter concludes by analysis of the ferroelectric gate concept and the most important phenomena determining the ferroelectric gate performance.

1.1 Ferroelectricity

1.1.1 Historical background

Since a century, ferroelectric materials have attracted interest of scientists and engineers due to their useful properties for applications. Besides the high dielectric constant ε, ideal for large capacitors, ferroelectrics convert mechanical energy into electric form through piezoelectricity (derived from the Greek word “piezein” meaning press). They possess also the capacity to convert a thermal signal, as a temperature change, to an electric signal via pyroelectricity (derived from the Greek word “pyr” meaning fire).

The brothers Pierre and Jacques Curie demonstrated piezoelectricity in Rochelle salt in 1880.[1] After almost another half of century, ferroelectricity, named in analogy to iron and ferromagnetism, was discovered by J. Valasek in Rochelle salt at 1921.[2] Another quarter century passed until $BaTiO_3$, probably the most studied ferroelectric perovskite, was revealed around 1945.[3] In 1971 ferroelectricity was found in an organic polymer named PVDF (polyvinylidene fluoride) which is still the star in the realm of organic ferroelectrics.[4]

With the growing experience in material preparation, high quality ferroelectrics entered applications. Besides applications based on their natural piezoelectricity and pyroelectricity, ferroelectrics were predicted to be useful for logic and memory devices. This idea started to be realized by J. Anderson at 1952[5] and continued since then.

1.1.2 Ferroelectricity and its origin

Ferroelectricity is characterized by a spontaneous electric polarization in absence of an applied electric field which can be reversed by the application of a reasonable electric field.[2] The customary "reversal definition" emphasizes two important features of ferroelectricity. First, it stresses the fact that ferroelectric materials can exist in at least two stable states of spontaneous polarization, implying the existence of domains (section 1.1.5). Secondly, it points out the essential fact that the magnitude and direction of the spontaneous polarization can be determined by measuring the charge during the switching, i.e., by integrating the electric current with time, when the direction of polarization is changed by external fields.

Beyond the "reversal definition" of ferroelectricity, there are two supplementary issues. Firstly, the symmetry requirements on a given ferroelectric may not allow for 180° reversibility of polarization, i.e. for the change of its sign; rather the polarization can exist in several directions which need not include antiparallel pairs of polarization vectors. This issue can be corrected through replacing "reversibility" by "reorientability". Furthermore, for a particular material under given conditions, the experimentalist may not be able to measure the change of polarization direction (e.g. due to a high electrical conductivity) while the material is still a true ferroelectric. Thus, another definition of ferroelectricity based on pyroelectric effect:[6]

Ferroelectrics are materials that undergo a phase transition from a high symmetry non-polar phase into a lower symmetry polar phase. [*A polar material is a material which has non-zero vector components of its pyroelectric coefficients.*]

From this definition, the spontaneous polarization P_s is determined by the integration of pyroelectric coefficient p:

$$P_s(T_f) = \int_{T_p}^{T_f} p(T)\,dT \tag{1.1}$$

where T_f is the temperature in ferroelectric phase and T_p for a temperature in paraelectric phase. Thus in principle, in the ferroelectric phase, the switching is defined by the direction change of the vector $\boldsymbol{p}$ by application of an electric field pulse or mechanical stress while the absolute value of $\boldsymbol{p}$ being unchanged.

To understand the occurrence of ferroelectricity, the Slater model[7] was developed to explain the so-called polarization catastrophe in ferroelectric materials e.g. in $BaTiO_3$. The model suggested that long range repulsive dipolar forces are canceled by short range local attractive forces. The phenomenology was based on the energy expansion that includes terms proportional to x^2 and x^4, where x stands for the ion displacement from its central position. When external electric field is applied on the material, the local electric field E_{local} at the atoms generates microscopic dipoles and polarization P. To examine the exact strength of E_{local} inside the medium, several contributions are taken into account:

- E_0: the field produced by a fixed charge external to the body;
- E_1: the depolarization field from the surface charge on the surface of the material;
- E_2: Lorentz cavity field, i.e. the field from the polarization charges from a spherical cavity cut in the material with the target atom as center;
- E_3: field from atoms inside the cavity.

Hence E_{local} is the sum of the four listed fields. The calculation in the model concludes the relation among E_{local}, P and the macroscopic field E:

$$E_{local} = E + \frac{P}{3\varepsilon_0} \tag{1.2}$$

Meanwhile combining with the proportional relation of $P=\alpha E_{local}$ we can conclude that the ratio between E and P:

$$\frac{E}{P} \to 0,\ \text{when}\ \alpha = 3\varepsilon_0 \tag{1.3}$$

namely the existence of the spontaneous polarization with zero electric field. In a more comprehensive way, the polarization in the material increases faster than the elastic restoring force in the crystal, leading to asymmetric displacement of the ions and resulting in emergence of spontaneous polarization.

Another interpretation of the origin in ferroelectricity is from the direct observation from ferroelectric crystal lattice. For the common perovskite ferroelectrics ABO_3, at high temperature, the crystal is in the cubic paraelectric phase in which the B cation stays at the center of the cubic unit cell, A cation at the corner positions and O^{2-} anions at the center of each face. The symmetric ion configuration results in zero dipole. In the tetragonal phase, the B cation is free to move off-center with six stable positions slightly displaced from the symmetric body center. This is called B-site driven generation of spontaneous polarization, presented in many perovskite ceramics such as $BaTiO_3$. In the notable exception of $PbTiO_3$, the off-centered Ti atom and the Pb are both displaced strongly in the same direction with respect to the oxygen octahedron, yielding an even stronger electric dipole.

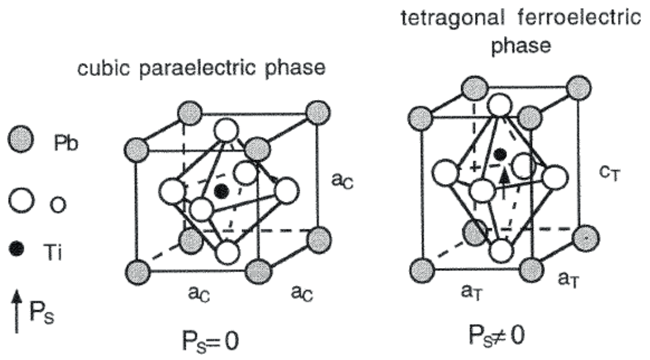

Figure 1.1: The structure of perovskite ferroelectrics, showing the cubic structure in the paraelectric phase and tetragonal structure in the ferroelectric phase. Adopted from Ref.8.

The origin of ferroelectricity described above is suitable for materials in which the ferroelectric phase transition is a *displacive* type, which can be summarized as that the atoms controlling the symmetry change at the phase transition perform small harmonic oscillations around their average positions.[6] Another origin drives ferroelectricity in ferroelectrics with *order-disorder* phase transition. The order-disorder ferroelectrics contain the atoms controlling the symmetry performing thermally activated hopping between several equilibrium positions. In this case, the phases are divided by the distribution of the atoms between these positions: in the non-ferroelectric phase the atoms are equally distributed between them, whereas in the ferroelectric phase, this distribution becomes asymmetric resulting in a displacement of the average positions of atoms.[6] The order-disorder class includes crystals with hydrogen bonds, as potassium dihydrogen phosphate (KH_2PO_4, or KDP in short). In KDP crystal, the motion of protons (H^+) contributes to the ferroelectricity.

Not restricted to inorganic materials, ferroelectricity has been discovered also in many organic materials. The origin of ferroelectricity in organics is classified as order-disorder system, mainly resulting from molecular dipoles and hydrogen bonds. Inside polymers such as PVDF or single molecules such as thiourea, the permanent molecular dipoles, which are ordered without cancelling each other out can generate spontaneous polarization in the ferroelectric phase, whereas the disordered orientations of dipoles exist in the paraelectric phase. The structural symmetry allows arrangement of the intrinsic dipoles in more than one stable alignment and the observation of polarization reversal.[9] A detailed discussion of the ferroelectric polymer PVDF is included in section 1.2.

Another important case of ferroelectricity occurs when dynamic protons on hydrogen bonds trigger the ferroelectric order in the materials.[10] A typical example is the diazabicyclo[2.2.2] octane (dabco) salts with inorganic tetrahedral anions, as the molecule alignment shown in Figure 1.2(b). Through the $N\text{-}H^+\cdots N$ bonds the monovalent (H-dabco)$^+$ cations are linked linearly between the basic nitrogen and its conjugate acid form, which align the spontaneous polarization along the axial direction. The cation chain obtains bistable orientations, which can undergo polarization reversal by a collective proton-transfer process.

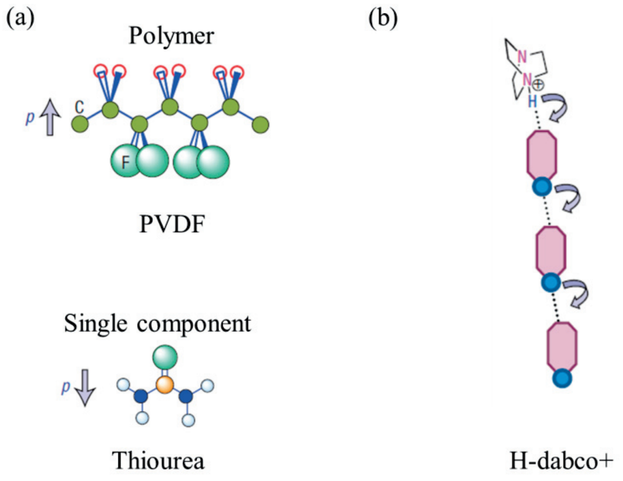

Figure 1.2: Conventional organic ferroelectrics: (a) up: the polymer PVDF in ferroelectric phase, down: single polar molecule thiourea $SC(NH_2)_2$; (b) Linear linked (H-dabco)$^+$ cations through hydrogen bonds.[11]

1.1.3 Phase transition between ferro-/para-electric phases

The thermodynamic potential is used as a phenomenological approach to describe a stimulus and its response with adequate variables of the material. By means of thermodynamics, the coupling of different properties in ferroelectrics can be expressed. This treatment is named after its founders: Landau-Ginzburg-Devonshire (LGD).[12,13,14]

The change of the internal energy dU due to the external stimulus to the system, i.e. due to the changes of the strain dx_{ij}, the dielectric displacement dD_i, and the entropy dS can be written as:

$$dU = T\,dS + X_{ij}\,dx_{ij} + E_i dD_i \tag{1.4}$$

with the temperature T, the stress X_{ij} , and the electric field E_i.

In the practical study, the Gibbs free energy potential is a more convenient thermodynamic potential for many experimental situations. It reads:

$$dG = -S\,dT - x_{ij}\,dX_{ij} + E_i dP_i \tag{1.5}$$

with the polarization P_i. Based on the work for $PbTiO_3$ as a tetragonal lattice,[15] we can expand the Gibbs function ΔG:

$$\begin{aligned}\Delta G &= a_1(P_1^2+P_2^2+P_3^2)+a_{11}(P_1^4+P_2^4+P_3^4)\\ &+a_{12}(P_1^2P_2^2+P_2^2P_3^2+P_3^2P_1^2)+a_{111}(P_1^6+P_2^6+P_3^6)\\ &+a_{112}[P_1^4(P_2^2+P_3^2)+P_2^4(P_3^2+P_1^2)+P_3^4(P_1^2+P_2^2)]+a_{123}(P_1^2P_2^2P_3^2)\\ &-\frac{1}{2}s_{11}(X_1^2+X_2^2+X_3^2)-s_{12}(X_1X_2+X_2X_3+X_3X_1)\\ &-\frac{1}{2}s_{44}(X_4^2+X_5^2+X_6^2)-Q_{11}(X_1P_1^2+X_2P_2^2+X_3P_3^2)\\ &-Q_{12}[X_1(P_2^2+P_3^2)+X_2(P_3^2+P_1^2)+X_3(P_1^2+P_2^2)]\\ &-2Q_{44}(X_4P_2P_3+X_5P_3P_1+X_6P_1P_2)\end{aligned} \tag{1.6}$$

where a_i, a_{ij}, and a_{ijk} are the dielectric stiffness and higher-order stiffness coefficients under constant stress, s_{ij} the elastic compliance coefficient at constant polarization, and Q_{ij} the cubic electrostrictive constant in polarization notation.

Most materials exist in different phases at different environments, determined by the minima of their thermodynamic potential. The phase transition can occur in a continuous or discontinuous way, described by the behavior of the global minimum of the Gibbs free energy potential ΔG introduced in equation (1.6).

To study the phase transition between cubic ($P_1=P_2=P_3=0$) and tetragonal ($P_1=P_2=0$, $P_3\neq 0$) in i.e. $BaTiO_3$ and $PbTiO_3$, the potential ΔG of a mechanically free sample can be reduced to:

$$\Delta G = \frac{1}{2}\alpha_1P_3^2+\frac{1}{4}\alpha_2P_3^4+\frac{1}{6}\alpha_3P_3^6 \tag{1.7}$$

with the coefficients $\alpha_1=2a_1$, $\alpha_2=4a_{11}$, and $\alpha_3=6a_{111}$, which are in general temperature dependent. For stability reasons with increasing P_3, the condition $\alpha_3>0$ is required. With different sign of the coefficients α_1 and α_2, there would be first-order or second-order phase transition appearing during the evolution of the potential minima. Simple examples of second-order and first-order transition are discussed below by assuming α_2 independent of the temperature.

Second-order ferroelectric phase transition

Differentiating the Gibbs potential (equation (1.7)) with respect to P at a constant temperature, $E=(\partial\Delta G/\partial P)_T$ generates the dielectric equation of state:

$$E=\alpha_1P+\alpha_2P^3+\alpha_3P^5 \tag{1.8}$$

where E is the electric field parallel to P. With the coefficient $\alpha_2>0$, the curves for equation (1.7) for ΔG vs. P are sketched in Figure 1.3. When the coefficient α_1 is positive, the potential curve has a single minimum at $P=0$; but the negative coefficient α_1 gives a double-minimum curve at non-zero P values.

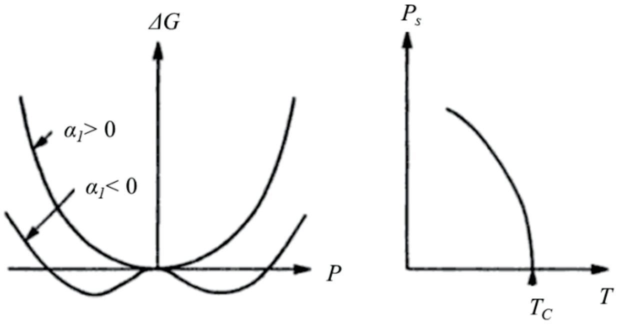

(a) (b)

Figure 1.3: Qualitative temperature dependence of the curves for ΔG vs. P (a) and of the spontaneous polarization P_s (b) near a second-order ferroelectric phase transition. The parameter α_1 is proportional to T-T_C.[12]

In the equation (1.8), α_1 can be considered as the reciprocal permittivity of zero-field displacement at the non-polar phase. Conventional phenomenological theory[13,14] assumes a linear dependence of the parameter α_1 on the temperature, with a positive constant β. This leads to the well-known Curie-Weiss law for $T>T_C$:

$$\alpha_1 = \kappa^{\chi,T>T_C} = \frac{1}{\varepsilon_0 \varepsilon} = \beta(T - T_C) \tag{1.9}$$

where ε_0 is the vacuum permittivity and ε the dielectric constant of the material in the paraelectric phase.

If α_2 is positive, nothing new is added by the term in α_3, and this may then be neglected. With E=0 for the criteria of the equilibrium states of zero electric field, we can derivative from equation (1.8):

$$\beta(T - T_C)P_s + \alpha_2 P_s^3 = 0 \tag{1.10}$$

So either P_s=0 or $|P_s|=[\beta(T_C-T)/\alpha_2]^{1/2}$. For $T \geq T_C$, the only real solution of equation (1.10) is P_s=0, since β and α_2 are positive. For $T<T_C$, the minima of the Landau potential are at:

$$|P_s| = \sqrt{\frac{\beta(T_C - T)}{\alpha_2}} \tag{1.11}$$

as plotted in Figure 1.3(b). This equation predicts that P_s undergoes a continuous phase transition down to zero.

First-order ferroelectric phase transition

When the coefficient α_2 is negative, the phase transition will happen as a first-order transition. We must now retain α_3 and keep it positive in order to prevent ΔG

going to minus infinity in equation (1.8). The equilibrium condition for E=0 is given by:

$$\beta(T - T_C)P_s - |\alpha_2|P_s^3 + \alpha_3 P_s^5 = 0 \quad (1.12)$$

so that either P_s=0, or P_s is obtained by the real solutions of the following equation:

$$\beta(T - T_C) - |\alpha_2|P_s^2 + \alpha_3 P_s^4 = 0 \quad (1.13)$$

At the transition temperature, the Gibbs energy deduced from either the paraelectric and or ferroelectric phases should be identical. That is, the value of $\Delta G|_{Ps=0}$ is the same as the ΔG at the minima given by equation (1.13) as shown by the curve for T=T_C in Figure 1.4(a). Figure 1.4(b) shows the characteristic variation with temperature of the P_s for a first-order transition, in contrast to the continuous dropping of P_s to zero shown in Figure 1.3(b).

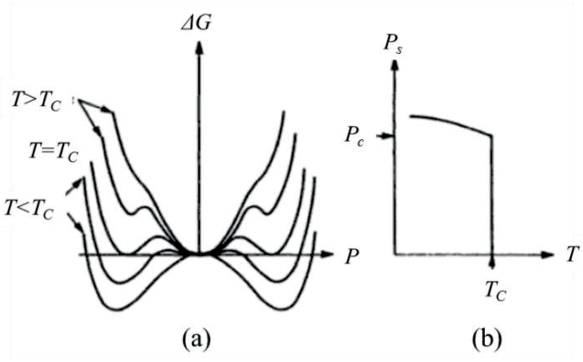

Figure 1.4: Qualitative temperature dependence of the curves for ΔG vs. P (a) and of the spontaneous polarization P_s (b) near a first-order ferroelectric phase transition. The P_c stands for the spontaneous polarization when T=T_C.

1.1.4 Permittivity development as a function of temperature in ferroelectrics

Basic

In linear dielectrics, the polarization P_i is proportional to the applied electric field E_j, with a second rank tensor named dielectric susceptibility χ_{ij}:

$$P_i = \chi_{ij} E_j \quad (1.14)$$

The dielectric displacement D_i is defined as:

$$D_i = \varepsilon_0 E_i + P_i = \left(\varepsilon_0 \delta_{ij} + \chi_{ij}\right) E_j = \varepsilon_0 \varepsilon_{ij} E_j \quad (1.15)$$

with the vacuum permittivity ε_0. δ_{ij} is the Kronecker's symbol with δ_{ij}=1 for i=j and otherwise δ_{ij}=0. ε_{ij} is the relative permittivity.

Phase transition behavior

For a *second-order ferroelectric phase transition*, we already concluded the relation between the temperature and the reciprocal permittivity in the equation (1.9) for $T>T_C$. At $T<T_C$, the reciprocal permittivity in the ferroelectric phase is written as:

$$\kappa^{\chi,T<T_C} = \frac{\partial E}{\partial P} = \beta(T - T_C) + 3\alpha_2 P^2 \tag{1.16}$$

Substituting equation (1.11) into equation (1.16) gives:

$$\kappa^{\chi,T<T_C} = 2\beta(T_C - T) \tag{1.17}$$

This temperature dependence is sketched in Figure 1.5(a). The slope of the reciprocal isothermal permittivity $\kappa^{\chi,T}$ vs. T curve below T_C is negative and twice as large as above T_C. In particular the value change of the reciprocal permittivity is continuous at T=T_C.

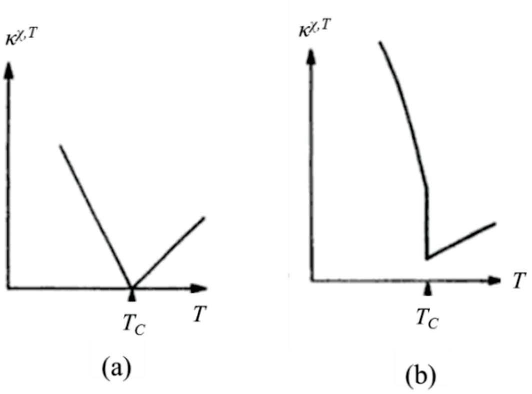

Figure 1.5: The sketch of the dependence of the reciprocal isothermal permittivity $\kappa^{\chi,T}$ on temperature for second-order (a) and first-order (b) phase transitions.

The reciprocal permittivity $\kappa^{\chi,T}$ demonstrates a different temperature dependence during a *first-order ferroelectric phase transition*. For the paraelectric phase, $\kappa^{\chi,T}$ still follows Curie-Weiss law as:

$$\kappa^{\chi,T} = \beta(T - T_0) \tag{1.18}$$

but here the Curie-Weiss temperature T_0 is not equal to the transition temperature T_C. At the transition temperature under zero field we have the equilibrium conditions of ΔG =0 and E=0 from equations (1.7) and (1.8):

$$\frac{1}{2}\beta(T - T_0) + \frac{1}{4}\alpha_2 P_s^2 + \frac{1}{6}\alpha_3 P_s^4 = 0 \tag{1.19}$$

$$\beta(T - T_0) + \alpha_2 P_s^2 + \alpha_3 P_s^4 = 0 \tag{1.20}$$

Further calculation gives:

$$T = T_C = T_0 + \frac{3}{16}\frac{\alpha_2^2}{\beta\alpha_3} \tag{1.21}$$

$$P_s^2|_{T=T_C} = -\frac{3}{4}\frac{\alpha_2}{\alpha_3} \tag{1.22}$$

Thus the behavior of $\kappa^{\chi,T}$ in the full temperature range is revealed by combining all the above equations:

$$\kappa^{\chi,T<T_C} = 8\beta(T_C - T) + \frac{3}{4}\frac{\alpha_2^2}{\alpha_3},\ T \to T_C^- \tag{1.23}$$

$$\kappa^{\chi,T>T_C} = \beta(T - T_C) + \frac{3}{16}\frac{\alpha_2^2}{\alpha_3},\ T \to T_C^+ \tag{1.24}$$

These two relations allow the permittivity to stay finite though discontinuous at T_C. The ratio of the slopes $d\kappa^{\chi,T}/dT$ immediately below T_C to that immediately above T_C is -8. The schematic presentation of the tendency of the reciprocal permittivity on the temperature is shown in Figure 1.5(b), presenting a discontinuous change at $T=T_C$.

1.1.5 Ferroelectric domains

When a thin plate of a ferroelectric single crystal or a monocrystalline thin film is oriented so that the polarization of all its unit cells is perpendicular to the plate or film surface, the bound charges of the intrinsic polarization induce a very high electric field opposite to the polarization, namely depolarization field. The depolarization field is sufficient to switch the polarization. The consequence is that the sample breaks up into regions, called *domains*, each has another permitted polarization direction to compromise with the depolarization field. The situation where all polarization vectors are pointed in one direction is called the monodomain state, while the situation with different polarization orientations in different regions is called the polydomain state.

Another reason for the appearance of the polydomain state is the relaxation of mechanical stresses. Considering a ferroelectric $BaTiO_3$ thin film with tetragonal lattice, the lattice constant *c* along Z-axis, which is parallel to the polarization, is slightly larger than the lattice constant *a* perpendicular to polarization. When the $BaTiO_3$ is epitaxially grown on a cubic substrate, there will be domains with their polarization vertical out-of plane known as *c* domain and others following in-plane orientation as *a* domain. Behind this *a*/*c* domain configuration is that the mixture of *a* and *c* domains minimizes the interfacial stress to the substrate due to the lattice constant mismatch.

The two reasons discussed above could be in favor of splitting materials into many domains; in contrary another factor stops the division, which is the electrostatic energy between differently oriented domains, proportional to the amount of the interfaces. The more domains splitting mean a higher electrostatic energy to balance the forces dividing domains. Thus, in particular materials, the combat among the three factors results finally in very complex domain patterns.

The interfaces between adjacent domains are called *domain walls*. The domain walls can be classified according to the angular difference of the polarization direction of the neighboring domains; the commonly observed domain walls in ferroelectric perovskites include 180°, 90° and 71°/109° domain wall.

In the case of a polydomain state, the material parameters, like dielectric constant, piezoelectric coefficient etc., originate from extrinsic and intrinsic contributions. The intrinsic contributions can be calculated using the thermodynamic potential as in section 1.1.3, and the extrinsic contributions originating mainly from ferroelectric domain walls contribution.[8] For instance due to their motion, domain walls can influence the permittivity under an AC electric field. Additionally, the domain wall kinetics could contribute to the ferroelectric hysteresis behavior as the motion of 180° domain walls has a significant role during the polarization reversal.

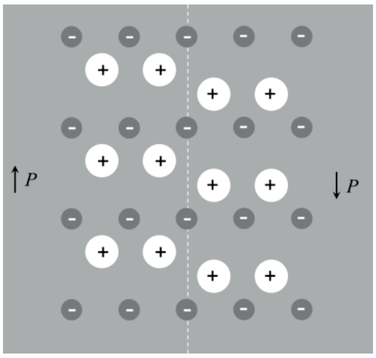

Figure 1.6: Schematic drawing of the atomic displacement on either side of an 180° domain wall in ferroelectrics. The central white dash line separates the two regions with opposite polarization orientations.

1.1.6 Polarization switching and ferroelectric hysteresis

The main features distinguishing ferroelectrics from other materials are the two or more stable states of the switchable spontaneous polarization and the ferroelectric hysteresis behavior.

The polarization switching in ferroelectrics includes the 3 following stages suggested by Merz[16] and Little[17]:

- Nucleation: Consists of the appearance of many small nuclei of inverse polarization as newly formed domains;

- Forward growth: The domains expand parallel to the direction of the polarization;
- Sideway growth: The domains expand perpendicular to the direction of the polarization, from the needle-like forward grown precursors.

The research of the field dependence of the maximal switching current and inverse switching time[18] endorsed low and high field behaviors corresponding to different switching stages. At low field, the thermally activated nucleation is the primary process for the polarization reversal and hence the switching current follows an exponential law. At high field, enough nuclei emerge and the polarization is limited by the forward and sideways growth of domains, i.e. the of domain wall movement, with a linear field-dependence.

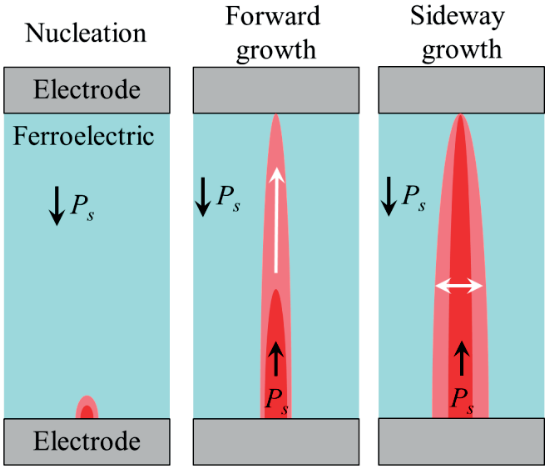

Figure 1.7: The schematic of the three growth stages with nucleation, forward and sideways growth.

The first theoretic approach to switch was proposed by Landauer at 1957.[19] The critical energy related to thermally active nuclei and the possibility of nucleation was concluded from the comparison between the energy gained upon polarization reversal to the domain wall energy and the energy associated with the depolarizing field. However the theoretical expectation did not coincide with experimental data. For closing the divergence between theorists and experimentalists, G. Gerra *et al.* added the interface energy term into the Landauer model, considering the real ferroelectric-electrode interface, and decreased the nucleation barrier successfully.[20] Further study revealed the possibility of cold-field nucleation, i.e. a nucleation that happens without thermal activation, deduced from observations of non-exponential temperature behavior of the switching dynamics.[21,22]

The first mathematical description of domain wall motion was established by Miller and Savage at 1958[23], and the picture of a wall-adjacent nucleus, namely a nucleation next to an existing domain wall, was developed almost immediately after[24,25]. With the development of microscopy techniques and simulation abilities, the creeping process of a thickness dependent sideways domain wall motion was observed[26] and corrected the shortcomings of the previous model[27].

From the discussion of thermodynamic theory in section 1.1.3, the feature of hysteresis results from the relation between P and E. Above the Curie temperature, the polarization is oriented following the direction of the external electric field and stays 0 at zero field in which P-E relation monotonically follows the curve associated to $T>T_C$ in Figure 1.8. Below the Curie temperature, the hysteresis can be illustrated by the equation (1.8), as in a second-order phase transition. With $T<T_C$, the coefficients fulfill the relation of $\alpha_1<0$ and α_2, $\alpha_3>0$, which results that the curve corresponding to $T<T_C$ includes a part with a negative slope for unstable states. When the electric field is equal to the critical value E_c, the polarization abruptly switches from one stable state to another along the dashed vertical lines. In both directions of the applied electric fields, the measured P-E relation shows a hysteresis behavior.

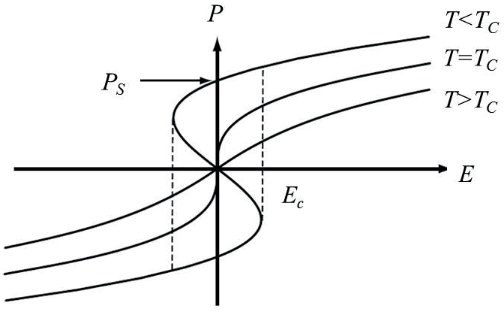

Figure 1.8: Dependence of polarization on electric field at three different temperatures in a ferroelectric with a second-order transition. The P-E relation according to equation (1.8) results in a hysteresis loop at $T<T_C$.

1.1.7 Depolarization effect

Depolarization effect is a twinborn phenomenon associated with the spontaneous polarization, which consists in formation of depolarization electric field and reduction of the polarization.[28] Depolarization effect significantly influences ferroelectric properties of thin films and may result in a substantial shift of the ferroelectric T_C, i.e. may cause a transition from ferroelectric to paraelectric phase below the nominal T_C. In multilayered systems like ferroelectric field effect structure (which is the subject of this thesis) depolarization effect is essential for understanding the electronic properties of the interfaces.

The physical origin of depolarization effect is an incomplete compensation of the bound charge associated with spontaneous polarization at the ferroelectric interfaces. A commonly used approach that accounts for this incomplete screening is so-called "passive layer" model.[29] The model considers a layered structure composed of a ferroelectric layer with thickness L and non-switchable dielectric layer with thickness d of which the permittivity is much less than that of the ferroelectric. The bound charge of spontaneous polarization at the ferroelectric/dielectric interface induces the charge of the opposite sign on the other interface of the "passive" dielectric layer. The formalism developed below shows how to predict the decrease of spontaneous polarization and ferroelectric-paraelectric phase transition in such layered structure based on Landau theory combined with electrostatics.

The dielectric displacements in the ferroelectric and dielectric layers can be written as:

$$D_f = \varepsilon_0 \varepsilon_b E_f + P_f \tag{1.25}$$

$$D_d = \varepsilon_0 \varepsilon_d E_d \tag{1.26}$$

where ε_b is the background dielectric permittivity of the ferroelectric layer (without soft mode), e.g. about 10 in PZT (short for $Pb(Zr,Ti)O_3$) and about 7 in PVDF, ε_d the dielectric constant of the dielectric layers, E_f and E_d the electric field in the ferroelectric and dielectric layers, P_f the ferroelectric polarization.

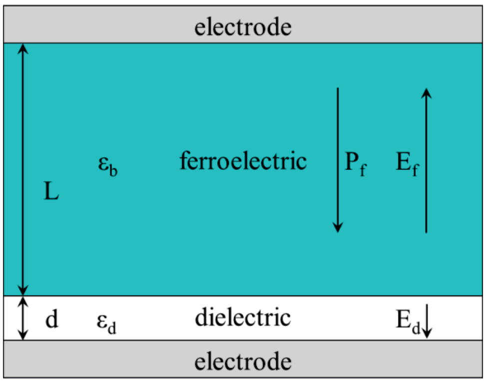

Figure 1.9: Illustration of depolarization field in the ferroelectric layer with a dielectric passive layer in series.

Considering the whole potential drop across the capacitor is zero, this results in:

$$E_f L + E_d d = 0 \tag{1.27}$$

From the constraint of continuous displacement value on the interface $D_f = D_d$, we obtain:

$$E_f = -\frac{P_f d}{\varepsilon_0 \varepsilon_d L + \varepsilon_0 \varepsilon_b d} \tag{1.28}$$

$$E_d = \frac{P_f L}{\varepsilon_0 \varepsilon_d L + \varepsilon_0 \varepsilon_b d} \tag{1.29}$$

And from equation (1.8) we can get:

$$E_f = \alpha_1 P_f + \alpha_2 P_f^3 + \alpha_3 P_f^5 \tag{1.30}$$

As a general discussion, we just consider the situation of second-order transition ($\alpha_1<0$ and $\alpha_2>0$) and ignore the high power term $\alpha_3 P_f^5$. The simultaneous equations of (1.28) and (1.30) give the non-zero solution of P_f:

$$P_f = \sqrt{-\frac{1}{\alpha_2}\left(\alpha_1 + \frac{d}{\varepsilon_0\varepsilon_d L + \varepsilon_0\varepsilon_b d}\right)} = \sqrt{-\frac{\alpha_1^*}{\alpha_2}} \tag{1.31}$$

where $\alpha_1^* = \alpha_1 + \frac{d}{\varepsilon_0\varepsilon_d L + \varepsilon_0\varepsilon_b d}$.

For ferroelectric thick films or ceramics, we have $L>>d$ for a relatively thin passive layer resulting in $\alpha_1^*\approx\alpha_1$ and the spontaneous polarization does not change. Nevertheless when d is comparable with L, i.e. the ferroelectric layer is very thin, we will have $|\alpha_1^*|<|\alpha_1|$ meaning that the effective polarization decreases. When assuming P_f=0, the criterion of the ratio between L and d is concluded as:

$$\frac{L}{d}\Big|_{P_f=0} = \frac{1}{\varepsilon_0\varepsilon_d|\alpha_1|} - \frac{\varepsilon_b}{\varepsilon_d} = \lambda \tag{1.32}$$

When the passive layer is thicker than L/λ, equation (1.31) does not have a real P_f solution and the only available one is that of equation (1.30), namely P_f =0, i.e. the ferroelectric phase becomes instable due to the depolarization effect. This conclusion implies a lower thickness limitation for ferroelectric layers having certain passive dielectric layers, hindering applications of ultra-thin films in functional heterostructures. From the optimistic aspect, a reduction of depolarization effect can be achieved through enhancing material quality or interface condition to minimize the passive layer.

1.1.8 Ferroelectric materials

The most important family of ferroelectrics is the perovskite ceramics with a chemical formula ABO_3, where A is a mono-, di- or tri-valent A cation and B a tri-, tetra- or penta-valent cation. In the centro-symmetric cubic structure, the A cations are located at the corners of the unit cell, the B cations are body-centered, and the oxygen anions are face-centered. The most well-known members in this family are $BaTiO_3$, $PbTiO_3$ and the solid solution $Pb(Zr,Ti)O_3$ (known as PZT for short).

The first perovskite oxide compound identified as being ferroelectric was $BaTiO_3$.[3] The ferroelectric phase transition from cubic into tetragonal lattice happens at T=393K. Upon further cooling, it will transform to orthorhombic phase at 278K, and rhombohedral phase at 183K. The measured spontaneous polarizations in the rhombohedral, orthorhombic and tetragonal phases are 33μC/cm^2, 36μC/cm^2 and 27μC/cm^2, respectively.[30]

$PbTiO_3$ has a paraelectric-ferroelectric transition temperature of 760K to a tetragonal $P4mm$ ground state, with a polarization of about 75μC/cm^2 at room temperature.[30] Different from $BaTiO_3$ with undisplaced Ba^{2+} ions, the displacement of the Pb^{2+} ion, in addition to that of Ti^{4+}, is substantial and contributes significantly to the spontaneous polarization when phase transiting.[31]

For its favorable piezoelectric properties, $Pb(Zr,Ti)O_3$ has a significant technological role in applications as actuators and transducers. For this solid solution, there is a phase boundary at about 45% Zr/55% Ti concentration ratio separating the rhombohedral (Zr rich side) and tetragonal (Ti rich side) phases in this ferroelectric, which is called the morphotropic phase boundary (MPB). Near the MPB, an applied electric field can easily induce a tremendous piezoelectric response.[32]

Another highly useful ferroelectric material is $LiNbO_3$, an oxide with a trigonal paraelectric structure. The paraelectric phase has a rhombohedral unit cell of $R\bar{3}c$ symmetry with two formula units per unit cell. Below the ferroelectric transition temperature, the cations are displaced along the [111] direction, breaking the mirror-plane symmetry and resulting in a spontaneous polarization. The paraelectric-ferroelectric transition occurs at 1483K, with a spontaneous polarization of 71μC/cm^2 at room temperature.[32]

Ferroelectricity in organic solids has been observed in polymers[4,11] and molecular crystals[33,34,35]. In general, new organic ferroelectrics are searched by synthesis of dipolar molecules or searching molecules with orientable hydrogen bonds. These materials are based on non-covalent molecules, in which ferroelectricity arises either from molecular dipole displacements or from the collective transfer of electrons or protons. Among the various organic ferroelectrics, PVDF with its copolymer P(VDF-TrFE), dominate current materials research due to the relative strong residual polarization, thermal stability and fast switching response.

1.1.9 The selection of ferroelectric materials for multiferroics studies

Multiferroic materials are those possessing two or more ferroic properties in one system. In particular materials containing both ferroelectric and ferromagnetic orders, generally known as magnetoelectric multiferroics, attract high interest, driven by their potential for electronic and spintronic applications. The single phase multiferroics by coupling of the two order parameters, opened the path for novel device functionalities[36,37,38], but meanwhile they are trapped by difficulties including weakness of this coupling[39], very limited materials which are single-phase multiferroics[40] and difficulties to integrate them with semiconductor technology.

To solve this issue, the composite multiferroics offer a way out, which consist of two or more separate phases possessing ferroelectricity or ferromagnetism and coupling via an interaction across the interface between the different protagonists. There have been significant research efforts on strain-induced coupling which relies on the piezoelectric effect and magnetostriction.[41,42] However for thin film memory and logic devices, the magnetoelectric coupling is limited through the mechanical clamping of the film to the substrate.[39]

Thus researchers moved forward to another type of multiferroics relying on electric-field-mediated coupling. The intimate contact between the ferroelectric layer and ferromagnetic channel further requires high crystalline quality interface to reduce the electric field screening. With the delicate epitaxy method, high quality perovskite ferroelectrics (PZT and $BaTiO_3$) were indeed grown successfully on $La_xSr_{1-x}MnO_3$ (LSMO) substrates showing ferroelectric control on the magnetic T_C shift and tunnel current spin polarization.[43,44]

In spite of these achievements with multiferroic coupling, the integration of ferroelectric perovskites into semiconductor electronics is problematic due to processing incompatibility, i.e. the high temperature processing for perovskites can eliminate most of the diluted magnetic semiconductors and metallic thin films applicable to the carrier-mediated interaction. All the above-mentioned restrictions on the material choices propel us to put the faith on the ferroelectric polymer PVDF.

For this ferroelectric, the chemical inertness excludes chemical reaction with the magnetic channels allowing ferromagnetism to persist, and its processing requires a very low annealing temperature of about 130-140°C to align the polymer chains. These factors endorse PVDF as an adequate solution for the ferroelectric gate material in the electric-field-mediated multiferroic heterostructures.

Indeed, the ferroelectric polymer thin film PVDF is more amiable than oxide ferroelectrics to semiconductor and metallic thin films.[45,46,47,48] The PVDF thin film has an appropriate combination of elevated spontaneous polarization and of low dielectric constant which helps to reduce depolarization problems. More important, the gentle processing conditions with low-temperature annealing promise its compatibility to the magnetic substrate used in this thesis.

1.2 PVDF and its ferroelectric properties

PVDF, the polymer 1,1-difluoroethylene, is a member of the fluoropolymers family. Its resistance to solvents, acids and bases allows wide applications in both industry and scientific research. PVDF is commonly used for insulation of electrical wires, because of its combination of flexibility, low density, and high electrical, chemical corrosion and heat resistances. It is also a standard binder material used in composite electrodes for lithium ion batteries. Another example for application is from biochemical research where the artificial membrane in immune-blotting is made of PVDF, due to its resistance to chemicals and low protein binding.

The exploration of electric properties in PVDF started half a century ago: Piezoelectricity was observed in this material at 1969[49] and ferroelectricity was found two years later[4]. The combination of ferroelectricity and the typical polymer properties, as the flexibility, light weight and low cost, brings PVDF into various electronic applications. PVDF non-volatile memory device based on the ferroelectric hysteresis was firstly demonstrated on metal-PVDF-insulator-semiconductor capacitor.[50] Other potential applications including ferroelectric diodes[85], use as a solar cell component for its spontaneous polarization[87], and mechanical/acoustic sensors and actuators[51] relying on its strong piezoelectric response were demonstrated as well.

1.2.1 Chemical formula

In the single molecule of 1,1-difluoroethylene (CH_2CF_2), the valence electrons of the carbon atoms follow sp^2 hybridization, confining the six atoms in the same plane. After the polymerization in “head-to-tail” configuration, the two hydrogen and two fluorine atoms are *alternately* bonded to the carbon atoms of the molecular backbone. In the molecule chain the carbon electrons obtain sp^3 hybridization, i.e. the four covalent bonds are oriented in a tetrahedral geometry and the C-C bond angle is equal to 109.5°, as one of common chain alignments shown in Figure 1.10(a).

In this organic polymer, ferroelectricity originates from the electric dipoles in the molecules, which can be reversed by molecule chain rotations under electric field. To explain the intrinsic dipoles, the key point is the increasing electronegativity from hydrogen (H: 2.20) to carbon (C: 2.55) and ended at fluorine (F: 3.98). Thus the electrons are on average closer to C than H along the C-H bond resulting in a dipole with positive charge δ+ on hydrogen and δ- on carbon. A similar dipole can be found on the C-F bond with δ+ on carbon side and δ- on fluorine, as depicted in Figure 1.10(b). In total the polar vector is aligned from the fluorine side to the hydrogen side.

The macroscopic polarization of PVDF thin films requires not only the dipolar configuration in the individual link but also the ordered arrangement of these microscopic elements. Concerning the molecular structure, ferroelectric PVDF is obtained in only three configurations among all possible ones.

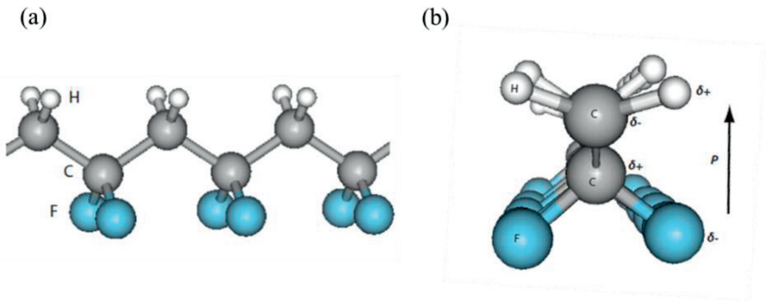

Figure 1.10: The chemical structure of PVDF. (a) A side view showing the carbon backbone forming in zigzag shape, so-called *all trans TT* configuration. (b) The view along the direction of the polymer long axis of PVDF, with the electronegativity of H, C and F atoms and the dipole direction from an individual link indicated by P_s. The original figures are from Ref.52.

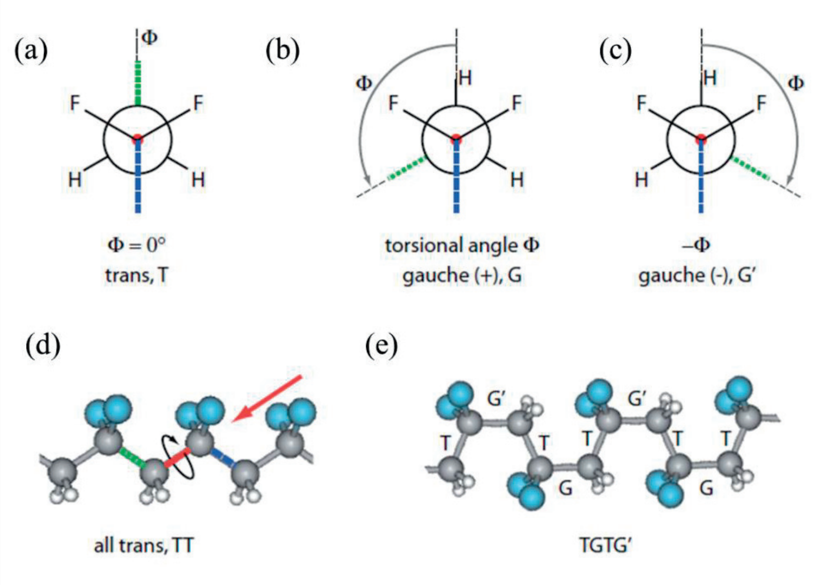

Figure 1.11: (a)-(c) Different conformations of a PVDF macromolecule of *trans*, *gauche*(+) and *gauche*(-). This projection is in direction of the arrow indicated in figure (d). (d) The *trans* state of subsequent C-C bonds results in a maximal stretched chain. (e)An alternative conjunction of *trans* and *gauche* (+ and -) conformations would result in a *TGTG'* chain.[52]

The conformation of the macromolecules is designated with the *trans* (*T*) and *gauche* (*G*) terms. The *trans* conformation corresponds to an angle of Φ=0° in the Newman projection for a minimum-energy position as illustrated in Figure 1.11(a). With the sp^3 hybridization and the $-[-CH_2-CF_2-]_n-$ elements, all the C-C bonds are in the *trans* conformation as shown in Figure 1.11(d), obtaining the maximally stretched C backbone. Besides *trans*, there are two possible *gauche* conformations shown in

Figure 1.11(b)&(c), and more precisely, depending on the direction of the bond rotation, *gauche* (+) [*G*] or *gauche* (-) [*G'*].

The polymers in melt or solution are disordered with respect to the regular conformation. When solidifying, the macromolecules can either keep disordered phase or crystallize into a regular configuration, which corresponds to the amorphous region and crystalline region in the solid material. At an equilibrium under Van der Waals force, the PVDF macromolecules are usually stabilized in three conformations: *TT*, *TGTG'*, *TTTGTTTG'* (or T_3GT_3G'), named by the twists in the periodic segments. With *TT* conformation, the dipoles on C-H and C-F bonds are fully oriented in perpendicular to the chain axis direction however the dipole vector gets an additional component along the chain in *TGTG'* conformation and the perpendicular component decreases.[53]

1.2.2 Crystallographic structure

As described in details in Ref. 52, the four common polymorphs of pure PVDF found in experiments are related to the various conformations of the molecules (*TT*, *TGTG'*, and *TTTGTTTG'*), and the polymorphs data of PVDF are listed in Table 1.1. They are transformable between each other through macroscopic treatments like stretching and heating to rotate the macromolecule chains.

Names	Conformation	Type of Dielectric	Lattice parameter				Lattice
			a[Å]	*b*[Å]	*c*[Å]	*β*[°]	
Form I *β*	*TT*, *all-trans*	ferroel.	8.58	4.91	2.56		b.c. orthorhombic
Form II *α*	*TGTG'* *antiparallel*	nonpolar.	4.96	9.64	4.62	90	monoclinic[54]
Form II$_P$ $\delta=\alpha_P$	*TGTG'* *parallel*	ferroel.	essentially the same as form II *α*				monoclinic
Form III ϒ	*TTTGTTTG'* *parallel*	ferroel.	4.96	9.58	9.23	92.9	monoclinic

Table 1.1: Summary of the four common polymorphs of PVDF.[55,56,57]

For multiferroics applications utilizing the spontaneous polarization from a poled PVDF thin film, the *β* ferroelectric phase is the most important, having the highest macroscopic polarization perpendicular to the surface of thin films. Fresh from spin-coating deposition, the PVDF molecules in the thin film are far from the ordered ferroelectric phase. Thus an additional process is necessary to trigger the ferroelectric *β* phase transition as described later in section 1.2.5.

1.2.3 Copolymer with TrFE

In a fully crystalized PVDF thin film in *TT* conformation/*β* phase, the unit cells are arranged in a spatial period with *a*=8.58Å, *b*=4.91Å and *c*=2.56Å. However the space offered in a *TT* crystal (0.256nm) is slightly narrower than the diameter of F atoms (0.270nm), therefore the lack of space will twist the carbon keel to left or right to *G*/*G'* bonds instead of neat *all-trans TT* arrangement. Typically the material is full of a mixture of *TT* and *gauche* conformations and its crystallinity is decreased dramatically. Thus in a pure PVDF membrane, the ferroelectric properties are hindered by the weak crystallinity of the *TT* conformation.

Introduction of some F atoms in the molecule chains instead of the H atoms results in a more stable *TT* conformation, because the repellence between F atoms in the *TT* conformation is lower than that between adjacent atoms in the *gauche* conformation.[58] This preference of the *TT* conformation favors the crystallization and enhances the crystallinity in the ferroelectric phase. The replacement of H atoms is accomplished by addition of trifluoroethylene (TrFE; $-CF_2-CHF-$) to the pure PVDF. Rather than the maximum 50% crystallinity of pure PVDF, 90% crystallinity is obtained in the copolymer with molecular ratio of VDF:TrFE between 70:30 and 80:20. With some hydrogen atoms replaced by fluorine, the average dipole in the copolymer is decreased proportional to the concentration of the TrFE component. However the benefit from crystallinity enhancement overcomes the dipole reduction in the copolymer to harvest a high macroscopic polarization.[59]

1.2.4 Polymer thin film preparation

Two approaches are commonly used for the preparation of ferroelectric polymer thin films used in electronic devices: solvent coating and Langmuir-Blodgett growth. In the solvent coating method, the polymer is first dissolved in a polar solvent at concentrations of several weight percents. Then the solution is spun or cast into sheets or films. After the solvent is evaporated, a solid film is left which is normally polymorphous, i.e. an inhomogeneous mixture of amorphous and crystalline matrix. By these means, it is generally possible to obtain ~50% crystallinity and ~25% polarization in the ferroelectric phase with pure PVDF and over 90% crystallinity and 80% polarization with copolymers containing approximately 50%-80% VDF.[58]

The Langmuir-Blodgett (LB) technique is the process of depositing uniform molecular monolayers (MLs) on solid substrates. After dispersing the material on the surface of a liquid to form a very thin, typically monomolecular, Langmuir layer, the floating layer is transferred onto a substrate by vertical dipping.[50] The final thickness of LB film is determined precisely by the number of the repeating transfer cycles and the thickness of the single layer. Another prominent advantage of LB technique is the ability to control film structure by adjusting conditions on the liquid surface, which is usually bounded by air or an inert atmosphere, before the transfer to solid substrate.

Besides these two well-known processes, another notable method is the epitaxial vapor deposition of crystalline mats of VDF oligomers consisting of short iodine-terminated chains of VDF with the chemical formula CF_3-$[CH_2$-$CF_2]_{17}$-I.[60,61] The oligomer films exhibit reversible switching thus likely to be ferroelectric. The attractive points of this technique include but are not limited to the following:

- Easy deposition by evaporation, hence more amiable than LB deposition;
- Potentially easy control over properties and functionalities by changing the chain lengths and the terminating groups, CF_3 and I;
- Controlled crystallization with the expectation of fewer chain-folding defects and lamellar structures.

After preparation, electron irradiation is sometimes used to modify the polymer thin film. Electron irradiation has been used to modify the switching properties[62] or convert P(VDF-TrFE) into relaxors[63], through forming double bonds and crosslinking, reducing crystallinity and lattice strain. An interesting possibility is to promote fast switching by inducing artificial defects in favor of nucleation during polarization reversal.[64] However conversion of the material to an amorphous state and loss of crystallinity are not negligible.[64]

Among the three preparation methods described above, the present work utilizes the solvent coating method which is the most mature and therefore suitable when the purpose is investigation of the ferroelectric field effect on carrier density mediation in transistors rather than investigation of the processing of PVDF itself.

1.2.5 The ferroelectric phase in P(VDF-TrFE)

The ferroelectric domains

Above the Curie temperature, the macromolecule is made of randomly rotated chains containing *T*, *G* and *G'* bonds and arranged in a hexagonal *6/mmm* symmetry in the materials, as shown in Figure 1.12(a) in which the circles stand for randomly oriented macromolecules. With the temperature decreasing, the *TT* conformation dominates the order of the copolymer molecule chains and the orientations among the chains are aligned along one direction. The phase transition results in an orthorhombic *mm2* symmetry, i.e. ferroelectric β phase, as depicted in Figure 1.12(b), while the chains are stretched along the *c*-axis. The orthorhombic *mm2* symmetry in the ferroelectric phase allows for six different domain states. Hence, 60° domain walls can be expected. The alignment of molecules across a domain wall is illustrated in Figure 1.12(c).

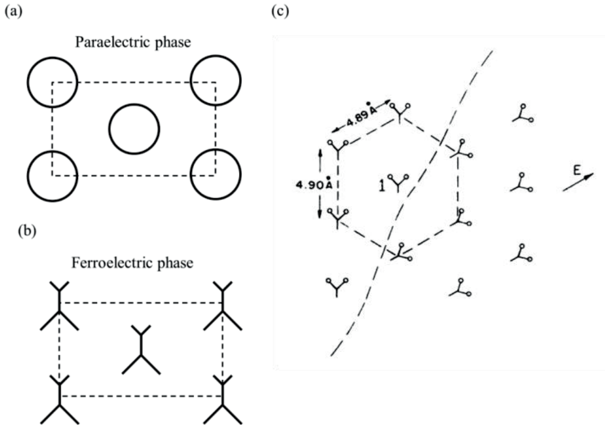

Figure 1.12: Illustration of (a) the hexagonal *6/mmm* symmetry in the paraelectric phase and (b) the orthorhombic *mm2* symmetry in the ferroelectric phase of P(VDF-TrFE). (c) The relative orientations of the PVDF molecules across a 60° domain walls[65].

Preparation of the ferroelectric phase

In pure PVDF, the ferroelectric β phase is commonly obtained by mechanical stretching of the α phase material[66]: (1) from the melt under specific conditions such as high pressure[67], external electric field[68] and ultra-fast cooling[69]; (2) from solution by casting at specific temperatures[70] or by the addition of nucleating fillers[71,72]. For applications requiring thin film form integrated with delicate semiconductor or metal films, a gentle low-temperature annealing is usually chosen as the applicable treatment for the phase transition.[73] As explained below, the copolymer P(VDF-TrFE) can be transformed into the ferroelectric phase simply by annealing, which is compatible with electronic thin film technologies.

As we have chosen P(VDF-TrFE) as the ferroelectric material instead of pure PVDF, three structural phases can be found in the copolymer:

- Low-temperature phase (LT): ferroelectric, similar to β phase in PVDF;
- High-temperature phase (HT): paraelectric, only observed in copolymer with randomly oriented molecules;
- Cooled phase (CL): formed after cooling with a TrFE composition of >30%, with the segments of *TT* chains separated by *gauche* bonds and 60° torsion.

Contrary to PVDF, the copolymer P(VDF-TrFE) presents always the ferroelectric β phase once VDF compound is in a specific range (discussed below), independently of the used processing method, either melt or solution casting.[74] Furthermore, this copolymer also shows the Curie temperature below the melting temperature, contrary to what happens in PVDF, which melts in its ferroelectric phase, and, in this way, the copolymer allows the study of the ferroelectric to paraelectric phase transition.[75]

As illustrated in Figure 1.13, the pure PVDF, corresponding to the right edge of the phase diagram, does not have the paraelectric HT phase implying its estimated T_C is higher than the melting point. By substitution of H by F atoms, the phase transition between ordered LT phase and disordered HT phase was characterized experimentally. The LT-HT transition temperature showing a hysteresis between heating and cooling process suggests a first-order phase transition.

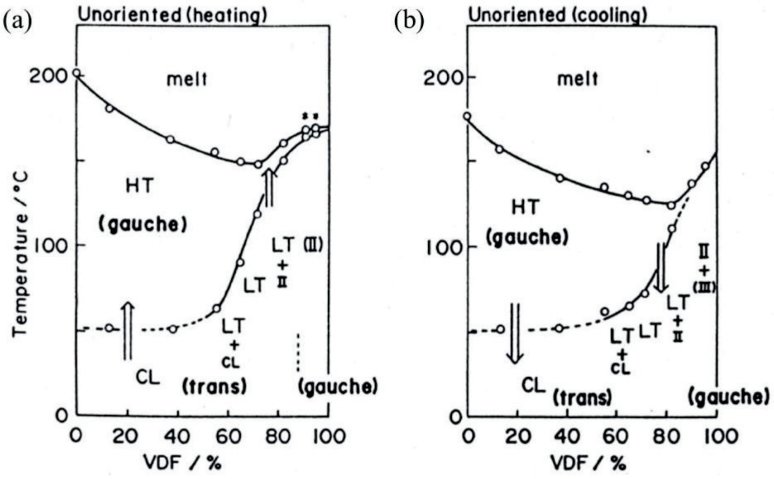

Figure 1.13: The phase diagram of the copolymer P(VDF-TrFE) for cooling and heating for different VDF:TrFE composition.[55]

T. Yagi *et al.* firstly synthesized the P(VDF-TrFE) copolymers over the whole range of compositions and characterized their properties systematically.[76] It has been found that the most interesting compositions consist of 50~80% VDF due to their relatively well-defined Curie temperature, the stability of the phase, and their high crystallinity.[77]

We used a 77/23 mol% composition of the P(VDF-TrFE) copolymer deposited by spin-coating for all our experimental studies. This choice is made with its advantages on remnant polarization and Curie temperature (see in Table 1.2) compared to the copolymers with 70/30 molecular ratio P(VDF-TrFE)[58,59] or deposited by LB technique[78]: the higher T_C provides a sharper switching behavior when the polarization reverses; the stronger remnant polarization means larger carrier density shift in a field-effect application and better performance.

Property	PVDF	P(VDF-TrFE) 80:20	P(VDF-TrFE) 70:30
Melting temperature	180˚C	148˚C.	152˚C
Transition temperature	N.A.	145˚C	116˚C
Dielectric constant	16	12	10
Remnant polarization	12μC/cm^2	10μC/cm^2	8μC/cm^2
Coercive field	75MV/m	38MV/m	5-60MV/m

Table 1.2: Properties of PVDF and its copolymers.[50]

1.2.6 Polarization reversal

The polarization reversal in the PVDF polymers can be understood as a molecular chain rotation. Theory suggested the reversal process as a thermally activated kink formation at the surface of a crystalline lamellae, and a subsequent motion through it.[65] Instead of a one-time 180˚ polarization switching, the polarization reversal involves three sequential 60˚ chain rotations. This was concluded from a comparison between the theoretical waiting time for complete reversal made of three 60˚ rotations and the experimental results.

Beyond the molecular rotations as the atoms rearrange themselves, the polarization reversal shows a further complexity. Suggested by Furukawa,[58] there are two more arrangements catalyzing the reorientation process, namely chain and lamella arrangement: after the reversal of a single molecular chain, a second stage, so-called chain arrangement follows, which is the expansion of the rotated chain region in one lamella; the lamella arrangement happens as to reverse the total film with the interaction between lamellas and the amorphous matrix in between.

Kolmogorov-Avrami model was used to quantify the switching phenomenon in thin film.[79,80] R. Gysel *et al.* observed a restricted domain growth in P(VDF-TrFE) thin film. They found that the interface-adjacent passive layer resulted in a retardation of the polarization reversal and impacted the switching properties considerably.[81] In the smaller structure of P(VDF-TrFE) nanomesas,[82] microscopic study showed that the domain switching behavior was drastically different from that of inorganic solid-state crystalline ferroelectrics. It was observed that the switching proceeds through a number of domain nuclei away from the PFM tip-surface contact point, namely “remote nucleation”. Moreover the growing domain in the P(VDF-TrFE) nanomesa acquires a profoundly irregular shape. These observations were associated with a high-degree nonuniformity of the local switching potential.

1.2.7 Ferroelectric polymers in electronics

The integration of ferroelectric polymer into electronic devices started 30 years ago: N. Yamauchi presented in 1986 the fabrication of memory devices known as metal-ferroelectric-insulator-semiconductor (MFIS) containing capacitor made of a ferroelectric polymer obtained by solvent spinning.[45] During the following years, the MFIS capacitors obtained dramatic improvements including operation voltage decreasing from about 200V[45] in the first generation down to 10V[83] and maintaining a reasonable on/off capacitance ratio of 8:1 with LB ferroelectric thin[84].

Ferroelectric diodes provide bistable resistivity states in miniaturized MFIS devices eliminating concerns of the finite charge displacement typical for FRAM technology. The bistability comes from a modulation of the depletion width by the ferroelectric polarization. For a polarization parallel to the built-in field, the depletion width is small and the resistance of the diode is low. *Vice versa* with antiparallel polarization to the built-in field, the depletion region is wider and the resistance is higher.[85] This type of electronics was demonstrated using blended P(VDF-TrFE) films and the polymer semiconductor rir-P3HT [region-irregular poly(3-hexylthiophene)] with the ratio 90:10.[86] The plots of current density J versus applied voltage V presented maximum two orders of magnitude change of resistance when the polarization in P(VDF-TrFE) was reversed.

The MFIS capacitor requires relatively inefficient slow capacitance measurements to read the device state, and faces a compromise between low-voltage operation vs. long retention. To overcome the poor performance, ferroelectric field effect transistor (FeFET) was developed as a competitive candidate for novel non-volatile memory devices. The detailed state of art about FeFET with P(VDF-TrFE) is presented in the next subchapter.

Besides these non-volatile memory devices, P(VDF-TrFE) films have been lately shown to be important components in polymeric organic photovoltaic (OPV) cells.[87] With the application of a poled P(VDF-TrFE) layer, a strong, permanent, internal electric field was generated to efficiently separate the electrons and holes and thus prevent their recombination. With the effect on the carrier separation, ferroelectric polymer layers enhanced the efficiency of OPV devices from 1-2% without layers to 4-5% with the fluoropolymer layers, and these enhanced efficiencies were 10-20% higher than those achieved by other methods.

1.3 Ferroelectric polymer gated field effect transistor

1.3.1 Field effect transistor

The well-known field-effect transistor (FET) is a transistor in which the conductivity of a channel between two electrodes called *source* and *drain*, is controlled by the applied electric field on the third electrode, the *gate*. FET is classified as a unipolar device because only one kind of charge carriers, electrons or holes, predominantly participates in the conduction process. The conductivity in the channel between the source and the drain is determined by the concentration and mobility of the free charge carriers, in which the former factor is controlled by the electric field from gate penetrating into the conductive material, like semiconductor or metal thin films.

There are two main types of field effect transistors, the junction field effect transistor (JFET) and the metal-oxide-semiconductor field effect transistor (MOSFET), illustrated in Figure 1.14(a)&(b). In this part we illustrate the working principle of FET based on MOSFET configuration. Its name refers to the metallic gate electrode, the insulator, typically an oxide, but also other dielectrics, e.g. Si_3N_4, and the semiconductor channel. In particular applications, other materials with similar functionality are used, for instance, indium tin oxide (ITO) gate electrode, Si_3N_4 dielectric layer and field tunable ultra-thin Co film.

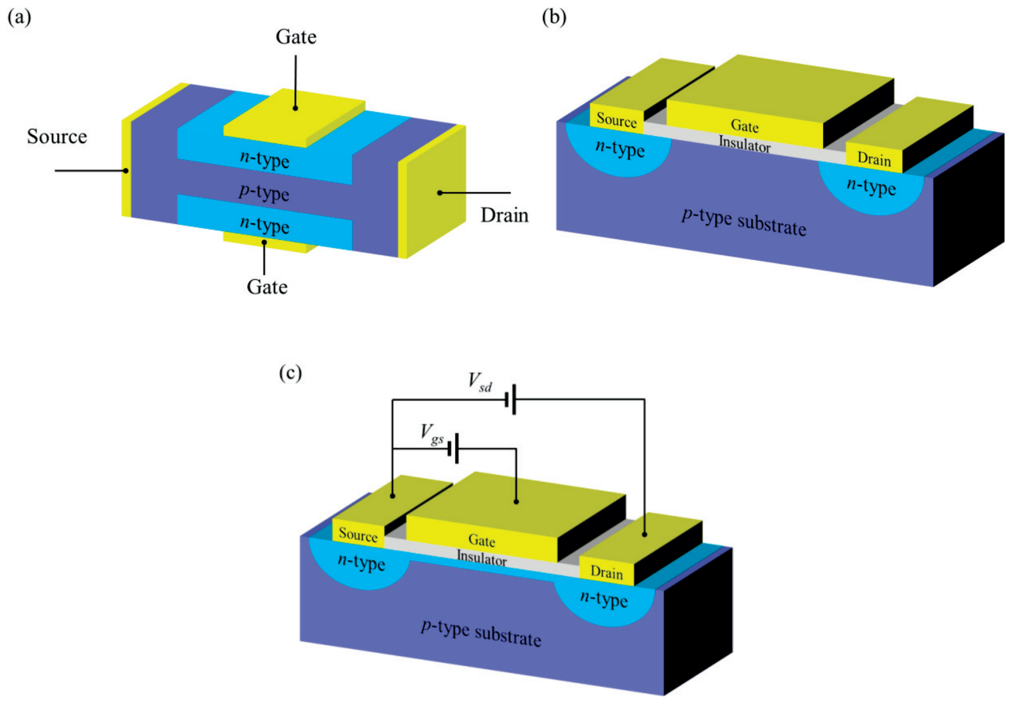

Figure 1.14: The schematic illustration of (a) JFET and (b) MOSFET configurations. (c) In the “on” state of MOSFET, the applied voltage between the gate and the source V_{gs} over a threshold will open the channel for electrons to drift from source to drain driven by the voltage V_{sd} between them.

As in Figure 1.14(b), a *p*-type semiconductor substrate is heavily doped with donor elements by ion implantation forming the source and drain *n*-type regions. At the *pn* contact interfaces, the electron and hole diffusion and recombination builds up a depletion region. When without a gate bias or with a bias lower than the threshold value, the charge carrier movement between source and drain is blocked and the device shows “off” state with a very low conductance. However when a high enough bias is applied on the gate as in Figure 1.14(c), holes drift away and the region below the dielectric layer becomes depleted of holes due to the electric field penetrating into the semiconductor. According to the mass-action law $n \cdot p$=const., the electron concentration increases dramatically and brings about a continuous *n*-type layer between source and drain allowing mobile electrons, namely an inversion layer. This is so-called “on” state with a high conductance between source and drain.

We should note that the MOSFET is a *volatile* device. With a zero gate-source voltage, the device is in the “off” state regardless the previous on/off state. A *non-volatile* FET integrating a ferroelectric material is described below.

1.3.2 FeFET with inorganic gate materials

In 1957, the idea to replace the dielectric gate by ferroelectric material in a FET to obtain non-volatile device was patented by Ross.[88] Compared to conventional FET, the remnant polarization of the ferroelectric gate maintains the field effect control on the conductive channel. In the *npn*-type substrate as discussed in the previous subsection, the channel is inversed for the gate polarized by a positive voltage V_{gs} (“on” state). In contrast, when the polarization is switched by a negative V_{gs}, the transistor is in “off” state, as the conjunction regions between *np* and *pn* form opposite oriented diodes blocking the source-drain current I_{sd}.

Compared to MFIS capacitor, the non-volatile memory device based on FeFET has several advantages: non-destructive read-out, better fatigue resistance, lower power consumption and a higher bit density.

The first realization of FeFET device was done by Moll and Tarui in 1963.[89] In their report, the FeFET used 150µm thick triglycine sulfate (TGS) as a ferroelectric gate on 100nm CdS semiconductor layer. With ±90V polarization voltage, the resistance between source and drain presented the relative variation about 25%. The first Si-based FeFET device was reported by Wu in 1974.[90] Using RF sputtering, the ferroelectric oxide $Bi_4Ti_3O_{12}$ was deposited on *p*-type Si substrate. In contrast to 80µA “on” state current, the current value in “off” state was not readable from the instrument. Moreover, injection of carriers from the semiconductor into the ferroelectric layer was observed when gating voltage was higher than 20V.

After additional early works using $LiNbO_3$[91] or $BaMgF_4$[92], more recent works used perovskite ferroelectrics like PZT[93]. In the first PZT-based FeFET, the ferroelectric-semiconductor combination was $Pb(Zr_{0.2}Ti_{0.8})O_3/La_{0.7}Ca_{0.3}MnO_3$. With 7V voltage switching, the on/off current ratio reached 3 and only 3% change of the channel resistance was left after waiting 45min at room temperature.

A promising result using inorganic gate FeFET was achieved on the heterostructure of $SrBi_2Ta_2O_9$ (known as SBT)/SiO_2/Si, with 10^3 on/off ratio and 10 hours retention.[94] The improvement is related to an inserted floating metallic gate electrode between the ferroelectric and dielectric layer. Through controlling the area ratio between the capacitor on the ferroelectric and dielectric layers, the higher induced charge density in SBT film was reduced on the SiO_2 layer below its maximum induced charge density ($\pm 3.5 \mu C/cm^2$).

The limited retention performance of FeFET device got huge improvement with the multilayer of $(Pb_{0.95}La_{0.05})(Zr_{0.2}Ti_{0.8})O_3/(La_{1.94}Sr_{0.06})CuO_4$.[95,96] The all perovskite device presented 70% channel modulation and >2 month retention of stored data. Furthermore, introduction of high-κ dielectric buffer layer HfO_2 enhanced the SBT gate efficiency: on/off current ratio about 2×10^6 after 12 days and the retention extrapolation of 10^5 after 10 years![97]

1.3.3 Difficulties in the realization of FeFET

In spite of the achievements described above, several difficulties persist, for the realization of a successful FeFET with inorganic gate:

1) Processing incompatibility, especially in terms of heat treatments;
2) High depolarization field that reduces the ferroelectric polarization;
3) Polarization back switching (retention loss) driven by depolarization field;
4) Charge injection and screening of the polarization at the interface-adjacent layer.

Basically those problems are related to three reasons: fabrication problems, depolarization effect and charge injection issues.

Fabrication problems

Processing incompatibility is a fundamental hindrance on the processing of FeFET devices with inorganic ferroelectrics. The ferroelectrics as PZT and other perovskites have inevitable incompatibility with the current semiconductor technologies that is already discussed in section 1.1.9 above.

Depolarization effect

As discussed in section 1.1.7, the depolarization field exists due to an insulating layer even without an intentionally deposited dielectric layer. Even in a device having a direct contact between the ferroelectric gate and the conductive layer, a low-permittivity transition layer can form by interdiffusion of the constituent elements at the ferroelectric-conductor interface, which typically occurs in high temperature processes.

From the practical point of view, the depolarization effect is two-fold. Firstly it reduces the net polarization in a single domain state. As we saw in equation (1.31), the corrected remnant polarization is less than the thermodynamic value in equation (1.11). Secondly, a high depolarization field causes the ferroelectric thin film to break into polydomain states as explained in section 1.1.5. The polydomain formation results in a reduction in the macroscopic polarization of the ferroelectric gate and consequently a possible loss of the inversion state in the source-drain channel of FeFET consequently. With time, the depolarization field eliminates the remnant polarization, i.e. a retention loss.

Reviewing equation (1.31) we can conclude the following relation:

$$P_f^2 \propto |\alpha_1| - \frac{1}{\varepsilon_0}\frac{d}{\varepsilon_d L+\varepsilon_b d} \tag{1.33}$$

In general, the parameters related to dielectric response can be considered as the total effect from passive layer of ferroelectric gate material and the intentionally deposited buffer layer between ferroelectrics and conductors (if any).

The existence of a low-permittivity dielectric layer, like the commonly used SiO_2, can complicate the polarization reversal in the ferroelectric during the information writing process. In a sandwich consisting of a high-permittivity ferroelectric and a low-permittivity dielectric, the applied voltage drops mainly in the dielectric layer, i.e. the switching voltage on the FeFET gate electrode needs to be very high in order to guarantee that the electric field in the ferroelectric layer is above the coercive field.

Inspection on relation (1.33) suggests the use of high-κ dielectric buffer layer as a solution. With a larger ε_d, the second term on the right side of relation (1.33) can be decreased to preserve a stronger P_f. In fact the literatures reported a corresponding retention improvement by the utilization of HfO_2 dielectric layer.[97]

A change in the device design can suppress further the depolarization loss in FeFET. With a special 1T2C (1 transistor and 2 capacitors) design integrating the ferroelectric SBT in two oppositely poled capacitors with a Si-based transistor, the depolarization loss was constrained and the retention time improved.[98] In comparison to the ordinary 1T1C FeFET[94], the retention time was tripled by the 1T2C configuration reaching over 10^5s. The simplicity of the single transistor FeFET was however sacrificed.

Charge injection

Another reason for the reduction of retention is charge trapping at the gate ferroelectric/dielectric interface. In a general consideration with the condition $d \ll L$, the electric field in the dielectric layer is estimated from equation (1.29):

$$E_d \approx \frac{P_f}{\varepsilon_0 \varepsilon_d} \tag{1.34}$$

The field E_d can reach up to a high value, pushing the charge through the dielectric layer and trapping it at the ferroelectric/dielectric interface. The trapped charge leads to a local compensation of the polarization. Furthermore, the inversion layer of the source-drain channel is gradually lost.

When considering the problems of depolarization and charge injection together, a simple increase of the thickness of the insulating layer d must be rejected: even with charge injection minimized, equation (1.33) predicts a stronger depolarization effect. With the high-κ dielectrics buffer the ε_d is larger however the layer thickness d increases as well comparing to the SiO_2 layer which can be naturally formed in the air with a few monolayer thickness. It is impossible to simultaneously address the two major detrimental effects on retention time by modifying the insulating layer alone.

Ferroelectric copolymers of P(VDF-TrFE) group offer an attractive combination of properties including low dielectric constant and optimal values of spontaneous polarization (6-8μC/cm^2) for ferroelectric FET applications. This allows keeping the depolarization effects relatively low while maintaining sufficient non-volatile field effect for controlling the channel. A series of proof-of-concept studies summarized in the next subsection demonstrates the viability of ferroelectric polymer gates for FeFET applications.

1.3.4 Novel FeFET with P(VDF-TrFE) gate

Advantages of P(VDF-TrFE) gate in FeFET

The main advantages of the copolymer P(VDF-TrFE) for integration in the gate of FET are the following:

- Low dielectric constant;
- Smaller than PZT yet significant spontaneous polarization;
- Low processing temperature;
- Chemical stability and compatibility with wide range of materials;
- Non-toxicity.

With the much lower dielectric constant and smaller spontaneous polarization than that of perovskites, the depolarization effect and charge injection issues are suppressed in the ferroelectric gate discussed above.

Processing of P(VDF-TrFE) below 140°C is a crucial advantage over perovskite oxides that generally have to be annealed at temperatures higher than the critical limit of 400°C for Si-based semiconductor technology.

Disadvantages of P(VDF-TrFE) gate in FeFET

The possible drawbacks of P(VDF-TrFE)-based FeFET are listed below:

- Limited temperature stability;
- High fields are required for fast polarization reversal;
- Relative slow switching speed;
- Long term endurance issues due to polarization fatigue.

The low temperature stability is due to the Curie temperature and the melting point, both below 150˚C. A complication of the low T_C is the strong temperature dependence of spontaneous polarization (e.g. the quick dropping polarization in Figure 1.3(b)). This limits the application of this material for devices requiring high stability over a wide temperature range. In daily life circumstance at room temperature, the temperature stability is however sufficient.

The switching speed on P(VDF-TrFE) was characterized under various electric field strength. Most of the results show the magnitude of microsecond.[50] As a comparison, modern DRAM has a much shorter writing time, less than 2ns.[99]

The uncertainties of the properties of the P(VDF-TrFE) thin films include the fatigue behavior, the polarization reversal, and the long term stability. These properties are still under research.

Next we review the progress and achievements of the research on P(VDF-TrFE) based FeFET.

FeFET with ferroelectric polymer gate has the almost same length of history as the MIFS capacitor device. The first P(VDF-TrFE) FeFET was presented in the same paper about P(VDF-TrFE) capacitor device in 1986.[45] This Si-based FeFET had a sandwich structure gate as the 80nm spun P(VDF-TrFE) covered by SiO_2 layers (71nm and 50nm thick) on both sides to improve breakdown resistance and to reduce charge injection into the ferroelectric. Due to the relatively thick dielectric layers, the polarization reversal in P(VDF-TrFE) required a voltage pulse >180V for 10s. Meanwhile the on/off source-drain current ratio was huge: 10^6. The retention performance was not reported.

The study of FeFET with LB-grown P(VDF-TrFE) was presented recently by Gerber.[100] The FeFET gate fabrication was done on the *p*-type doped Si wafer with 10nm SiO_2 oxide layer. With 25 LB transfers and 130˚C annealing for 1h, the P(VDF-TrFE) layer thickness was 35nm. The width of the hysteresis loop in source-drain current I_{sd} vs. applied gate voltage V_g, namely the memory window, was 3V wide under a large V_g sweep ±14V. However the retention performance was not satisfactory: less than 10s even after applying 10V poling voltage pulse.

Interestingly the same group reported within one month[101] that by replacing the dielectric material from SiO_2 to CeO_2 ($\varepsilon_d \approx 26$), the FeFET retention time was improved tremendously. In the configuration of 15ML P(VDF-TrFE)/30nm CeO_2 for the gate, the retention time was prolonged to 10min with 7V poling voltage pulse.

R. Gysel *et al.* demonstrated one-transistor non-volatile memory cell implemented by integration of a ferroelectric P(VDF-TrFE) gate on a standard *n*-type metal oxide semiconductor FET.[102] Here the copolymer gate thickness was 240nm after spin-coating and 140˚C annealing for 10min. 30V/2s voltage pulse was applied on the gate electrode to polarize the P(VDF-TrFE) layer and the electronic transport measurement reported an on/off I_{sd} ratio about 10^2-10^3, with retention exceeding 2-3 days. Through comparing the piezoelectric polarization loops taken immediately after poling and 24h later, polarization stability of 24h was shown. This PFM experiment concluded that retention loss was not associated with the depolarization effect.

FeFET application is being explored also on other systems apart from silicon. One hybrid concept is the modulation of the electric transport properties of a two dimensional electron gas (2DEG) in an $Al_{0.3}Ga_{0.7}N$/GaN heterostructure.[46] In that report, the heterostructure consists of a 7nm of Si doped $Al_{0.3}Ga_{0.7}N$ ($n=3\times10^{18}$electrons/cm^3) as conductive channel, 10nm undoped $Al_{0.3}Ga_{0.7}N$ and 250nm 70/30 P(VDF-TrFE) as the ferroelectric gate configuration. With -30V gating voltage, the FeFET gave an increase of sheet resistance by a factor of 3 and a decrease of carrier mobility by a factor of 1.85. The time-dependence characterization demonstrated a retention time of about 30min.

The 2DEG can also be replaced by graphene. Utilizing the polarization of ferroelectric P(VDF-TrFE) gate,[103] the graphene FeFET presented a factor of difference of 2.5 between the saturated values of high and low resistance states.

Fully organic electronics is expected as alternative to Si-based semiconductor technology in the future due to their advantages in terms of low costs and easy processibility. In fully organic FeFET, the conductance increase in the semiconductor channel originates from the accumulation of charge carriers, instead of an inversion layer as in inorganic devices. The most successful combination of organic semiconductor and ferroelectric gate shown to date is the poly[2-methoxy, 5-(2’-ethyl-hexyloxy)-p-phenylene-vinylene] (MEH-PPV) *p*-type semiconductor and a ferroelectric P(VDF-TrFE) gate.[104] With the absence of the gate oxide, the device allowed for higher charge densities on the gate, which are limited in inorganic FeFET by the insulator breakdown field. A coercive voltage of ±35V was measured for the 0.85μm thick P(VDF-TrFE) layer in I_{sd} vs. V_g measurements. The on/off current ratio varied among different samples from 10^3 to 10^5. The retention test, presented on a sample with on/off ratio of 10^4, is shown in Figure 1.15(b). The endurance experiment was successful during 10^3 programming cycles while the sample remained with 10^3 on/off ratio.

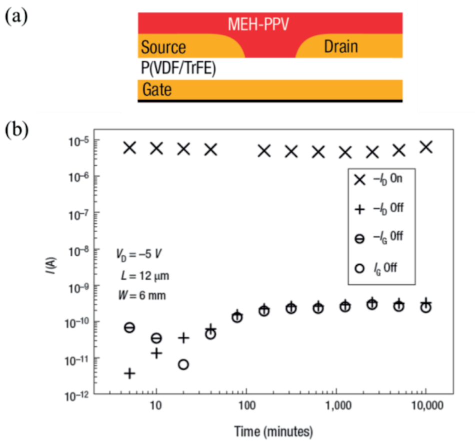

Figure 1.15: (a) Schematic cross section illustration of the P(VDF-TrFE)/MEH-PPV fully organic FeFET device. (b) Data retention measurement obtained by programming the on- or off-state once and monitoring the drain current at zero gate bias for a week.[104]

As the review of literatures demonstrates, the organic ferroelectric P(VDF-TrFE) presents its advantages as a gate material in FeFET devices instead of perovskite ceramics. The wide compatibility of P(VDF-TrFE) is proven that this copolymer gate can be integrated on various channel materials, such as Si, GaN, graphene and MEH-PPV, in contrast to the limited choices for PZT and SBT ferroelectric gate. The retention study shows also a weaker loss in FeFET allowing the maintain of the field effect for days, unlike the few hours shown in inorganic gate FeFET. Thus we are confident to choose P(VDF-TrFE) as the ferroelectric gate material for the multiferroic study.

1.4 Summary

In this chapter the phenomenon of ferroelectricity was discussed with focus on multilayered structures where the spontaneous polarization of ferroelectric alters properties of the adjacent material. Analysis of physical effects responsible for polarization loss and screening of ferroelectric field effect suggests that organic ferroelectric P(VDF-TrFE) layers are attractive candidates for ferroelectric gates. In the context of present study, the use of P(VDF-TrFE) offers a solution for gating ultrathin magnetic layers, which do not easily lend themself for integration.

Chapter 2

Ferromagnetic materials for ferroelectric gating

Similar to the logic of the first chapter, this chapter explains the basic principles of ferromagnetism and then moves to ferromagnetic materials. The ferromagnetic properties of (Ga,Mn)As and Co thin films suitable to charge-mediated control are described. In the context of possible FET applications, the progresses of field-effect control on those magnetic thin films are reviewed following the timeline from the original proof-of-concept experiments to more advanced ferroelectric gate devices.

2.1 Ferromagnetism

2.1.1 Historical background

In 6th century BC, the magnetism in lodestone, the magnetic iron ore of FeO-Fe_2O_3, was mentioned in a Greek manuscript by Thales of Miletus. More than two thousand years later, the systematic scientific studies on magnetism, in particular the experiments by Michael Faraday and the fundamental electromagnetic equations of James Maxwell have established the framework for accurate description of magnetism and magnetic properties of materials. However, classical physics failed to explain the origin of ferromagnetism, which was properly addressed only in 20th century within the quantum theory.

With regards to magnetic properties, most materials can be classified in three large groups:

- Ferromagnetic and ferrimagnetic materials: These are the ones thought conventionally as magnetic. They retain magnetization with no external magnetic field applied and present macroscopic attraction/repulsion in bulk. Examples are ferrites and lodestone;

- Paramagnetics: These materials, such as platinum, aluminum and oxygen are attracted by an external magnetic field and develop their own induced magnetic field, however they do not retain any magnetization when the external magnetic field are switched off;

- Diamagnetics: Typical examples of this group are carbon, copper and water.

> These materials are weakly repelled by magnetic field. They respond to the external magnetic field by developing their own magnetic field that points in the opposite direction.

In addition to these principal groups there are various types of magnetism found in modern physics research, such as superparamagnetism, superdiamagnetism, and metamagnetism.

Magnetic materials play a key role in modern electronics because of their use in memory devices and other functional elements. Their properties used in device applications including giant magnetoresistance[105,106], ferromagnetic resonance[107] and galvanomagnetic properties[108] were observed in magnetic thin films[109].

2.1.2 The origin of ferromagnetism

Ferromagnetism is characterized by the non-zero spontaneous magnetic moment in the absence of the external magnetic field and the reversible orientations of magnetization.[110] Ferromagnets can be treated as paramagnets with an internal interaction, i.e. exchange interaction, tending to align the magnetic moments parallel to each other. To rationalize ferromagnetism and formation of spontaneous magnetization, quantum theory is required.

Considering an atom in free space, its magnetic moment is given by:

$$\boldsymbol{\mu} = \gamma\hbar\boldsymbol{J} = -g\mu_B\boldsymbol{J} \tag{2.1}$$

where γ is the ratio of the magnetic moment to the angular momentum, known as the gyromagnetic ratio, $\boldsymbol{J}$ the total angular momentum as the sum of the orbital and spin angular momenta, g is g-factor, the spectroscopic splitting factor, and Bohr magneton μ_B.

If a multi-atoms system has only two energy levels under external magnetic fields, the equilibrium between their populations is given by:

$$\frac{N_1}{N} = \frac{e^{\mu B/\tau}}{e^{\mu B/\tau}+e^{-\mu B/\tau}} \tag{2.2}$$

$$\frac{N_2}{N} = \frac{e^{-\mu B/\tau}}{e^{\mu B/\tau}+e^{-\mu B/\tau}} \tag{2.3}$$

where $\tau = k_BT$, N_1, N_2 are the populations of the lower and upper levels, $N=N_1+N_2$ the total number of atoms, and B the magnetic field. The projection of the magnetic moment of the upper state along the field direction is $-\mu$ and of the lower state is μ. The resultant magnetization for N atoms per unit volume is, with $x = \mu B/k_BT$:

$$M = (N_1 - N_2)\mu = N\mu\frac{e^x - e^{-x}}{e^x + e^{-x}} = N\mu\tanh x \tag{2.4}$$

In a magnetic field an atom with angular momentum quantum number J has $2J+1$ equally spaced energy levels. The magnetization is given by:

$$M = NgJ\mu_B B_J(gJ\mu_B B/k_B T) \tag{2.5}$$

where B_J is the Brillouin function.[110] In ferromagnets the exchange interaction can be approximated to a molecular field. The molecular field is estimated by the mean-field approximation with $B_E=\lambda M$. Then the equation (2.5) is reduced to:

$$M = N\mu \tanh(\mu\lambda M/k_B T) \tag{2.6}$$

If we define $T_C=N\mu^2\lambda/k_B$, non-zero M solutions of equation (2.6) exist between the temperature 0 and T_C. Those solutions correspond to the spontaneous magnetization in the materials. Here T_C is the Curie temperature separating the ferromagnetic and paramagnetic phases similar to the situation in ferroelectrics. The inspection of the temperature dependence of non-zero M solutions reveals that M decreases smoothly to zero at $T=T_C$. This behavior classifies the usual ferromagnetic/paramagnetic transition as a second-order phase transition.

This theory explained the temperature-dependent variation of susceptibility as well. In paramagnetic materials, i.e. in the high temperature phase, with $\mu B/k_B T<<1$, after the approximations of Brillouin function $B_J(\mu B/k_B T)$ the susceptibility runs as:

$$\frac{M}{B} \approx \frac{NJ(J+1)g^2\mu_B^2}{3k_B T} = \frac{Np^2\mu_B^2}{3k_B T} = \frac{C}{T} \tag{2.7}$$

where p is the effective number of Bohr magnetons, defined as $p=g[J(J+1)]^{1/2}$, and the constant C is the Curie constant. Equation (2.7) is known as the Curie law describing the susceptibility vs. T for paramagnetic materials.

Additionally, based on the molecular field approximation in ferromagnetic specimen, we have $B_E=\lambda M$ from the mean-field approximation. Further extrapolation of Curie law gives $M/(B_a+B_E)=C/T$ where B_a is the applied field. The susceptibility χ becomes:

$$\chi = \frac{M}{B_a} = \frac{C}{T-\lambda C} \tag{2.8}$$

which is known as Curie-Weiss law that describes the temperature dependence of susceptibility in the paramagnetic phase of the ferromagnets. With temperature decreasing to $T=T_C=\lambda C$, a singularity with infinite χ occurs and below this temperature a spontaneous non-zero magnetization M persisting without any applied magnetic field is observed.

2.1.3 Magnetic interaction in solid materials

The exchange interaction between spins plays a crucial role in magnetic arrangements of electrons, resulting in different magnetic properties. The interaction originates from Coulomb repulsion and Pauli Exclusion Principle.[111,112] To describe this interaction in quantum mechanics, the energy of two neighboring electrons is considered as depending on parallel or antiparallel alignment of their spins, usually written as Heisenberg Hamiltonian:

$$H = -2J_{ij}\vec{s_i} \cdot \vec{s_j} \tag{2.9}$$

where $\vec{s_i}$ and $\vec{s_j}$ is the spin vectors of two electrons, and J_{ij} the exchange integral describing the strength of exchange interaction. For many purposes in ferromagnetism, it is a good approximation to treat the spins as classical angular momentum vectors. For multiple-electrons-involved interaction between adjacent atoms, the Hamiltonian includes $\vec{S_i} = \sum \vec{s_i}$ and $\vec{S_j} = \sum \vec{s_j}$, as follows:

$$H = -2J_{ij}\vec{S_i} \cdot \vec{S_j} \tag{2.10}$$

The sign of the exchange integral will determine whether parallel or antiparallel alignment of those adjacent spins is favored for lower energy and stable state. Generally the parallel alignment leads to ferromagnetism while antiparallel to antiferromagnetism. We should remember that only unpaired electrons have contribution to $\vec{S_i}$ and $\vec{S_j}$.

In real materials, the interaction between electron moments, i.e. the Heisenberg Hamiltonian, is more complicated, involving multiple electrons with different angular moments and complex relative spatial positions. Three kinds of mechanism contribute to the magnetism with different interaction types.

Direct interaction

Within the materials in which the atoms have extended electron wave functions overlapping each other, the direct interaction can present a dominant contribution to align the spin direction of adjacent electrons. However, the direct exchange interaction is important only for a very narrow group of materials, such as the para-/ortho-H_2 and paramagnetic O_2 molecules. In best known magnetic solids, for instance iron, the extension of the 3*d* unpaired electron wave function is just 10% of the interatomic distance.

Itinerant interaction

In metals, most of the delocalized electrons from the partly filled orbits participate in the bonds. Ferromagnetism in this situation is no longer explainable by the interaction of localized electrons. The high density of free states near the Fermi level and big exchange integral support paralleled arrangement of the valence electrons and result in ferromagnetism. The quantitative description is available in the framework of Stoner model, which is discussed in section 2.1.4. This magnetic interaction is known as itinerant exchange, since the magnetism originates from delocalized "itinerant" electrons.

Indirect interaction

There is a wide range of magnetic materials where the interaction between spins is indirect i.e. involves more than two particles. An important example is the superexchange mechanism, which can be found in both ferromagnetic and antiferromagnetic materials. For example, in the antiferromagnetic manganese (II) oxide (MnO), the magnetic moments of one Mn^{2+} ion are coupled to another, bridged by paired electrons of the intermediate O^{2-} ion as depicted in Figure 2.1(a). The antiparallel arrangement of spin moments results in antiferromagnetic coupling.

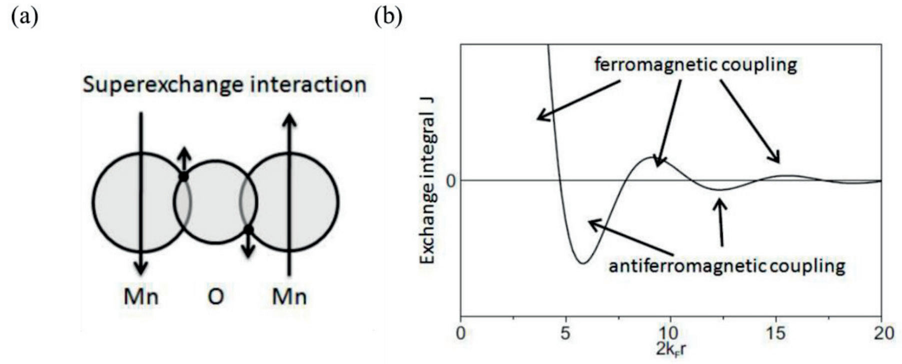

Figure 2.1: (a) Superexchange mechanism in antiferromagnetic MnO as an example of indirect interactions.[113] (b) Illustration of oscillation of the exchange integral after the RKKY theory.[114] Either a ferromagnetic or an antiferromagnetic interaction is possible depending on the separation distance of the atoms.

Another mechanism of indirect exchange interaction mediated by free carriers occurs in diluted magnetic semiconductors (DMS) and rare earth metals. With increase of the net acceptor concentration in DMSs, the impurity band merges with the valence band. For the average distance between the carriers, much smaller than the effective impurity Bohr radius, the holes reside in the band, and their quasi-free propagation is only weakly perturbed by scattering on Mn ions, whose long-range Coulomb interaction is screened by the carrier liquid. The Ruderman-Kittel-Kasuya-Yosida (RKKY) mechanism is responsible the for a long-range interaction between the spins with exchange integral J_{RKKY} that oscillates with the atomic distance:

$$J_{RKKY} \propto \frac{cos(2k_f)}{r^3} \tag{2.11}$$

where k_f is the absolute value of the wave vector at Fermi surface and r the atomic distance. The magnetic order is ferromagnetic or antiferromagnetic depending on the separation distance of the atomic cores as shown in Figure 2.1(b).[114] For the case of DMS films, the mean distance of the charge carriers is bigger than that of the spins, which prevents the exchange integral from oscillating.[115] At this condition the RKKY description is identical to the Zener model[116], which was used within mean-field approximation framework to describe the role of free carriers in mediating ferromagnetic ordering between localized spins[117].

2.1.4 Stoner model for spontaneous magnetization

In metals, each atom contributes with all its valence electrons to the formation of the metallic bond. Within this itinerant interaction mechanism, Stoner model is used to describe the spontaneous magnetization.

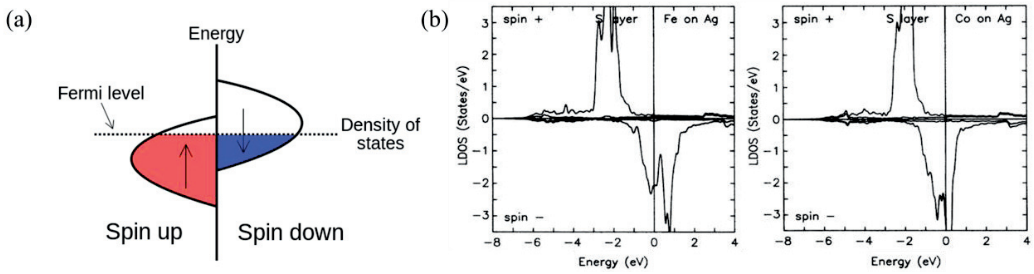

Figure 2.2: (a) A schematic band structure illustrating the scenario for Stoner model. Exchange interaction splits the electron energy of states with different spins. (b) The density of free states for ferromagnetic Fe and Co monolayers grown on Ag(001) substrate. Near Fermi level, both metallic thin films exhibit extreme high density of free states.[118]

Without considering magnetic exchange interaction, the band structures of metals are symmetric i.e. regardless of moment direction, the number of spin-up electrons is precisely the same as spin-down electrons. Near Fermi level the two kinds of electrons occupy the free states $N(E_F)$ with ratio 50/50. Considering the exchange interaction one arrives at the "split" state shown in Figure 2.2(a) where the Fermi levels for spin-up/spin-down electrons is shifted by δE. Due to redistribution of electrons the total electron energy increases by ΔE_1:

$$\Delta E_1 = \frac{1}{2} N(E_F)(\delta E)^2 \tag{2.12}$$

On the other hand, the magnetic exchange energy of electrons ΔE_2 also changes as follows:

$$\Delta E_2 = J\left[\frac{n}{2} + \frac{1}{2} N(E_F)\delta E\right]\left[\frac{n}{2} - \frac{1}{2} N(E_F)\delta E\right] - J \cdot \left(\frac{n}{2}\right)^2 = -\frac{1}{4} J N(E_F)^2 (\delta E)^2 \tag{2.13}$$

where J is the exchange integral and n is the total amount of electrons. As a result, the total energy change will be:

$$\varDelta E = \varDelta E_1 + \varDelta E_2 = \frac{1}{2}\left[1 - \frac{1}{2}JN(E_F)\right]N(E_F)(\delta E)^2 \tag{2.14}$$

Comparing the energy gain due to exchange interaction and loss due to the kinetic energy increase in expression (2.14) one can formulate the *Stoner criterion* for electron band spontaneous splitting (i.e. ferromagnetism onset) : $\frac{1}{2}JN(E_F) > 1$. A big exchange integral and a high density of free states near Fermi level will favor formation of spontaneous magnetization and ferromagnetism. In Figure 2.2(b) two ferromagnetic metal films, Fe and Co, with thickness of few monolayers show high density of states near the Fermi level and therefore fulfill Stoner criterion.

2.1.5 Magnetic anisotropy

Heisenberg Hamiltonian (2.10) describing the interaction between individual spins represents the simplest case when this interaction is isotropic. However, in reality the materials generally show anisotropic magnetization behavior.

The macroscopic anisotropy is a result of interplay of many factors. The first origin is the *shape*. If the sample is neither cubic nor spherical, the magnetization won't be equal for all directions. Second, in crystalline materials very important role is played by *magnetocrystalline anisotropy* that relates the magnetization to the principal axes of crystal lattice. The easy and hard magnetization axes in body-centered cubic, hexagonal and face-centered cubic lattice are shown in Figure 2.3. Other sources of anisotropy include magnetostatic anisotropy, magnetoelastic anisotropy and exchange anisotropy. Each one shows its importance under the specific conditions.

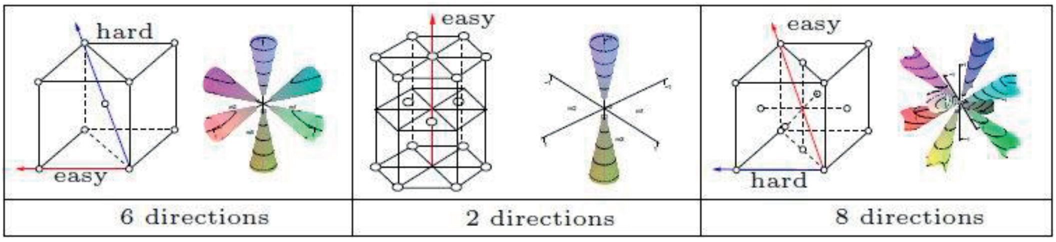

Figure 2.3: Examples of easy and hard directions in body-centered cubic, hexagonal and face-centered cubic lattices.[119]

Phenomenological description of the free energy F_C of the system as a function of magnetic field direction with respect to the easy magnetization axis is relatively simple for cubic magnetic materials:

$$F_c = K_1\left({\alpha_x}^2{\alpha_y}^2 + {\alpha_y}^2{\alpha_z}^2 + {\alpha_z}^2{\alpha_x}^2\right) + K_2\left({\alpha_x}^2{\alpha_y}^2{\alpha_z}^2\right) \tag{2.15}$$

where K_1 and K_2 are the cubic anisotropy constants, and α_x, α_y, α_z are the cosines of the angles between the magnetization and <001> crystalline direction. For uniaxial symmetry along Z-direction of crystal lattice, the free energy is simplified to:

$$F_u = K_u {\alpha_z}^2 \tag{2.16}$$

where K_u is the uniaxial anisotropy constant.

2.1.6 Magnetic domains and domain walls

At temperatures below T_C, the magnetic moments are aligned parallel locally. Macroscopic specimens are usually composed of regions with the same magnetization vector called *domains*. The relative directions of magnetization of different domains can vary (need not be parallel or antiparallel). The behavior observed in polycrystalline specimens is similar to that in single crystals. The domain structure always has its origin in the possibility of lowering the energy of a system by going from a saturated configuration with high magnetic energy to a domain configuration with a lower energy.[110]

The increase in the macroscopic magnetic moment of a ferromagnetic specimen in an applied magnetic field is governed by two independent processes: in weak applied fields the volume of domains favorably oriented with respect to the field increases at the expense of unfavorably oriented domains; in strong applied fields the domain magnetization rotates toward the direction of the field.

The transition region between domains is known as domain wall (similar to the ferroelectric case). Based on the space distribution of the magnetic momentum orientations within the wall, two principal types of domain walls are distinguished: Bloch wall and Néel walls. In most common Bloch walls magnetization rotates in the plane parallel to the wall plane, while in Néel walls, which may occur in thin films magnetization rotates around the axis perpendicular to the magnetic layer surface.

Of high practical importance is domain wall dynamics i.e. nucleation and propagation of domains (or domain wall movement) under external stimuli. In an ideal ferromagnetic film where pinning on defects is neglected, the domain wall motion is characterized by steady and precessional linear flow regimes.[120] At the low field the walls move steadily under field; while at the high field, the magnetization precesses about the field and a periodic component appears in the forward motion of the wall.[121] The low/high field ranges are separated by the critical value named Walker field $H_W=N_y 2\pi\alpha M_s$, where N_y is the demagnetizing factor across the wall, α the Gilbert loss parameter and M_s the saturation magnetization. However, in real films domain wall pinning on defects has to be taken into account. When the external magnetic field is far below the critical depinning value, the wall motion is called creeping.[122] For the other extreme case, once the magnetic field is extremely high, the disorder becomes irrelevant resulting in a dissipative viscous flow motion with the velocity proportional to the field strength.[122]

2.1.7 Anisotropic Magnetoresistance (AMR)

The phenomenon of anisotropic magnetoresistance (AMR) i.e. dependence of the electric resistance of magnetic materials on the magnetization direction has been known since 1857.[123] Although modern solid state physics offers general understanding of this phenomenon in terms of interplay between spin-orbit interaction and magnetization, the detailed microscopic description is available only for some relatively simple model cases.[124] In contrast to Anomalous Hall effect (AHE) that also links the magnetization and resistive properties of the system AMR is symmetrical with respect to the magnetization M direction when aligned by the strong magnetic field B. Specifically for the case of AMR the longitudinal resistivity $\rho_{xx}(M)=\rho_{xx}(-M)$, and the transverse resistivity $\rho_{xy}(M)=\rho_{xy}(-M)$, whereas AHE is antisymmetric with respect to the magnetization: $\rho_{xy}(M)= -\rho_{xy}(-M)$.

This phenomenon was studied since long time in ferromagnetic transition metals;[125,126] however, the underlying principles are still difficult to understand partly due to the relatively weak spin-orbit coupling (SOC) compared to other relevant energy scales and the complex band structure. From general theoretical analysis there are three different mechanisms of anisotropic scattering that have been shown to contribute to AMR phenomenon: directional anisotropy of Fermi carrier velocities, anisotropic scattering of carriers by spin-polarized impurities or anisotropic scattering of partially spin-polarized carriers by conventional (generally non-magnetic) impurities[124]. These scattering mechanisms are schematically illustrated in Figure 2.4 where the magnetization points to the right and Fermi velocity vectors are represented by arrows.

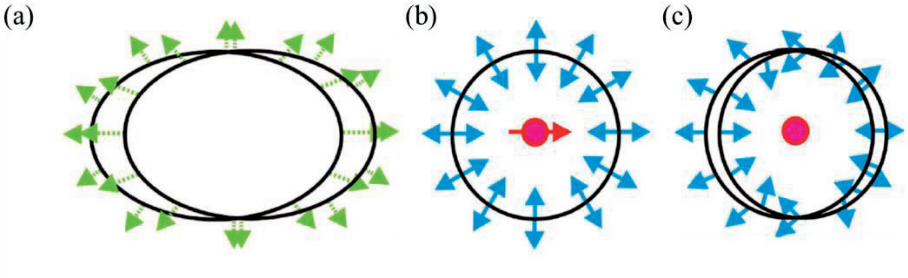

Figure 2.4: The three distinct mechanisms of AMR combining magnetization (pointing to the right and coupled antiferromagnetically to charge carrier spins in this sketch) and spin-orbit interaction: (a) anisotropic Fermi velocities (arrows) along the Fermi surface for the charge carriers, or anisotropic relaxation rates due to (b) unpolarized bands (represented by the indicated isotropic spin texture) scattered by anisotropic impurities; (c) partially polarized bands scattered by isotropic impurities.

Complete description of AMR requires measurement of two quantities: out-of-plane AMR (AMR_{OOP}) and in-plane AMR (AMR_{IP}):

$$AMR_{OOP} = \frac{\rho_{xx}(\vec{M}\|\vec{I}) - \rho_{xx}(\vec{M}\|\vec{n})}{\rho_{xx}(\vec{M}\|\vec{n})} \qquad (2.17)$$

$$AMR_{IP} = \frac{\rho_{xx}(\vec{M}\|\vec{I}) - \rho_{xx}(\vec{M}\perp\vec{I},\vec{n})}{\rho_{xx}(\vec{M}\perp\vec{I},\vec{n})} \qquad (2.18)$$

where $\vec{I}$ is the in-plane electrical current, $\vec{n}$ the surface vector of thin film, and $\vec{M}$ the magnetization vector. The differences between AMR_{OOP} and AMR_{IP} originate from the lowered symmetry in strained samples.

For most of conventional ferromagnetic materials (metals), AMR is generally a positive quantity[125,127], however in thin film diluted magnetic semiconductors (DMS) like (Ga,Mn)As under compressive strain it changes to negative[128].

In context of the present thesis work AMR represents an extremely valuable and sensitive tool that helps detecting even very faint changes of the magnetic state. In Chapter 4 it will be employed in order to probe the impact of charge carrier concentration on the magnetic anisotropy in DMS.

2.1.8 Ferromagnetic materials for field effect control of ferromagnetism

Ferromagnetic metals are extensively used in a wide range of electronic applications. Well-known magnetic metals include iron, cobalt and nickel. In these transition metals there are unpaired free $3d$-electrons which are ordered into parallel spin alignment via iterant interaction. The non-zero average spin moment per atom (Fe: 2.19μ_B, Co: 1.57μ_B, Ni: 0.62μ_B) brings the intense magnetic interaction and the high Curie temperatures.[110] Electrical control of ferromagnetism in metals is generally difficult because of very high electron densities, however recent results demonstrate that electrical gating is possible for ultra-thin films of a few monolayers.[129,130]

Among semiconductors there are ferromagnetic materials that contain at least one magnetic element in their chemical formula. Magnetic perovskites like (La,Sr)MnO$_3$ (LSMO) are representatives of this group where ferromagnetism is mediated by double exchange interaction.[131] Due to the coexistence of semiconductor properties and ferromagnetism, there is a possibility to concurrently control the charge carrier density and magnetic state.[132] However, the device integration is very difficult because of processing incompatibility of the manganates with standard semiconductor technology.

There is a group of semiconductors known as dilute magnetic semiconductors (DMSs) where the ferromagnetism is introduced by magnetic dopants. Suitable host materials can be either group IV elemental semiconductors or III-V and II-VI compound semiconductors, and Mn is widely used as the magnetic doping atom. In DMSs, ferromagnetic coupling is mainly mediated by delocalized carriers. In case of archetypical DMS material, (Ga,Mn)As the same dopant (Mn) provides both magnetic ions and strongly spin-orbit coupled holes required for ferromagnetic coupling. The coupling strength depends on carrier concentration, therefore electrical gating can directly influence the ferromagnetic state by inducing the accumulation/depletion state in DMS channel.

In this thesis work *DMSs* and *ferromagnetic metals*, specifically (Ga,Mn)As and Co thin films, were chosen to study non-volatile field-effect control of ferromagnetism. DMS offers a good model system with relatively well understood ferromagnetic coupling and its interplay with the charge density, whereas Co layers give a change to implement ferroelectric control of ferromagnetism within the temperature range suitable for applications.

2.2 Ferromagnetic ultrathin films of (Ga,Mn)As and Co

2.2.1 Ferromagnetism in (Ga,Mn)As thin films

As seen from the previous discussion, manganese doping of GaAs host constitutes a viable path towards ferromagnetism mediated by mobile charge carriers.[133] GaAs has zinc blend crystal structure and MnAs forms hexagonal structure. Thus the equilibrium condition of molecular beam epitaxy (MBE) growth is not applicable for the (Ga,Mn)As compounds. To avoid formation of hexagonal MnAs cluster, the growth of (Ga,Mn)As has to be far from equilibrium conditions where meta-stable (Ga,Mn)As zinc blend structure is favored.

For magnetic doping, the manganese atoms substitute gallium positions as Mn_{Ga} depicted in Figure 2.5. However, it is inevitable that manganese occupies also other positions in the crystal lattice, in particular manganese interstitial Mn_I in the center of a gallium tetrahedron is the most common one.[134] F. Maca *et al.* used these Mn_I defects to describe many properties of (Ga,Mn)As[135] and the analysis was experimentally confirmed[136]. Another common defect influencing the properties is As antisite As_{Ga} shown in Figure 2.5 as well.

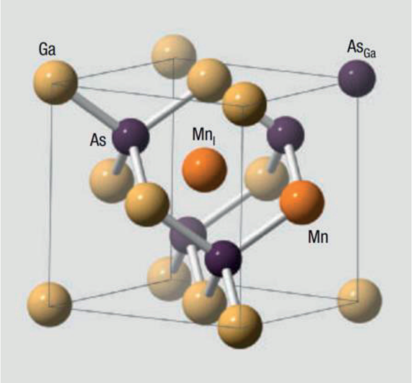

Figure 2.5: Unit cell of $Ga_xMn_{1-x}As$, with different types of defects: As_{Ga} is an As antisite and Mn_I represents Mn interstitials. For magnetic doping manganese has to substitute gallium (Mn_{Ga}), marked as Mn in the illustration, where it acts as an acceptor and couples ferromagnetically to other Mn_{Ga} positions. Alternatively it can occupy the interstitial site Mn_I in the center of a tetrahedron of gallium atoms. Also an As antisite impurity As_{Ga} is depicted. Both the Mn_I and As_{Ga} impurities act as donors.[137]

Manganese acceptor: Mn_{Ga}

In the ideal case of manganese substituting gallium, manganese has one less electron in its 4*p* shell than gallium, and a hole is created since an electron from the valence band is needed to perform the sp^3 hybridization for the tetragonal binding structure. In (Ga,Mn)As manganese plays a double role of magnetic dopant and acceptor that supplies free holes required for ferromagnetic coupling.

Interstitial Manganese: Mn_I

With high doping levels of manganese, the side effect of formation of Mn_I is inevitable. These defects work as double donors and reduce the hole concentration in the material. Additionally the Mn_I donors tend to form pair defects with substitutional manganese impurities. The superexchange interaction between these ions then results in a strong antiferromagnetic coupling, even effective up to room temperature. Therefore a large amount of Mn_I not only reduces the conductivity but also destroys the ferromagnetism.

Arsenide antisites: As_{Ga}

The low-temperature MBE growth of (Ga,Mn)As favors a large amount of As antisites. These double donor defects provoke a reduction of hole concentration deteriorating the (Ga,Mn)As ferromagnetic properties in the same manner as the donor character of Mn_I.

In (Ga,Mn)As the ferromagnetic properties depend on this hole concentration. One of the most important measures of the ferromagnetic interaction in solids is ferromagnetic Curie temperature, T_C. According to the Zener model for the (Ga,Mn)As case, the Curie temperature depends on the non-compensated manganese concentration x_{eff} and hole concentration p:[115]

$$T_C \propto x_{eff} p^{1/3} \tag{2.19}$$

In real (Ga,Mn)As materials Mn ions are distributed between Ga sites and interstitial sites. Mn dopants at interstitials are donors that pair with the substitutional Mn_{Ga} acceptors with approximate zero net moment, which results in an effective free local-moment doping $x_{eff}=x_s-x_i$ with the concentrations of substitutional Mn x_s and interstitial Mn x_i respectively. Equation (2.19) was confirmed experimentally by K. Wang *et al.*[138] as shown in Figure 2.6.

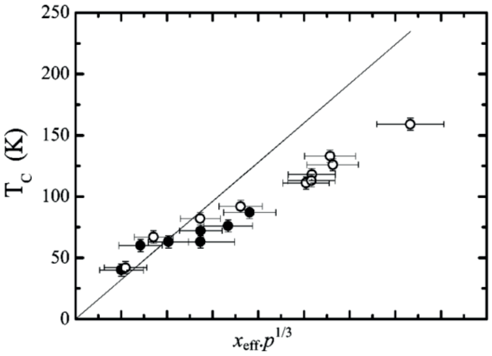

Figure 2.6: Experimentally determined T_C vs. $x_{eff} \cdot p^{1/3}$ diagram and Zener model prediction (solid line) from Ref.138.

In the thin film form of (Ga,Mn)As, the magnetic properties are different compared to the bulk form. In particular Curie temperature shows a pronounced temperature dependence with general trend of T_C decreasing with thickness; however a local maximum of T_C around 10nm was reported.[139] In other studies of $(Ga_{0.95},Mn_{0.05})$As thin films below 20nm it was demonstrated that the 5nm thick film got the highest T_C comparing to either thinner or thicker layers.[140,141] For ultra-thin films below 5nm the resistance strongly increases and the ferromagnetic properties are increasingly difficult to observe. In recent studies,[141,142] the ferromagnetic state has been observed below 30-40K in very thin films of 3.5nm.

In ultra-thin (Ga,Mn)As, there are two important relevant scale length of order 1nm which may influence the magnetic properties: the Thomas-Fermi screening length and the average Mn-Mn separation. The former implies a depth-dependent hole concentration through the channel, which can be tuned via applying external electric field, as modeled with Poisson solver in Ref. 141. The inhomogeneous hole distribution was discussed in relation with conventional FET configuration and the results suggested that the depth-averaged approximation is applicable.[143] The scale length relating to Mn-Mn average distance was shown not to affect magnetic properties down to 3nm.[142] The similar T_C of 3/5/7nm thick films supported that the major part of the Mn ions align in a sample-spanning ferromagnetic cluster, similar to thicker films.

The magnetic properties of (Ga,Mn)As thin films are also sensitive to the mechanical boundary conditions, specifically the strain imposed by the crystal lattice mismatch between the film and substrate. The Mn-doped thin films have a lattice constant between 0.566nm (GaAs) and 0.598nm (MnAs), depending on the Mn concentration. For instance the (Ga,Mn)As thin film grown films on GaAs substrate is in compressive strain and the deviation from a fully relaxed cubic lattice leads to the ferromagnetic anisotropy characterized by an in-plane easy axis. Through doping with P that substitute As atoms, the lattice constant of the dual-doped film can be reduced below that of GaAs. This strategy is widely used to tune the anisotropy inducing the crossover between the in-plane and out-of-plane easy axis as discussed in subsection 2.2.3.

2.2.2 Magnetic properties of ultrathin Co film

The general physical problem of change of the system properties when one or more of its dimensions is reduced to the scale comparable with unit cell has been investigated for the case of ultrathin magnetic films of cobalt. Finite-size scaling theory[144,145,146,147] predicts that the Curie temperature of magnetic Co films will decrease from the bulk value with the film thickness reduction.

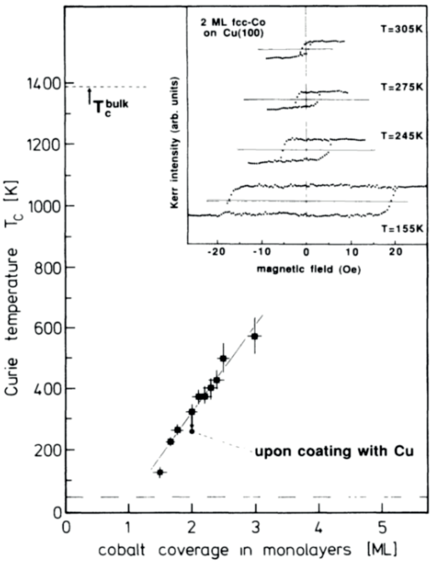

Figure 2.7: Coverage dependence of the Curie temperature of face-centered-cubic (fcc) Co films as determined from the magneto-optic Kerr effect (MOKE) experiments. Inset: Variation of the hysteresis loops of a 2ML film with sample temperatures.[148]

C. Schneider *et al.* presented experiments on ferromagnetic Co monolayers showing a decrease of T_C with film thickness as depicted in Figure 2.7.[148] Through the electron-beam evaporation in UHV ($<2\times10^{-10}$Torr), the fcc Co monolayers were deposited on atomically flat Cu(100) surfaces. The phase transition in bulk fcc cobalt occurs at the temperature T=1388K. The results in Figure 2.7 show a dramatic decrease from $T_C\approx$500K (2.5ML) to $T_C\approx$130K (1.5ML). In lowest thickness limit, a single Co monolayer did not exhibit a ferromagnetic signal above T=50K which is the lowest temperature observed in this experiment. The authors concluded that the magnetic properties of these Co films, such as T_C, coercive force, and magneto-crystalline anisotropies, were strongly influenced by the substrate surface and structural defects in the layer.

Besides the phenomenological analysis, *ab-initio* simulation revealed as well a difference of the density of states (DOS) in ultra-thin Co films in comparison to the bulk. From the Stoner model, the DOS shape of materials near E_F determines the average spin moment per atom and the strength of the ferromagnetism. As Figure 2.8 shows, the DOS from Co bulk[150] is different from the simulation results in freestanding Co monolayer or the ones deposited on noble metal substrates[151] which implies a difference in magnetic properties. Furthermore, comparison of DOS in Figure 2.8 (b)&(c) illustrates the importance of interfaces for the ultra-thin film with a few ML thickness. The sensitivity of the monolayers to the interfacial conditions results in significant changes of properties, which are exploited in experiments presented in Chapter 5 and 6[149].

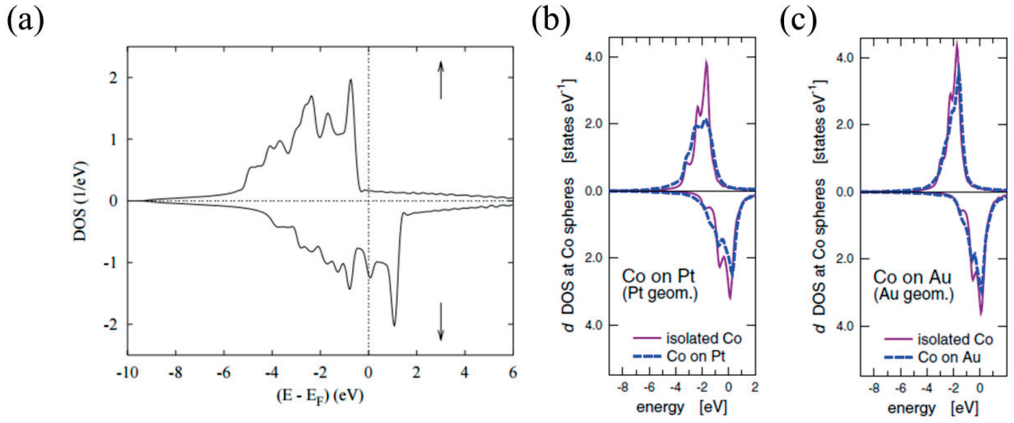

Figure 2.8: (a) Spin-polarized DOS of fcc cobalt bulk[150]; Spin-polarized DOS of 1ML fcc Co films freestanding or on Pt with Pt geometry (b), and on Au with Au geometry (c)[151].

2.2.3 Magnetic anisotropy in (Ga,Mn)As and Co thin films

The zinc blende structure of (Ga,Mn)As is cubic which means a fully relaxed

(Ga,Mn)As layer would have the natural cubic isotropy. The lattice constant variation between GaAs (0.566 nm) and MnAs (0.598 nm) implies compressive strain for the epitaxial films grown on GaAs substrate and tensile strain for films deposited on top of (In,Mn)As[152]. Through measuring the magnetic hysteresis with different field orientations, A. Shen *et al.* proved that the *compressive* and *tensile* strains induce *in-plane* and *out-of-plane* orientation of magnetization in (Ga,Mn)As layer, respectively.[153] The observed anisotropy includes the contributions from the natural cubic anisotropy of the (Ga,Mn)As zinc-blende structure and a uniaxial anisotropy attributed to the effects of surface reconstruction.

For obtaining a DMS thin film with out-of-plane (OOP) anisotropy, the phosphorous doping is used to decrease the lattice constant below the value of GaAs. The X-ray diffraction (XRD) characterization of the P, Mn co-doped MBE-grown (Ga,Mn)(As_{1-y},P_y) (y=0.1, 0.2, 0.3) thin films showed the lattice constant decrease below 0.566nm, which corresponds to the tensile strain.[154] The magnetic anisotropy in the films with tensile strain was shown to induce OOP direction of the easy magnetization axis as confirmed by magnetic hysteresis loops and MOKE microscopy.[155] Further experimental investigation demonstrated that OOP anisotropy occur in fully annealed (Ga,Mn)(As_{1-y},P_y) films while the as-grown samples show the in-plane (IP) easy axis.[156]

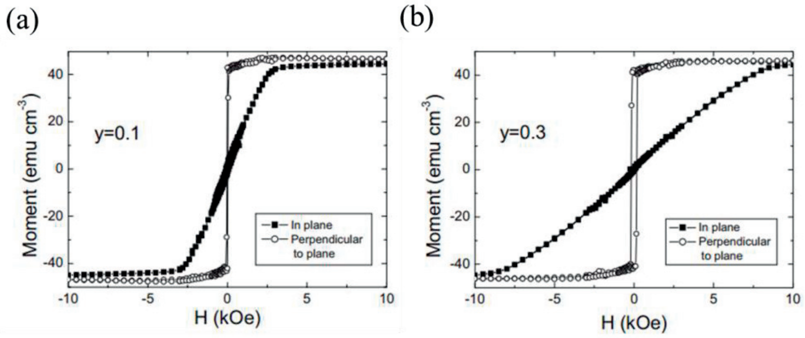

Figure 2.9: Magnetic hysteresis loops measured at 2K when the external magnetic field applied in the plane and perpendicular to plane for annealed ($Ga_{0.94}Mn_{0.06}$)($As_{1-y}P_y$) layers with (a) y=0.1 and (b) y=0.3.[154]

In cobalt thin films, the magnetic anisotropy has a complicated behavior that depends on many parameters.[157,158] Generally, the anisotropy is determined by competition between surface and bulk contributions, hence the effective anisotropy coefficient in thin film can be represented as:[159]

$$K^{eff} = K^{v} + \frac{K^{s}}{t} \qquad (2.20)$$

where t is the thickness of film, K^s and K^v are surface and bulk anisotropy coefficients. Due to its inverse proportionality to the film thickness, the surface anisotropy contribution prevails in ultra-thin Co films resulting in out-of-plane direction of the easy magnetic axis. For thicker films, the in-plane easy axis is typically observed, the crossover between two direction being around, t_c=11.5Å for Au/Co/Au sandwich multilayers. Easy axis of anisotropy lies in the film plane at higher thickness and rotates to perpendicular direction in thinner samples.[158]

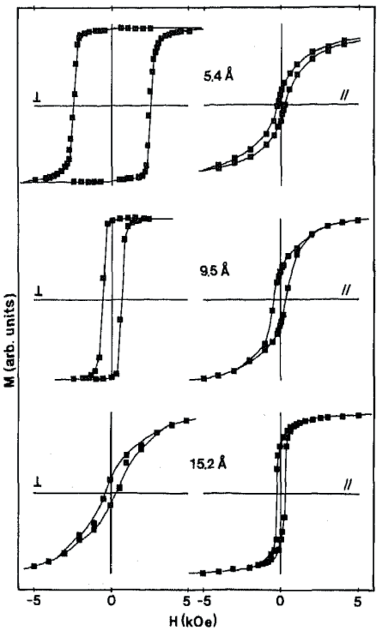

Figure 2.10: Hysteresis loop for magnetic field *H* perpendicular (⊥) or parallel (//) to the film plane for Au/Co/Au multilayers with various Co thickness *t*=5.4Å, 9.5Å and 15.2Å, at *T*=10K.[158]

In addition to the variation of the film thickness there are other methods to control the magnetic anisotropy. S. Monso *et al.* proposed a technique based on control of oxidation of an insulating barrier of a trilayer composed of Pt/Co/MO_x (where *M* is a metal: Al, Mg, Ta, etc.).[160,161] The interpretation of this effect was based on the oxidation-induced asymmetry of 3*d* orbitals in Co. The charge transfer between Co and O[162,163] in optimally oxidized Co/AlO_x interfaces increases the asymmetry of the Co 3*d* bands, reducing the energy of the 3*d* orbitals responsible for the out-of-plane anisotropy and creating a splitting between in-plane and out-of-plane 3*d* orbitals.[164] Thus, in spite of a weak spin-orbit coupling of oxygen atoms, this strong band splitting could lead to a measurable perpendicular magnetic anisotropy.[165]

2.2.4 Anisotropic Magnetoresistance (AMR) in (Ga,Mn)As and Co thin films

DMS like (Ga,Mn)As and related materials are of particular interest for exploring AMR because of both fundamental and practical reasons. This is one of the few groups of magnetic materials where a theoretical analysis of microscopic mechanisms of AMR has been successfully carried out.[124] That was possible because of the relatively simple band structure near the Fermi level and strong spin-orbit coupling in this material.[166,167] From experimental perspective, (Ga,Mn)As and related materials are perfectly suitable for verification of the theoretical predictions. The well-established technology of molecular beam epitaxy allows to continuously vary the strain conditions, magnetic doping and carrier concentration influencing AMR through magnetic anisotropy change.

The symmetry considerations, which are essential for understanding magnetotransport phenomena, enter in AMR analysis in two ways: symmetry with respect to the magnetization direction and symmetry with respect to the major directions determined by the material structure (e.g. crystallographic axis). Therefore the contributions to the measurable AMR are classified in two groups: "non-crystalline" and "crystalline" contributions.[166] The former depends only on the angle between magnetization *M* and the current *I*, while the latter is determined by angles between *M* and the crystallographic axes. Thus for description of AMR, two angles need to be defined: ϕ the angle between *M* and *I* and ψ the angle between *M* and a selected crystallographic direction as [110] crystallographic direction. With the magnetization rotating in the sample plane, the longitudinal and transverse resistivity can then be written as: [169]

$$\frac{\Delta\rho_{xx}(\phi,\psi)}{avg(\rho_{xx})} = C_I \cdot cos(2\phi) + C_U \cdot cos(2\psi)$$

$$+C_C \cdot cos(4\psi) + C_{I,C} \cdot cos(4\psi - 2\phi) \qquad (2.21)$$

$$\frac{\Delta\rho_{xy}(\phi,\psi)}{avg(\rho_{xx})} = C_I \cdot \sin(2\phi) + C_{I,C} \cdot \sin(4\psi - 2\phi) \qquad (2.22)$$

where C_I is the non-crystalline contribution, C_C and C_U the crystalline cubic and uniaxial components and $C_{I,C}$ the mixed crystalline/non-crystalline contribution. $avg(\rho_{xx})$ is the value of ρ_{xx} averaged of a 360° rotation of *M*. The terms of higher order in ϕ and ψ were found to be negligibly small in (Ga,Mn)As devices.

From the above equations, the different contributions to AMR cannot be separated by a single measurement. However it was demonstrated, that the different combinations of AMR constants can be extracted by combining measurements from two or more Hall bars with different current orientations[169].

A semi-quantitative analysis of AMR in (Ga,Mn)As has been carried out using Boltzmann transport theory under approximation of spherical Fermi surface and no dependence of the crystalline and strain anisotropies.[168] The resulting prediction describes the AMR dependence on the parameter, which represents the ratio of the effective strengths of non-magnetic to magnetic charge carrier scattering:[169]

$$AMR = \frac{20\alpha^2 - 1}{24\alpha^4 - 2\alpha^2 + 1} \tag{2.23}$$

where α is the ratio of the effective strengths of non-magnetic to magnetic scattering. This result is in good agreement with the general experimental scenarios despite the severe approximations, like no interstitial Mn, spherical Fermi surface and thus no dependence on crystalline and strain anisotropies.

Figure 2.11 shows the predicted AMR dependence on the magnetic dopant (Mn) concentration and the scattering parameter. This description was found to be in a reasonable agreement with experiment and helped rationalizing the essential observations such as negative AMR for relatively small α and $AMR>0$ for α approaching zero (magnetic metals case, no non-magnetic scattering). On the other hand, this approach does not fully describe the complicated physical picture of AMR in ultra-thin films with very rich magnetic anisotropy and non-negligible crystalline AMR contribution. As a recent research revealed, in ultra-thin films the crystalline term tends to become the primary contributor.[170]

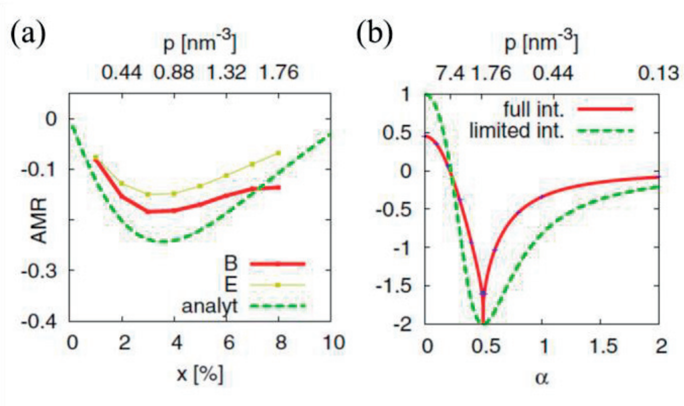

Figure 2.11: Theoretical predictions based on Boltzmann transport theory of (a) non-crystalline AMR magnitude vs. Mn doping and (b) the strength of non-magnetic to magnetic scattering α.[124]

In Co thin layers the magnetoresistance has been studied using Pt/Co/Pt sandwiches with different Co film thickness t_{Co}.[171] Analyzing the thickness dependence of IP and OOP AMR ($\Delta\rho_{ip}/\rho$ and $\Delta\rho_{op}/\rho$) (Figure 2.12) the authors concluded that the AMR signal is dominated by an anisotropic magnetic scattering of electrons at the interfaces.

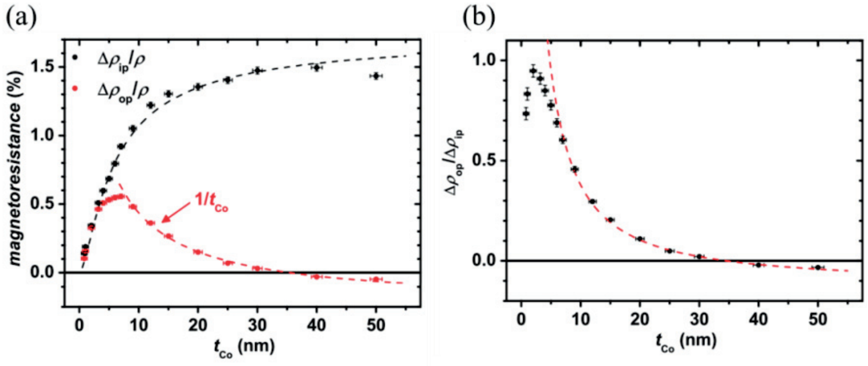

Figure 2.12: (a) Co thickness dependence of $\Delta\rho_{op}/\rho$ and of $\Delta\rho_{ip}/\rho$ behaviors. The dashed lines represent fitting results. The $\Delta\rho_{ip}/\rho$ is related to an increase of the current in the Co layer whereas the shunting through the Pt layer decreases. The $1/t_{Co}$ dependence of $\Delta\rho_{op}/\rho$ indicates that the effect originates from the double Co/Pt interfaces. (b) Ratio of $\Delta\rho_{op}$ and $\Delta\rho_{ip}$. The curve is fitted utilizing the Fuchs-Sondheimer model for $t_{Co}\geq$7nm.[171]

2.3 Field-effect control on ferromagnetism: state of art

2.3.1 Field-effect control of ferromagnetism in DMS thin films

In 2000, H. Ohno *et al.* demonstrated for the first time purely electrostatic control of magnetic properties using a 5nm ferromagnetic (In,Mn)As film as channel in FET structure.[172] The effect was observed below 30K with a rather weak T_C shift by 2K only at a very high gate voltage of ±125V; however this experiment opened the new chapter in magnetoelectric devices.

Further to this ground-breaking work, the focus was shifted to (Ga,Mn)As based magnetic FET structures proposed by D. Chiba *et al.* where higher phase transition temperatures close to 70K were achieved.[173] Using $(Ga_{0.953},Mn_{0.047})As$ thin films with Al_2O_3 dielectric gate, it was possible to lower the operating voltage to ±25V (corresponding to electric field $|E|$=5MV/cm) and reach a T_C shift up to 5K. Theoretical analysis and calculations based on the *p-d* Zener model were in agreement with the magnitude of observed T_C modulation. Both the characterization of the transport data and the MOKE images indicated that the coercive field $\mu_0 H_c$ was determined by the nucleation field $\mu_0 H_n$ and, thus, the change in carrier concentration was found to affect the magnitude of $\mu_0 H_n$.

Targeting a higher degree of control of magnetic properties, M. Sawicki *et al.* improved the dielectric gate in FET devices by using a high-κ material.[141] The Al_2O_3 dielectric layer in the FET structure was replaced by a 40-50nm HfO_2 ($\varepsilon_r\approx$20), resulting in a much higher induced charge and hence stronger field effect sensed by the (Ga,Mn)As layer under the same applied electric field. In further efforts to enhance the gate effect, the total thickness of (Ga,Mn)As was reduced down to 3.5nm. After annealing, T_C was 34K at zero gate voltage, and increased (decreased) to 41K (24K) under a bias of V_G= -12V (+12V). Deeper inspection of the experimental data revealed a coexistence of ferromagnetic-like, superparamagnetic-like and paramagnetic regions. The authors explained the coexistence of magnetic phases by quantum critical fluctuations in the local density of hole states in doped semiconductors. With electronic disorder increasing, the portion of the spins that contribute to the long-range ferromagnetic order diminishes and eventually results in the loss of spontaneous magnetization. Additionally they pointed out that the magnitude of the apparent T_C is determined rather by non-random distribution of magnetic ions than by the fluctuations in the local carrier density.

Along with the T_C shift and the coercivity changing, the field-effect manipulation with the magnetization vector has been reported in (Ga,Mn)As films suggesting that the magnetic anisotropy was controlled in magnetic FETs.[174] The theoretical analysis implied that anisotropic valence band structure was responsible for the anisotropy manipulation by the external electric field.[175]

2.3.2 Field-effect control of ferromagnetism in cobalt thin films

Electrical control at ambient temperature is crucial for device applications, which explains the interest in field-effect control of the magnetic coercivity or anisotropy in metals like Fe[130], FePt/FePd[129] and CoFeB alloys [176], as well as in semiconductors[177,178]. Further to successful control of magnetic properties of DMS at cryogenic temperatures, D. Chiba *et al.* demonstrated the electrical control of the ferromagnetic phase transition in cobalt[179] at room-temperature. In a FET structure consisting of a ferromagnetic stack (2nm MgO/0.4nm Co/1.1nm Pt/3nm Ta) covered by HfO_2 dielectric layer and a gate electrode, electric fields of about ±2MV/cm were shown to be able to generate a 12K T_C shift (318K vs. 330K) slightly above room temperature as illustrated in Figure 2.13. Further analysis suggested that the abruptly falling R^s_{Hall} near T_C is a signature of a 2D ferromagnetic film. The reduction of M near T_C can be quantified by a critical exponent (β) as $M \propto (1 - T/T_C)^\beta$ where the value of β depends on the dimensionality and the number of degrees of freedom for spin orientation. The experimental results gave β=0.160±0.013 which is close to the prediction of β≈0.125 from the Ising model[180] and ≈0.23 from the XY model[181], but far from the estimation 0.365 in 3D Heisenberg model[182].

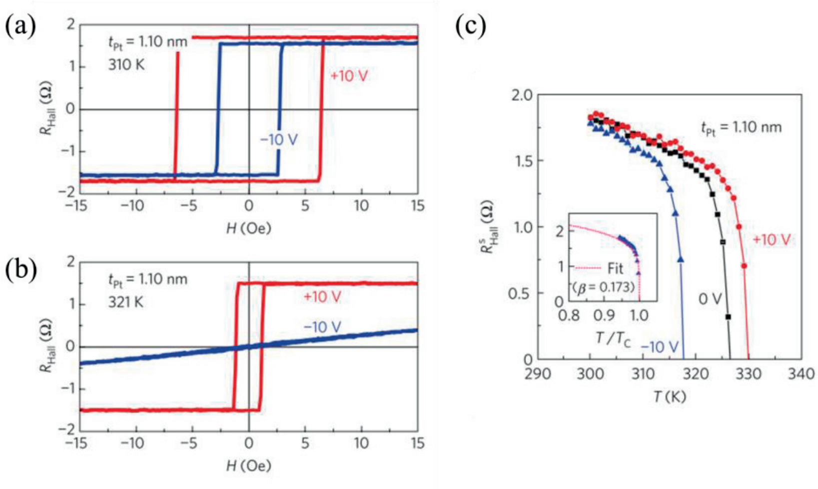

Figure 2.13: Anomalous Hall resistance R_{Hall} loops measured on 0.4nm cobalt film under applied V_G of ±10V at (a) 310K, and (b) 321K near the Curie temperatures. (c) Temperature dependences of spontaneous Hall resistance proportional to spontaneous magnetization, under V_G=+10, 0 and -10V; in the inset the horizontal axis is the normalized temperature T/T_C and the dashed line indicates the fitted curve by using a power-law.[179]

In order to enhance the field-effect control of carrier density in ultrathin metal layers, high-κ HfO_2 gate dielectric was replaced with a material with even higher dielectric permittivity: an ionic liquid film.[183] On a ferromagnetic stack (2nm MgO/0.4nm Co/1.2nm Pt/3nm Ta) similar to the previously discussed experiment, a novel ionic liquid film was deposited[184]. The ionic liquid film contained the following cation and anion: 1-ethyl-3-methylimi-dazolium (EMI^+) and bis(trifluoro-methylsulfonyl)imide ($TFSI^-$). On top of the ionic liquid film a 25μm-thick Pt thin film was placed in order to implement a gate electrode. The analysis indicated that a gate voltage of 1V induced in the magnetic channel a charge density of 12.6μC/cm^2, which is about 7 times larger than that in the FET with 50nm HfO_2 gate driven by 1MV/cm field (V_G=5V). When V_G=0V, the T_C of Co was roughly estimated to be 325K, and was shifted to ~280K and ~380K with -2V and +2V V_G, respectively, i.e. the modulation of T_C was as high as ~100K. This low-voltage control of magnetism at room temperature constituted a significant step towards realizing low-power and low-voltage magnetoelectric devices.

These successful demonstrations of electrical control of the magnetic state in ultra-thin Co film prompted further experiments focused on controlling magnetic domain dynamics, which is of interest for information processing devices. In first domain velocity studies of gated Co channels relatively thick (non-transparent) Au gate electrodes were used. DW propagation velocities were determined by MOKE microscopy from the length of the gate divided by the time of DW passing the whole length of opaque gate electrodes.[185] A range of different gating voltages were applied to the channel in order to gradually change DW velocity, which was measured under different magnetic fields. The detected DW velocities varying from several μm/s to several mm/s indicated that the DW motion was in the thermally activated creep regime. The effective critical field of DW dynamics change increased almost linearly with the V_G. This indicated that the energy associated with the pinning potential randomly occurring in the magnetic channel was modulated electrically.

In order to overcome the experimental difficulties with optical visualization of domains through the non-transparent electrodes, A. Schellekens *et al.* prepared ultrathin 4nm Pt channel crossing the Co channel and inducing field effect at the region of ~220μm×180μm.[186] Such 4nm thickness allowed MOKE microscopy to investigate magnetization reversal from underneath Co in real-time, and the relatively large size of the junctions permitted for accurate optical measurement of DW motion. As depicted in Figure 2.14(a), the unreversed magnetization open windows (light grey) were switched by opposite magnetic field with different speeds that depends on the gate voltage. The data analysis indicated that the electric field altered the height of the disorder-induced pinning barrier. A systematic research on the pinning strength showed that the pinning field changed linearly as a function of applied voltage with the rate 0.22mT/V.[187] A simple micromagnetic 1D model, discussing the electric field distribution creating the step in the anisotropy leading to pinning, in combination with calculations of the electric field distribution[188] demonstrated that not only the magnitude of the electric field but also the width of the electric field distribution at the gate edge was crucial for inducing artificial pinning site. Therefore, DWs could be purely electrically pinned or depinned, which provides wide opportunities to control DWs in experiments and devices, e.g. using the device concept of racetrack memory.

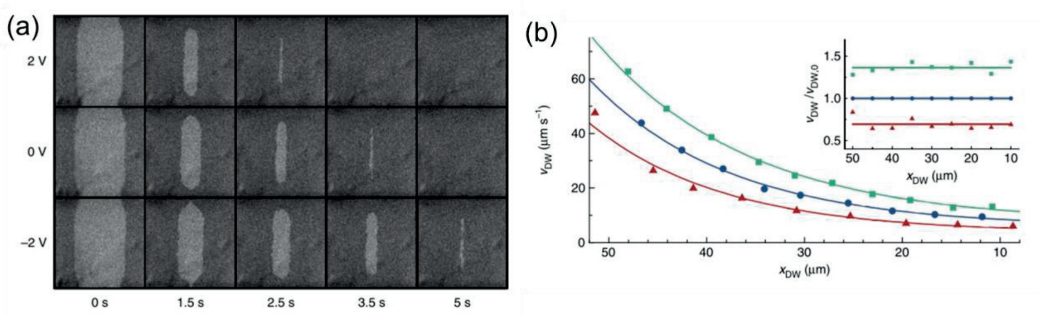

Figure 2.14: (a) MOKE images of magnetization reversal in a constant magnetic field of 23mT for three values of V_G. The magnetization reversed (unreversed) appeared in dark grey (light grey) and the visible part of the junction in each image was ~180μm wide. (b) DW velocity as a function of position at constant B=23mT. Inset: the relative change of DW velocity v_{DW} as a function of DW position x_{DW}.

By using an AlO_x wedge on top of Co thin film, A. Bernand-Mantel *et al.* achieved structures with gradual change of surface magnetic anisotropy energy (MAE) and used these structures for electric field manipulation of the magnetic state.[189] The

AlO_x wedge was formed by oxidizing sputtered Al layer of varying thickness. Gradual change of the degree of oxidation of Co/AlO_x interface resulted in a variation of the magnetic anisotropy of the Co layer so that it was possible to find a region with out-of-plane easy magnetic axis.[165] Generally the less oxidized Co/AlO_x interface resulted in an increase in MAE, which corresponds to a magnetic switching characterized by lower nucleation density. For magneto-optic measurements using MOKE technique, the 7nm Al_2O_3/37nm HfO_2 dielectric bilayer was combined with transparent top gate electrodes of indium tin oxide (ITO).

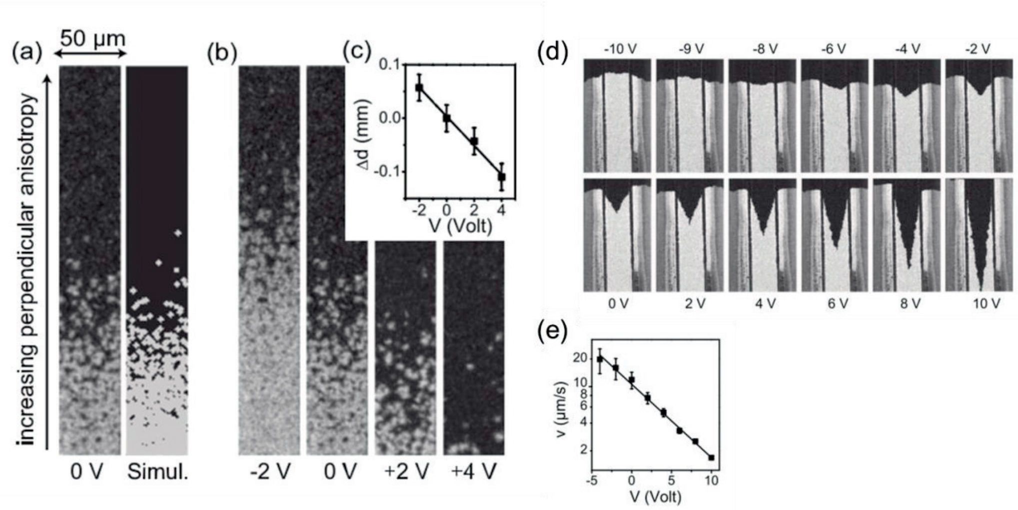

Figure 2.15: (a) (left) and (b) MOKE images recorded through the ITO electrode 200ms after a 1mT constant magnetic field is applied, for different applied voltages. (a) (right) Simulation of the nucleation. (c) Displacement of the 50% reversed zone as a function of the applied voltage. (d) MOKE images of the magnetization reversal below the ITO electrode (center) for various applied voltages. (e) The experimental DW velocities measured below the ITO electrode for different applied voltages. The flat domain wall inside the field-effect region expected for V_G=0 was obtained for V_G= -8V, which may be attributed to the presence of fixed charges inside the dielectric layer.[189]

Figure 2.15(a)&(b) shows MOKE images that represent the magnetic switching within a region with a high nucleation density, where unreversed (reversed) domains appear in dark grey (light grey). The nucleation density is decreasing (indicating an increase in MAE) in the direction where the Co/AlO_x interface gets more oxidized. Monte-Carlo simulations from Néel-Brown model provided a qualitative description of the experimental data for a linear variation of the energy barrier height along the wedge $\Delta E_N/\Delta x$=0.22meV/μm. The influence of the electric field on the nucleation is determined by determining the position where 50% of the magnetization is reversed, which is linearly shifted with a position/voltage equivalence of $\Delta x/\Delta V$=30μm/V. Therefore the equivalence between the electron density reduction and an oxidation increase had been established. Furthermore the voltage influence on DW propagation was investigated in the higher anisotropy (less oxidized) region. The field effect on DW propagation was examined by analyzing the shape of switched domains below the electrode, for different gate voltage. The triangular shape of switched domains below the electrode (Figure 2.15(d)) shows a difference in the DW velocity outside the electrode and below the electrically biased electrode. As shown in Figure 2.15(e), DW velocity below the electrode varied exponentially with V_G implying DW pinning energy barrier modulation by the electric field.

2.3.3 Field-effect control of ferromagnetism in P(VDF-TrFE)/(Ga,Mn)As heterostructure

The use of ferroelectric gates for non-volatile control of ferromagnetism in (Ga,Mn)As presents a major challenge due to the materials incompatibility. In particular for (Ga,Mn)As and related materials, temperatures higher than 250˚C must be avoided since they result in losses of substitutional Mn required for ferromagnetism.[190] Thus for multiferroic devices with (Ga,Mn)As thin film channel, instead of traditional perovskite ferroelectrics the copolymer P(VDF-TrFE) has been used.[191] Its chemical stability and low processing temperature about 130-140˚C made it a suitable gate material for integration on a DMS channel.

The proof-of-concept work showing the polymer/DMS field-effect coupled multiferroics structure was done by I. Stolichnov *et al.* using P(VDF-TrFE)/(Ga,Mn)As heterostructure in 2008.[191] In this FeFET structure, the ferroelectric P(VDF-TrFE) gate showed a sharp polarization hysteresis loop, with a remnant polarization close to 6μC/cm^2. In ferromagnetic FET structures the hysteretic behavior of the magnetization changed in response to the ferroelectric gate polarization. Figure 2.16(a)-(c) show, a significant change of hysteretic anomalous Hall signal between the accumulation and depletion states indicating that the polarization switching alters the magnetic state of the channel. Remarkably for the R_{xy} measured at 60K, the hysteresis cannot be resolved at 60K in the depletion state and above 64K in the accumulation state, suggesting a T_C difference between two states of approximately 4K.

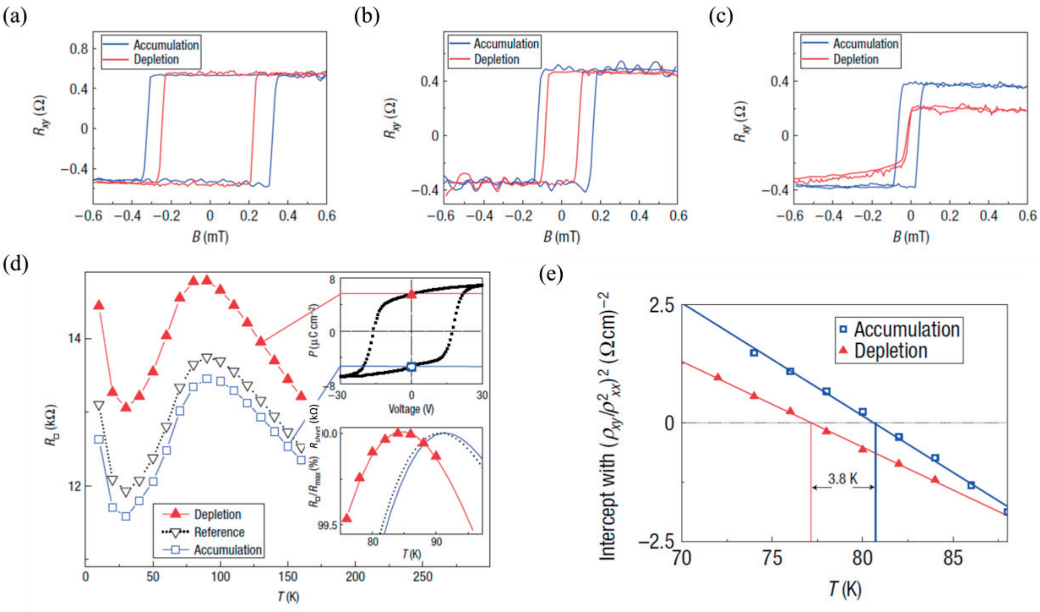

Figure 2.16: The differences in the coercive fields observed from the hysteresis loops of transverse resistance vs. magnetic field for accumulation and depletion states for 50K (a), 56K (b) and 60K (c). (d) Ferroelectric gate operation and temperature dependence of the sheet resistance R_{sheet}; upper inset: polarization hysteresis loop of P(VDF-TrFE) gate driven with 1kHz triangle pulse; lower inset: curves of resistance versus temperature normalized and zoomed in the region around the maximum occurring close to T_C. (e) The intercepts from Arrott plotted vs. temperature, which give T_C of 76.9K and 80.7K, respectively, for depletion and accumulation.[191]

For evaluation of the field effect associated with the switched polarization the sheet resistance of (Ga,Mn)As channel was characterized at different temperatures and opposite ferroelectric polarizations. The resistance of the (Ga,Mn)As films typically shows a weak negative temperature coefficient above the Curie temperature typical for metallic conduction in the presence of weak localization. A reduction of spin-disorder scattering in the ferromagnetic state leads to a resistance peak near T_C, hence the shift of this peak is a signature of T_C change.[192] In Figure 2.16(d) the temperature-dependent resistivities of the channel were compared for the switched gate, in addition with the reference Hall bar where the ferroelectric gate has been chemically removed. The electrical field-effect induced a resistivity change between accumulation and depletion of 9% around T_C. The resistance curve of the reference Hall bar occupied an intermediate position between the accumulation and depletion curves indicating that the channel resistance was not significantly influenced by the trapped charge or any other factors associated with the gate deposition.

To extract T_C of (Ga,Mn)As with high accuracy the Arrott plots technique was used: $(\rho_{xy}/\rho_{xx}^2)^2$ was plotted against $B/(\rho_{xy}/\rho_{xx}^2)$, where B is magnetic field strength.

The zero intercept of the extrapolated linear behavior occurs at T_C. Figure 2.16(e) gives a Curie temperature 76.9K and 80.7K in depletion than in accumulation respectively and a T_C shift ~3.8K (4.7%). (Further details about Arrott plot technique are presented in Chapter 3)

In the experiments described above the 200nm P(VDF-TrFE) gate was polarized by 30V voltage to reverse the field-effect completely. Trying to reach lower operation voltage S. Riester *et al.* implemented ferroelectric FET with same architecture using thinner ferroelectric layers.[193] Using a diluted solution, the spin-coated copolymer layer thickness was reduced to 60nm. The polarization reversal was accomplished at a relatively low voltage ±9.5V. Similar to the previous study, Arrott plots used to determine the accurate T_C shift provided the T_C of 70K and 75K in the depletion and accumulation states respectively (5K shift on T_C). It was shown that the coercive voltage of P(VDF-TrFE) gate could be reduced below 5V, for improved compatibility with the semiconductor circuitry. However this required use of 20-30nm polymer gate, where the risk of breakdown failure becomes significant.[194]

To enhance the ferroelectric gate effect, it is a natural approach to use the thinnest DMS layer to increase the T_C response to the electric field and thus maximize the exploitable capability of P(VDF-TrFE) gate. Due to the difficulty to grow high-quality (Ga,Mn)As layer below 7nm, the ultra-thin samples were obtained by etching of 7nm (Ga,Mn)As raw materials.[195] After every cycle of the surface oxidation in ambient condition wet-etching by 10% HCl resulted in the thickness of (Ga,Mn)As decrease by 0.5nm.[142] From the thinned Hall bar, 3nm (Ga,Mn)As layer still maintained the ferromagnetism with a reasonable T_C ~70K in contrast to the great degradation of T_C down to 30K reported from others[141]. From the Arrott plots a T_C shift of 8.5K was extracted, which was nearly double of the previous results. Furthermore, the exponent ($\partial \ln T_C / \partial \ln R_{sheet}$) gave a value about -0.3 for all channels with different thicknesses (3-7nm). This suggests that the ferromagnetic coupling, even in an ultrathin 3nm channel is still far from the theoretical 2D limit, showing a rather bulk-like behavior similar to well-established 7nm films.

From the magnetotransport data it was possible to estimate the polarization screening at the interface and net charge inducing the non-volatile gate effect. In the conductive channel its sheet resistance is proportional to the hole concentration. The hole concentration in its turn can be tuned by the effective interfacial charge when applying gating voltage. Considering a 5% observed change of R_{sheet} in the multiferroic device between accumulation and depletion states at room temperature, the calculated charge modulation was equal to 1.2μC/cm^2, whereas the total polarization swing in P(VDF-TrFE) is over 12μC/cm^2.[196] To explain the relatively weak 10% effective charge modulation, the polarization screening mediated by two mechanisms has been considered: (a) the depolarization effect and (b) the interfacial charge injection. As discussed in the section 1.3.3, the charge screening in the interface adjacent layer is likely to be a major factor reducing the efficiency of the ferroelectric gate.[102]

Further to successful control of ferromagnetic T_C, the magnetic domain dynamics in ferroelectrically gated DMS channels has been studied.[197] The macroscopic technique of monitoring domain wall propagation was based on analysis of magnetotransport data from (Ga,Mn)(As,P) Hall channel with OOP easy axis. When applying external switching field B along IP directions, there are 4 stages happening for the magnetization M reversal in the channel:[197] (i) M is forced to align along the hard axis (IP) by B, resulting in an IP monodomain state; (ii) As the field is reduced, M rotates towards its easy axis (OOP); (iii) As the signs of the vertical component of B are reversed, M is gradually reversed towards the opposite OOP direction; (iv) At high negative B, M is once again forced along the IP direction. The presence of domain walls is clearly seen in the longitudinal resistance R_{xx}, which displays asymmetric spikes (Figure 2.17(b)) upon magnetization reversal. Poling P(VDF-TrFE) gate significantly changed the domain dynamics: in the accumulation state a spike in the R_{xx} curves was observed at 41K, while in the depletion state at this temperature R_{xx} curve was smooth and the spike shows up only at temperature <38K (Figure 2.17(c)).

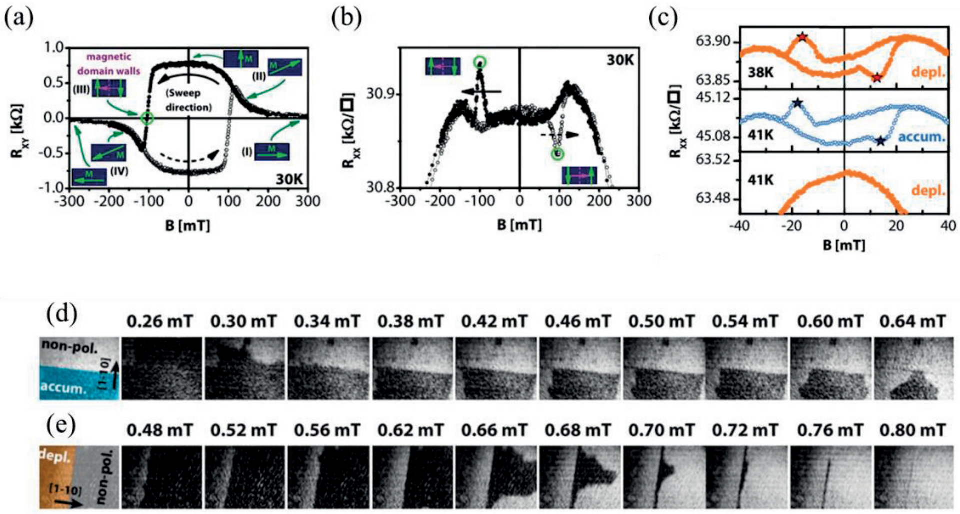

Figure 2.17: The four steps correlated to (a) the Hall resistance R_{xy} and (b) the magnetoresistance R_{xx} plots. The black arrow indicates the direction of B sweep. (c) Near T_C, asymmetric R_{xx} spikes are clearly visible in depletion (38K, upper panel) and in accumulation (41K, second panel). The serial MOKE images for the sample poled (d) in accumulation at 35K (near T_C) and (e) in depletion at 30K (near T_C).[197]

In alternative microscopic approach, the magnetic domains were directly visualized using MOKE microscopy. The specific regions of P(VDF-TrFE) were poled with ±30V using the top Au electrodes, which were chemically removed before MOKE experiment. Poling in the accumulation (depletion) state impeded (facilitated) the ferromagnetic switching as shown in the series of images in Figure 2.17(d) and (e).

In both cases, the boundary of poled/unpoled regions of the polymer gate projected on the magnetic layers as a sharp border between two oppositely magnetized domains. This border remained stable resisting the magnetic domain propagation while the external magnetic field is increased by 0.3-0.35mT, then the monodomain state gradually set on.

2.3.4 Multiferroic P(VDF-TrFE)/Co heterostructure with charge coupling

The highly attractive device concept of field-effect coupled multiferroic heterostructure turns out to be very difficult to implement using Co ultrathin layers because of their sensitivity to processing parameters. First successful experiments show that P(VDF-TrFE) copolymer offers a viable solution for non-volatile field-effect control of magnetism in such channels at room temperature.

The device structure presented by A. Mardana *et al.*[48] included an ultrathin cobalt wedge on glass with a very shallow wedge angle of 2.7×10^{-6}deg covered by 30 monolayers thick P(VDF-TrFE) ferroelectric layer from Langmuir-Blodgett deposition. The sputtered Co wedge had the thickness varied from 8.5 to 27.8Å across the whole 40mm long sample (Figure 2.18(a)). MOKE measurements were used to collect the hysteresis loops at several positions with different Co thickness, and the ratio of the remnant magnetization to the saturation magnetization M_r/M_s was extracted. The hysteresis data strongly suggested that the polarization of P(VDF-TrFE) film had a significant effect on the coercivity and magnetic anisotropy of the Co films. Magnetic anisotropy was altered by as much as 50% by switching the ferroelectric polarization as calculated from OOP and IP hysteresis loops. As depicted in Figure 2.18(b) for the thinnest films, the easy magnetization axis switched between OOP to IP when the ferroelectric polarization was reversed. The change in coercivity was proportional to the ferroelectric polarization, as confirmed by magnetization loops measured at intermediate polarization values. Additional experiments at temperatures above the ferroelectric ordering temperature of the P(VDF-TrFE) showed no changes in the coercivity observed, which confirms the link between the observed change of the magnetic state and the presence of spontaneous polarization.

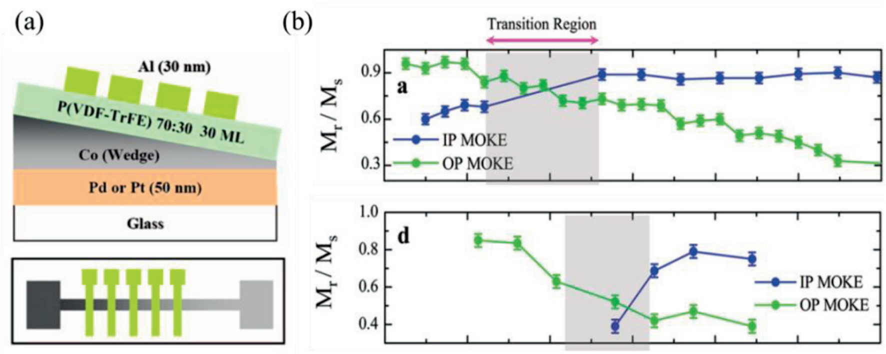

Figure 2.18: (a) Up: schematic side view of the sample: glass/(Pd or Pt)/Co (8.5-27.8Å)/30ML P(VDF-TrFE) 70:30/30nm Al. The Co strip is 40mm long resulting in a very shallow wedge angle of 2.7×10^{-6}deg. Down: schematic diagram of the top view of the sample with bottom Co (gray) electrode and top Al (green) electrodes. (b) M_r/M_s data from MOKE measurement on Pd/Co and Pt/Co samples. OOP and IP M_r/M_s measurements indicate the reorientation region.[48]

Analyzing the nature of the ferroelectric gate effect on ferromagnetism in the Co channel the authors eliminated any role of the magnetostriction. The authors pointed out that a large mismatch in stiffness coefficients between Co and P(VDF-TrFE) exclude any strain-mediated effects so that the observed magnetic changes were solely due to the presence of the electric field.

The experimental efforts in implementing FeFET with ferromagnetic Co channel were supported by *ab-initio* simulations addressing the scenario of purely electric field effect control on ultra-thin Co film.[198] First-principles density functional calculations were used to demonstrate the effect of ferroelectric polarization of PVDF on the magnetocrystalline anisotropy energy (MAE) at the Co/PVDF interface. In this analysis the oxidized Co/O/PVDF interface was considered in order to account for some degree of unintentional oxidation occurring at the Co surface. The differences of spin moments M_s under opposite polarization listed in Table 2.1 indicate that spin moments of Co monolayers are not sensitive to the polarization orientation in PVDF, except for the surface layer Co_0 adjacent to the interface. The change of MAE is due to the change of electronic structure in this layer. The positive sign of the MAE for Co/PVDF implies the easy axis perpendicular to the plane of the multilayer, and the 50% magnitude change of MAE upon reversal of the ferroelectric polarization in PVDF (0.28mJ/m^2 vs. 0.42mJ/m^2) was predicted. In a fully oxidized Co/O/PVDF interface, the quenching of the Co_0 spin moment was due to the chemical bonding of the O monolayer with the Co surface, and the negative sign of MAE showed an IP easy axis consistent with the earlier reported results of the oxygen-induced spin reorientation transition.[199] The oxidation reduced the field effect significantly with 4% change of MAE (-1.16mJ/m^2 vs. -1.12mJ/m^2). Thus the *ab-initio* calculations support the experimental results showing a possibility of field-effect control of ferromagnetism in this Co layers gated by a ferroelectric polymer.

	Polarization					
	Down			Up		
	Co_2	Co_1	Co_0	Co_2	Co_1	Co_0
Co/PVDF	MAE=0.28mJ/m^2			MAE=0.42mJ/m^2		
M_s	1.659	1.689	1.763	1.661	1.696	1.783
L[100]	0.081	0.083	0.107	0.080	0.083	0.108
L[001]	0.085	0.087	0.092	0.085	0.087	0.095
ΔL	-0.004	-0.004	0.015	-0.005	-0.004	0.013
Co/O/PVDF	MAE= -1.16mJ/m^2			MAE= -1.12mJ/m^2		
M_s	1.662	1.740	0.286	1.666	1.740	0.282
L[100]	0.083	0.101	0.003	0.084	0.101	0.003
L[001]	0.082	0.090	0.009	0.083	0.090	0.009
ΔL	0.001	0.011	-0.006	0.001	0.011	-0.006

Table 2.1: Calculated interface MAE values for the Co/PVDF and Co/O/PVDF interfaces and spin and orbital moments (in units of μ_B) of Co atoms. Co_0, Co_1 and Co_2 are three monolayers of cobalt atom from the interface to PVDF sequentially. This table is adopted from Ref. 198.

2.4 Summary

In this chapter ferromagnetism was discussed in context of materials and solutions suitable for implementation of multiferroic heterostructures coupled via persistent field-effect. Analysis of physical phenomena leading to the magnetoelectric coupling and integration issues suggests that two groups of magnetic materials are of interest for ferroelectric gating: diluted magnetic semiconductors (DMSs) and ultra-thin metal layers. The advantage of DMS is that the physics behind field-effect control of ferromagnetism is well understood and the theory allows for quantitative interpretation of the experimental data. The importance of ultra-thin magnetic layers (cobalt) is linked to a possibility of magnetoelectric coupling at room temperature and implementation of multiferroic FeFET using one of the mainstream magnetic materials.

The presented literature review demonstrates that both groups of materials show a strong promise for ferroelectric control of ferromagnetism in multiferroic heterostructures. A significant progress has been reached in manipulating the magnetic state using conventional gates and the results are generally in a good agreement with the theory. The apparent processing incompatibility of DMS and metal magnetic channels with ferroelectrics has been overcome by using ferroelectric copolymers of P(VDF-TrFE) group. The body of results established in Laboratory of Ceramics and in several other groups shows the potential of ferroelectric polymer gates integrated on DMS and metal channels for structures with magnetoelectric coupling. These results constitute a solid basis for exploration of magnetic domain dynamics and deterministic control of ferromagnetism in a wide temperature range addressed in this thesis work.

Chapter 3
Characterization techniques and processing methods

The major part of this thesis work is an experimental study of magnetoelectric coupling in multiferroic structures with (Ga,Mn)(As,P) diluted magnetic semiconductor or Co channels combined with P(VDF-TrFE) copolymer gate. This chapter is composed of two parts. First it presents the characterization methods for evaluation of both ferroelectric and ferromagnetic parts of the multiferroic system. The central experiments of the thesis involve study of ferroelectric control of ferromagnetism using techniques presented in this chapter. The second part of the chapter describes the device fabrication and specific routines for Hall bar processing and ferroelectric gate integration. New approaches for enhanced ferroelectric gates using an additional interface-adjacent hydrophobic layer or high-resistance polymer blends are described and experimentally tested.

I. Characterization methods for ferroelectric and ferromagnetic protagonists

3.1 Ferroelectric characterization using polarization hysteresis loops

The simplest, most important and best established characterization method of ferroelectrics is the testing of polarization-electric field (*P*-*E*) loops.[12] This measurement consists in collection of surface charge induced under the electric fields, normally set as a complete cycle from zero to a maximal positive field, then a maximal negative, and back to zero.[200] In conventional (non-ferroelectric) insulators, the *P*-*E* loop looks like a straight line passing through zero point on the *P*-*E* diagram. As Figure 3.1(a) shows, the typical hysteresis loop in the ferroelectric P(VDF-TrFE) thin film ideally gives the coercive field $E_c=E|_{P=0}$ and remnant polarization $P_r=P|_{E=0}$ by the intercepts on X and Y axis.

The apparent simplicity of *P*-*E* loop concept makes measurement rather simple; however there is a risk of misinterpreting loops with various shapes due to a number of artifacts in particular those associated with leakage. Normally the leakage in ferroelectrics can be estimated by measuring the *P*-*E* loops at different frequencies.[12,201] At low frequencies, the leaky *P*-*E* loops are expected to be of a more round shape as shown in Figure 3.1(b). Thus comparing the *P*-*E* loops taken at different sampling rates, the influence from leakage can be estimated.

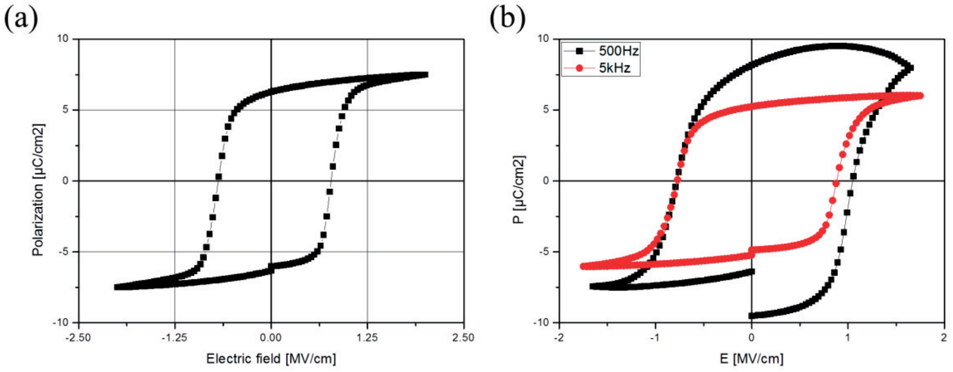

Figure 3.1: (a) A typical ferroelectric hysteresis loop from a 300nm P(VDF-TrFE) thin film. (b) Two *P*-*E* loops taken on the same 200nm P(VDF-TrFE) thin film but with different sampling rates. The black plot, containing 201 data points was recorded with 500Hz, while 5kHz frequency was applied to the red one to eliminate the leakage effect.

The measuring system for polarization hysteresis loops used in this study is based on a LabView program piloting a data acquisition card (DAQ, National Instruments, model: PCI-6030E), with voltage applied through a wide bandwidth amplifier (Krohn-Hite Corp., model 7602M). The charge was collected in virtual ground mode using charge amplifier (Kistler AG, type 5011). A triangular waveform was generated by the DAQ card and amplified by the Krohn amplifier since the coercive voltage V_c for a typical 200nm P(VDF-TrFE) film is ~15V and the sweeping range is set to ±20V. The charge was collected in parallel-plate capacitor geometry using electrodes with area 10^{-3}-10^{-4}cm^2.

There are some particular issues in measuring ferroelectric P(VDF-TrFE) thin films. First, the fresh annealed film requires some “training” before it develops its full switching capacity. For example on the 200nm P(VDF-TrFE) with V_c around 15V, the maximum voltage V_{max} in the first *P*-*E* cycle is usually chosen as 5V. When repeating 5V swing several times, the amplitude of *P*-*E* plots increases steadily. Then V_{max} can be increased by 2-3V each step containing several exercises until V_{max} closing to 1.5 times of V_c, like ~20V for 200nm P(VDF-TrFE), presenting a fully opened *P*-*E* hysteresis loop. The concern of increasing V_{max} rapidly during training procedure is mainly the electrical breakdown where the ferroelectric capacitors get short circuited making further measurements impossible.

Second, the loop frequency has to be slow enough to allow for ferroelectric switching. In the example of P(VDF-TrFE) films, switched with 20V pulse, the switching time is in the millisecond range. A loop period of 0.04 sec (taking 201 measurements with 5kHz frequency) is suitable to get a fully saturated hysteresis loop showing full spontaneous polarization of 6-7μC/cm^2.

3.2 Piezoresponse Force Microscopy

Piezoresponse force microscopy (PFM) technique is an extension of atomic force microscopy (AFM), which probes local electromechanical coupling. Through applying AC signal to the conductive probe and analyzing the response from materials, PFM maps ferroelectric polarization locally with nanometer lateral resolution. In PFM a weak electric field induces a deformation of the crystal lattice via the converse piezoelectric effect. This microscopic deformation is sensed locally by AFM cantilever. Typically in PFM the conductive cantilever is driven with a small AC signal and the mechanical response is detected using lock-in technique. Both amplitude and phase of the mechanical response are essential for ferroelectric polarization analysis. The polarization mapping by AFM is based on the fact that the phase of piezoelectric response changes by 180° depending on the polarization orientation. This reflects the nature of the piezoelectric response, which is proportional to the spontaneous polarization i.e. sensitive to the polarization orientation.

PFM is a useful tool for evaluating ferroelectric properties of ferroelectric gates where conventional polarization hysteresis cannot be measured. Local piezoelectric loops collected by PFM yield the coercive voltage, stability of the switched state and polarization retention.[102] In this work PFM characterization was carried out using an Asylum Research Cypher AFM (Asylum Research). For analyzing P(VDF-TrFE) thin films, very soft cantilevers with spring constant about 0.1-0.3N/m were used at rather low scanning speed <1μm/s in order to avoid damage of the polymer film surface.

The ferroelectric domain writing experiment was done in the Center for near-field microscopy (AFM-STM), Institut Néel, CNRS, Grenoble. During the domain writing, the 2N/m Asylec tips were used. The scanning areas were 15×15μm squares, with the tip speed <2μm/s to make sure P(VDF-TrFE) thin films fully switched. The poling voltage was provided by an external voltage source connected to the tip directly. The uniformity and stability of written polarization domains were verified by subsequent PFM imaging.

3.3 Anomalous Hall Effect in magnetotransport

Ordinary Hall effect

Consider a piece of conductive material in crossed magnetic and electric fields. When the charge carriers move inside the material driven by electric field, they experience the Lorentz force perpendicular to the direction of movement and external magnetic field. If the current I flows in X direction (Figure 3.2), in presence of Z oriented magnetic field, the positive charges are pushed along Y axis while the negative charges marching to the opposite direction, by Lorentz force. In the *p*-type semiconductor (Ga,Mn)As we used, the major carriers are holes carrying positive charge. The positive charge will start to accumulate at the rear surface and the front surface will become negatively charged, resulting in a voltage between front and rear surface called Hall voltage U_H. In Co thin film the carriers are the delocalized electrons with the sign of U_H reversed. The Hall voltage is determined by the equilibrium between Lorentz force and the electric field force originated from the surface charge.

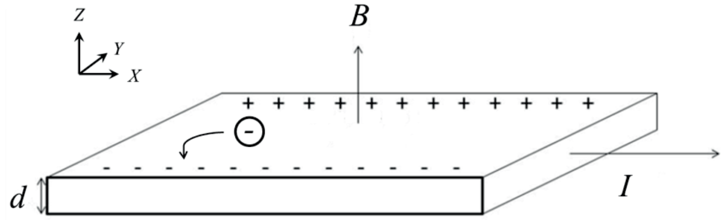

Figure 3.2: Schema illustrating ordinary Hall effect.

The Hall potential U_H and the Hall resistance R_H can be expressed as:

$$U_H = \frac{IB}{pqd},\ R_H = R_{xy} = \frac{U_H}{I} = \frac{B}{pqd} \tag{3.1}$$

where I is the current, B the magnetic field, p the carrier density, q the carrier's charge, and d the thickness of sample. Since the sign of U_H is determined by the sign of carrier's charge q (positive for holes and negative for electrons), Hall effect is usually used to detect the carrier type in materials.

Anomalous Hall effect

Anomalous Hall effect (AHE) is a magnetotransport phenomenon occurring in ferromagnetic materials. In ferromagnetic materials, Hall resistivity ρ_{xy} has two different sources. One is proportional to the applied magnetic field B, the other is proportional to the material's magnetization M:

$$\rho_{xy} = \rho_{OHE} \cdot B + \rho_{AHE} \cdot M \tag{3.2}$$

where ρ_{OHE} and ρ_{AHE} are ordinary and anomalous Hall coefficients. The anomalous Hall coefficient depends on the longitudinal resistivity ρ_{xx} and can be described as:

$$\rho_{AHE} \propto a\rho_{xx} + b{\rho_{xx}}^2 \tag{3.3}$$

The first term comes from so-called skew scattering, which depends on scattering of spin-polarized carriers at non-polarized impurities and at intrinsic crystal potentials[202].The skew scattering contributes to both anomalous Hall resistivity and longitudinal resistivity, so ρ_{AHE} contains one term proportional to ρ_{xx}. The second term depends on side-jump mechanism, describing spin-polarized carriers scattered elastically by the impurity's electric field. The possibility of scattering and its strength are both proportional to ρ_{xx}, resulting the quadratic term.

In ferromagnetic metals and DMS, the experiments revealed the trend of $\rho_{AHE} \propto \rho_{xx}^2$.[168,203] Furthermore for the term $\rho_{AHE} \cdot M$ much higher than $\rho_{OHE} \cdot B$, equation (3.2) can be simplified to:

$$M \propto \frac{\rho_{xy}}{{\rho_{xx}}^2} \tag{3.4}$$

Therefore Hall measurements can be used as a tool to probe magnetization in magnetic materials.

Arrott plot

Arrott plot is a widely used technique of evaluation of ferromagnetic Curie temperature T_C from magnetotransport measurements carried out at different temperatures. If T_C is out of available temperature range of measurements, one can estimate it from Arrott plots via extrapolation procedure. In Arrott plots the square of magnetization M^2 is plotted as a function of B/M, at fixed temperature. Based on Ginzburg-Landau mean field model for magnetism, the free energy in ferromagnetic material close to T_C can be written as:

$$F(M) = -BM + \frac{1}{2}a(T - T_C)M^2 + \frac{1}{4}bM^4 \tag{3.5}$$

where $a,b>0$ are arbitrary constants. A stable state of system requires $dF/dM=0$, leading to the following equation

$$bM^2 = \frac{B}{M} - a(T - T_C) \tag{3.6}$$

A standard Arrott plots measurement is illustrated in Figure 3.3, representing a series of data from (Ga,Mn)As thin films plotted in coordinates M^2 vs. B/M.[113] The asymptotic of linear part at high B is used for T_C estimation. The sign of its intercept with Y-axis changes at T_C. Thus the positive intercept corresponds to the ferromagnetic phase and negative signals the paramagnetic state of the material.

Most of the magnetotransport experiments were carried out using a conventional electromagnet (Bruker B-E15v) delivering magnetic fields up to 1.4T and a closed-cycle Janis cryostat providing the temperature range from 4K to 325K. The temperature was regulated with LakeShore temperature controller (model 331). A source-meter (Keithley Instruments, Inc., model 2636A) and multimeters (Hewlett

Packard, model 3478A) were used for magnetotransport measurements, in constant-current and constant-voltage regimes. The entire system was piloted by LabView program, which enables control of temperature and magnetic field as well as data acquisition.

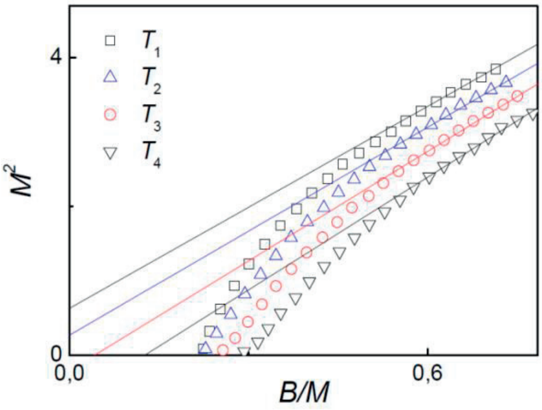

Figure 3.3: An example of Arrott plots measured around T_C. The four plots represent data for $T_1<T_2<T_3<T_4$, showing ferromagnetic state (T_1, T_2) and paramagnetic state (T_3, T_4) as seen from the sign of intercept.[113]

3.4 Anisotropic magnetoresistance (AMR) measurement: crystalline and non-crystalline contributions

For exploring very weak magnetic response of ultra-thin films close to Curie temperature AMR represents a valuable and sensitive tool that helps detecting even very faint changes of the magnetic state. As discussed in subsection 2.2.4, in order to rationalize the generally complicated angular dependence of AMR, it is very useful to single out the “crystalline” and “non-crystalline” contributions to the AMR signal. The former depends on the angle between magnetization M and the crystallographic axes, whereas the latter is governed by the angle between M and the current I. In many cases, the easy magnetization axis in the DMS thin layers lays in-plane and therefore the in-plane geometry of AMR measurements is widely used. Figure 3.4 shows the AMR geometry and angular diagrams of typical AMR signal as presented in Ref. 166, for current parallel to the main crystallographic directions.

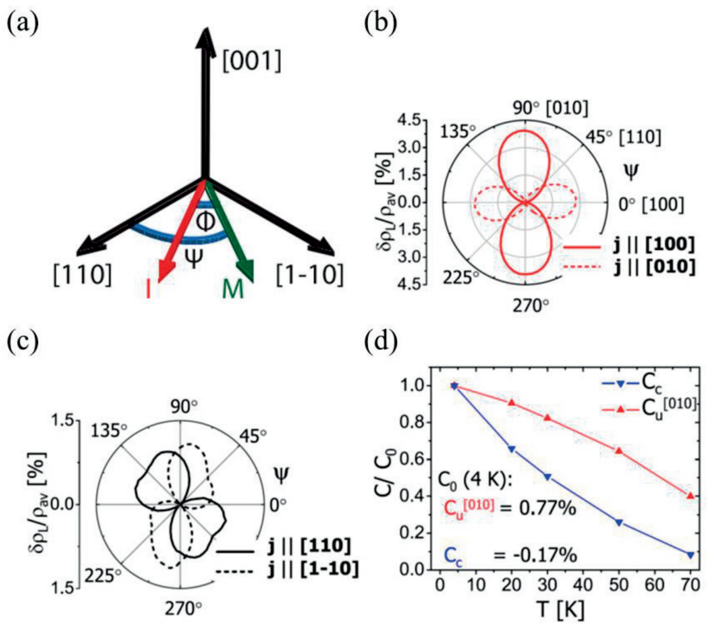

Figure 3.4: (a) Angle notation for the in plane AMR geometry. (b) and (c) Angular diagrams of AMR curves for longitudinal resistance at B=4T, with the current oriented along [100] and [010] in (b), [110] and [1-10] in (c). (d) Temperature dependence of the extracted crystalline components C_U and C_C.[166]

Following the notation for magnetization rotated in the sample plane,[166] one describes AMR using angle ϕ between M and I and angle ψ between M and [110] crystallographic direction. According to the analysis from Ref. 169, the angular dependence of longitudinal and transverse resistance can be expressed as a function of these two angles, for the magnetization rotating in plane as follows:

$$\frac{\Delta\rho_{xx}(\phi,\psi)}{avg(\rho_{xx})} = C_I \cdot cos(2\phi) + C_U \cdot cos(2\psi)$$

$$+C_C \cdot cos(4\psi) + C_{I,C} \cdot cos(4\psi - 2\phi) \tag{3.7}$$

$$\frac{\Delta\rho_{xy}(\phi,\psi)}{avg(\rho_{xx})} = C_I \cdot \sin(2\phi) + C_{I,C} \cdot \sin(4\psi - 2\phi) \tag{3.8}$$

Here $avg(\rho_{xx})$ stands for value of longitudinal resistance averaged over 360° rotation of the magnetic moment, C_I, C_U, and C_C are non-crystalline, uniaxial and cubic crystalline contributions, respectively.

A rather complicated angular dependence originating from these equations can be significantly simplified by choosing directions of the current parallel to the principal crystallographic axes. In this study the Hall bar axis, which determined the current direction is [1-10]. In this case replacement of ϕ by $\psi+\pi/2$ leads to the angular dependence of ρ_{xx} given by a simple function of only one angle ψ:

$$\frac{\Delta\rho_{xx}(\phi,\psi)}{avg(\rho_{xx})} = \left(C_U - C_I - C_{I,C}\right) \cdot cos(2\psi) + C_C \cdot cos(4\psi) \tag{3.9}$$

$$\frac{\Delta\rho_{xy}(\phi,\psi)}{avg(\rho_{xx})} = \left(-C_I + C_{I,C}\right) \cdot \sin(2\psi) \tag{3.10}$$

The relative contribution of crystalline and non-crystalline contributions in DMS strongly depends on the sample geometry. In relatively thick films (starting from hundreds of nm) the non-crystalline contribution is shown to be predominant. As the film thickness decreases, the role of crystalline contribution tends to grow and in ultra-thin films (≤20nm) it dominates.[169] This crystalline contribution was shown to be particularly sensitive to the external control e.g. using strain imposed on the magnetic layer via the piezoelectric transducer. The responsiveness of AMR signal in ultrathin DMS films to the external stimuli is exploited in this chapter for detecting magnetic anisotropy change induced by the ferroelectric gate.

3.5 Magneto-Optic Kerr Effect

In 1877, John Kerr discovered the influence of magnetized media on the reflection of linearly polarized light which leads to an elliptical polarization.[204] The magneto-optic Kerr effect (MOKE) measurement is now an established optical technique used to probe the magnetic state and visualize magnetic domain arrangements. S. Bader *et al.* invented MOKE microscopy to study the surface magnetization in microscopic scale.[205]

In MOKE microscopy, the linearly polarized light is generally used, which can be decomposed into left-handed and right-handed circularly polarized light with equal amplitude. These two modes have different complex reflection coefficients r^L and r^R. Upon reflection from a magnetized medium the linearly polarized light gets Kerr rotation α_K and a Kerr ellipticity ε_K:

$$\alpha_K = -\frac{1}{2}\left(arg(r^L) - arg(r^R)\right),\ \varepsilon_K = -\frac{|r^L| - |r^R|}{|r^L| + |r^R|} \tag{3.11}$$

Upon magnetization reversal, both the α_K and ε_K change sign, therefore MOKE can be exploited to characterize the magnetization in thin films. The most practical cases can be classified in three Kerr configurations: polar, longitudinal and transverse geometries as shown in Figure 3.5(a). For analyzing the magnetic Co thin film with out-of-plane anisotropy used in this thesis, the polar MOKE is the technique of interest.

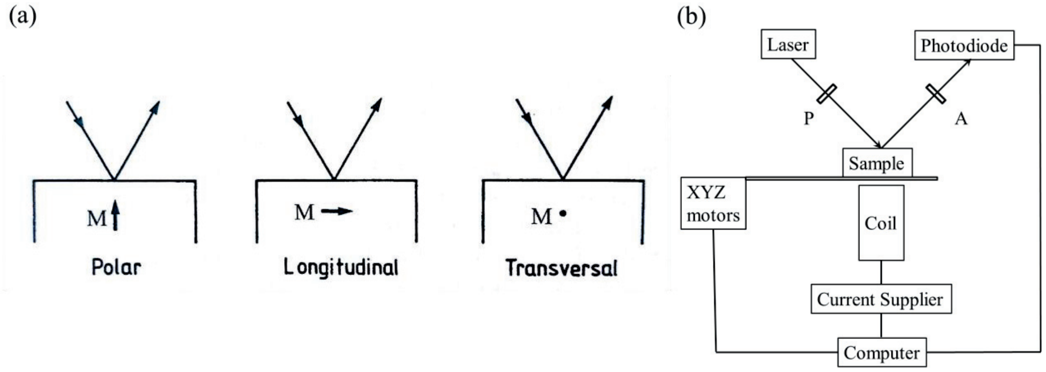

Figure 3.5: (a) Orientation of the magnetization and incidence plane for three main Kerr geometries.[182] (b) Schematic illustration of a MOKE microscopy setup.

In MOKE experiments (Figure 3.5(b)), the laser light becomes polarized after passing through the first polarizer “P”. Subsequently it is reflected from the sample surface and its intensity is detected by the photodiodes which transfer the detected signal to the computer. Between the sample and the photodiode, the second polarizer “A” is inserted with an angle δ rotated from the extinction position. The computer-controlled current source generates a magnetic field in the coil. The precise positioning of the sample is controlled by the XYZ three axis motors.

In this experiment, the intensity I measured by the photodiode after the polarizer “A” can be written as:[182]

$$I = I_0\left(1 - \frac{2\alpha_K}{\delta}\right) \tag{3.12}$$

where I_0 is the intensity with zero Kerr rotation. Since the Kerr rotation α_K is proportional to the magnetization, the intensity difference carries the information about the magnetization change.

For the particular MOKE setup in Institut Néel, CNRS, Grenoble, where the measurements in this work were done, the light source contains three lasers with red, green and blue colors. All the MOKE experiments described later used the blue laser. Similar to a normal optical microscopy configuration, the incident and reflected light were vertical to the sample surface. A CCD camera replaced the photodiode to receive the optical image. The used coil contained a soft ferromagnetic core but the remnant magnetization was considerable even at the low field measurements, which required further correction when converting galvanometer number into the effective magnetic field. The sample was fixed by double-side tape on a piece of glass slide activated by XYZ motors, which were manipulated from tangible switches or by virtual bottoms in computer program. The signals from the CCD camera, the current supplier and the coordinators of XYZ motors were compiled into a LabView program (created by Laurent Ranno).

The raw images obtained in MOKE experiments have usually too low contrast to show the magnetization change or magnetic domains in the sample. The unprocessed image taken by the camera is shown in the left picture of Figure 3.6. It contains surface topography information mixed with the magnetization signal. By appropriate image processing technique, the useful information about magnetic domains can be extracted and enhanced. At first, for calibration purpose a “background” image of the sample surface is recorded, normally with saturated magnetization generating by a strong field, i.e. monodomain state. After applying the magnetic field, the domain patterns in the sample start to evolve from the initial configuration. By subtracting this new image from the background, the signal depending on shape or other non-magnetic origins is suppressed, whereas the magnetic domain evolution data remain in the output. Thus the processed image highlights ferromagnetic information, showing magnetization switching as shown in the right panel of Figure 3.6. In this image the grey part is where magnetization is not switched yet, and white areas are newly formed magnetic nuclei reversing their magnetization from the original monodomain.

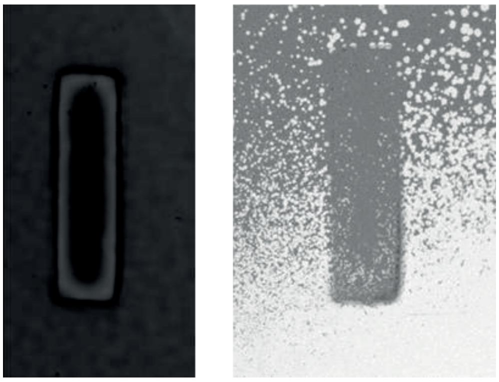

Figure 3.6: The images from MOKE microscope. Left is the “background” image from CCD camera, illustrating a transparent electrode in the center; the right figure is the processed (differential) image enhancing the visibility of the magnetic domains. Adopted from Ref. 149.

3.6 Monte-Carlo Simulation

Monte Carlo method is a computational algorithm to obtain numerical results through vast repeated random sampling. It is used in a wide range of physical problems and especially useful when the problem is difficult or impossible to approach via other numerical methods. In this thesis, Monte Carlo simulation is used to study the probability distribution for nuclei in magnetic film with generating draws from the computer calculation results.

The material background and physical scenario addressed in the simulation work is summarized below:

1) Material background: an ultra-thin Co film with out-of-plane magnetic anisotropy, covered by a partially oxidized AlO_x wedge. The gradual variation of the Co/AlO_x interface oxidation changes the anisotropy and nucleation energy of the Co layer.
2) Pretreatment: the whole Co film is magnetized into a monodomain state, i.e. the magnetization is parallel everywhere in the magnetic layer, ready to be reversed later.
3) Reversal Stage I in Simulation: with applying a weak opposite magnetic field, the magnetization in Co starts to switch. At first, only a few small regions in Co, so-called nuclei, reverse their magnetization depending on their nucleation energy. Monte-Carlo method gives the nucleation distribution on the film.
4) Reversal Stage II in Simulation: the nuclei expand their volume under the constant magnetic applied, known as domain wall propagation. The growth process is simulated based on the result from *Stage I*.

In order to analyze the nucleation density distribution in the ferromagnetic ultra-thin Co film, a Matlab program was used. In this numerical experiment, the nucleation probability can be written as:

$$P = 1 - e^{-\frac{a}{X}},\ X = X_0 e^{-Y} \tag{3.13}$$

where P is the nucleation probability, a and X_0 the constants, X and Y the tunable parameter related to the material properties in calculation.

To initialize the calculation, the values of a and X_0 need to be defined at the beginning of program. And an $A\times B$ pixel matrix is generated, representing the region where the nucleation density is studied. Considering the progressive variation of the Co/AlO_x interface oxidation that impacts the nucleation energy,[189] the parameter Y (nucleation energy) is set to linearly increase along the longitudinal direction of pixel matrix. This linear approximation of the nucleation energy change along the wedge was shown to be adequate for simulating the behavior of real samples.[189]

II. Fabrication process of multiferroic heterostructures

3.7 Fabrication of Hall bars on (Ga,Mn)(As,P) film with ferroelectric polymer gate

The two protagonists in our multiferroic heterostructures are (Ga,Mn)(As,P) and

P(VDF-TrFE). The $(Ga_{0.94},Mn_{0.06})(As_{0.9},P_{0.1})$ was grown by molecular beam epitaxy (MBE) at the School of Physics and Astronomy, University of Nottingham.[154] Firstly a 50nm $GaAs_{0.9}P_{0.1}$ buffer layer was grown on a GaAs(001) substrate. Immediately 25nm $(Ga_{0.94},Mn_{0.06})(As_{0.9},P_{0.1})$ was added on the top. The growth was done at a low temperature of 230˚C. Additional technical details can be found in Ref. 154.

The ferroelectric gate layer was prepared by spin-coating technique from P(VDF-TrFE) solution. The precursor consisted of 77:23 molecular ratio copolymer of vinylidene fluoride (VDF) and trifluoroethylene (TrFE) in granule form, bought from Solvay Solexis S.A.. The copolymer powder was dissolved in methyl ethyl ketone (MEK) at 60˚C water bath under stirring for 24h. Depending on the desired gate thickness, the concentration of P(VDF-TrFE) varied from 0.2 wt% to 3 wt%. The most common processing receipt was to spin 2 wt% P(VDF-TrFE) solution at 1800rpm speed for 70s to have 200nm thick layer. After ~135˚C annealing for 7-10min, the amorphous copolymer layer transformed into the ferroelectric phase.

For fabricating Hall bar structure on (Ga,Mn)(As,P) layer, several steps involving photolithography were necessary as described below. The photolithography resist used was AZ5214 with MF-319 developer. All photolithography works described in this section were done in the clean room of Institute of Condensed Matter Physics (ICMP), EPFL.

First the contact electrodes of the Hall bar were deposited on the (Ga,Mn)(As,P) layer. This stage includes 3 steps as following:

1) Mask preparation: The masks were prepared on a 5×5 inch quartz substrate by Dr. S. Riester, including the patterns for the contact electrodes, the Hall channels on the semiconductor layer and the top gate electrodes.

2) Photolithography I: The receipt used for resist coating consisted of 30s spinning at 5000rpm speed (parameters on spin-coater panel: 3, 30, 500). A baking step followed, leaving the resist 3min at room temperature followed by 3min at 90˚C on a hotplate. After 2.0 sec exposure, 115˚C/60s post-baking and 15s exposure were applied to reverse the polarity of the AZ5214 from positive to negative. After 90s in the developer, the patterns were ready and were transferred from the quartz mask to the sample surface.

3) Metal deposition: 15nm Ti and 100nm Au were deposited by electron-beam evaporator over the surface of developed resist, with the rates around 2.5Å/sec and 5.5Å/sec separately.

4) Lift-off: The residual resist (with metallic layers above it) was removed by soaking 4min in acetone under ultrasonic waves. This left the well-defined contact electrodes tightly bonded to the DMS layer (Figure 3.7(a)).

The purpose of the following second lithography was to curve the outline of Hall channel (2300×180µm) on the (Ga,Mn)(As,P) layer. This work was done in 2 steps:

1) Photolithography II: Resist spinning during 30s with 5000rpm speed, 5min drying at room temperature and 5min baking at 90˚C. Exposure time varied between 2.5s and 3.5s, depending on the age of the resist. Developing procedure was shortened to 75s relative to *Photolithography I*. Resist removal was done leaving residual resist to define the channel patterns as shown in Figure 3.7(b).

2) Etching of (Ga,Mn)(As,P): Wet-etching was done by the solution of 3mL H_2O_2 and 3mL ammonium in 300mL DI water. The etching consisted of no less than 25s etching and twice 20s rinse in DI water. This resulted in the structure shown in purple in Figure 3.7(b) of (Ga,Mn)(As,P) bar raised above the GaAs substrate. After cleaning by acetone and DI water, the Hall bar was ready for gate deposition.

To deposit the ferroelectric gate, the common spin-coating receipt of P(VDF-TrFE) (2 wt% solution, 1800rpm/70s) was used, yielding a 200nm thick film. In order to obtain the ferroelectric phase, annealing at 137˚C/10min was applied.

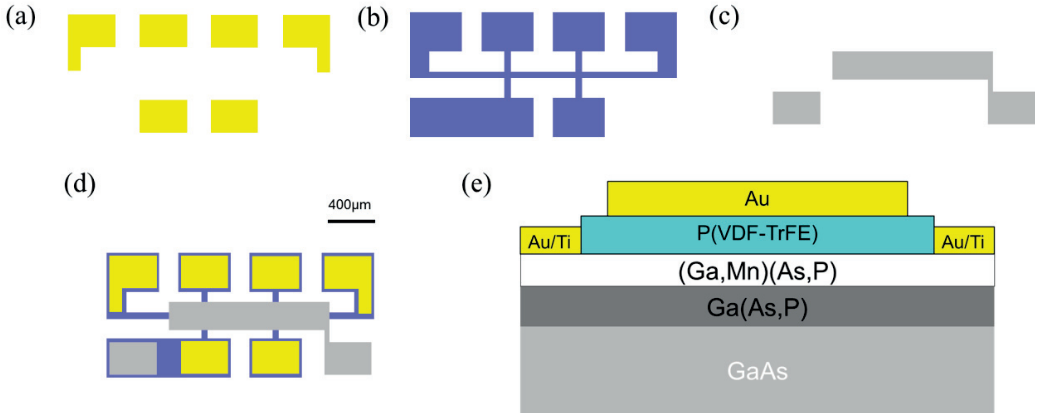

Figure 3.7: (a)-(c) Patterns for the 3 photolithography steps, as the yellow rectangles for the bottom contact electrodes, purple the Hall bar and grey the top gate electrode (d) the final alignment of photolithography structures seen from the top and (e) the schematic cross section of multilayers in the Hall bar.

Finally the top electrodes were prepared in 4 steps:

1) Metal deposition: A top Au layer of 100nm thickness was made by thermal evaporation, with a carefully controlled deposition rate to avoid overheating of the underlying P(VDF-TrFE).

2) Photolithography III: This step was used to create the mask patterns in

Figure 3.7(c). In this pattern, the left rectangle is later used together with the bottom electrode to characterize the ferroelectric layer by *P*-*E* loops, and the right longer one is used for polarizing P(VDF-TrFE) to gate the DMS channel. The resist deposition, baking, exposing and developing were applied with the similar parameters as in Photolithography II.

3) Etching of Au: Following developing, KI/I_2 etchant was used during 30s to remove all the gold outside the resist protection. Then the sample was rinsed in DI water twice and the top gate electrodes were exposed having the pattern shown in Figure 3.7(c).
4) Cleaning residual resist: A 4.0s no-mask exposure and 30s developing was used to clean up the residual resist and to finalize the whole fabrication process of the FeFET-style Hall bar.

3.8 Preparation of a Co magnetic channel with P(VDF-TrFE) cover

FeFET structures for studying multiferroic coupling at room temperature were fabricated based on the same concept but with the ultra-thin cobalt film substituting the DMS channel. The ferromagnetic channel consisted of a Pt/Co/AlO_x wedge stack on Si substrate. Pt layer works as a buffer layer between the Co film and the Si substrate. The ultra-thin Co film is ferromagnetic and sensitive to external electric field. The AlO_x wedge is used not only as a protection layer for Co, but also to adjust its magnetic properties. The gradually changing thickness along the wedge results in a continuous variation of the interface oxidation degree, which entails a magnetic anisotropy change.

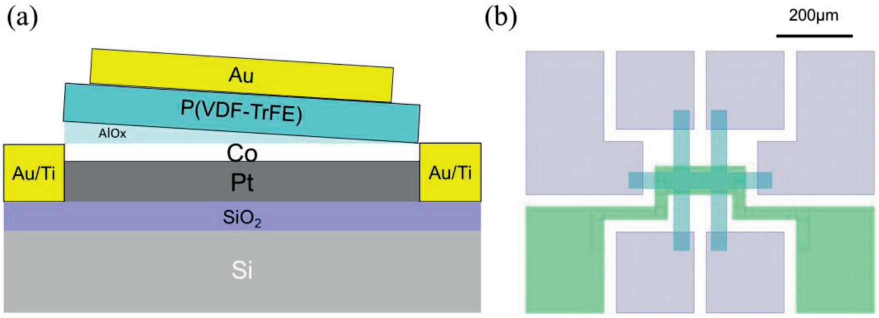

Figure 3.8: (a) Schematic side view of cross section of the sandwich. (b) Top view of Co magnetotransport device.

The 3nm Pt/0.6nm Co/~1.5nm Al wedge stack was deposited on Si substrate by sputtering (Figure 3.8(a)). Through controlling the shutter speed in the sputtering machine, the 1Å/cm linear increase of the Al thickness was achieved along the wedge. Then the Al wedge was oxidized in O_2 plasma, resulting in the formation of a partially oxidized alumina layer.[189] As a result, for an optimum oxidation of the Co/AlO_x interface, the ferromagnetic layer possessed an out-of-plane anisotropy.[206]

After AlO_x formation, the first photolithography was applied on the magnetic layer to draw Hall bar structures (central blue part in Figure 3.8(b)), patterned by ion-beam etching (IBE). Those steps were done in the clean room of Institut Néel, CNRS, Grenoble.

The following photolithography steps were done in CMI, EPFL. To prepare the metal electrodes of the Hall bars first 1.2μm nLOF photo-resist was prepared using the 3000rpm spin-coating receipt of the SSE SB20 manual coating machine, followed by a 115˚C/105s baking. The photolithography exposure took 4.2s (48mJ/cm^2) by Süss MJB4 machine. After a 115˚C/90s post-baking for polarity reversal and developing during 40s in AZ726-MIF, the nLOF resist was well prepared. The 15nm Ti/100nm Au deposition and lift-off process, same as mentioned in the parts of *Photolithography I* of section 3, were made in ICMP to obtain the contact electrodes shown in light purple in Figure 3.8(b).

The deposition of the ferroelectric gate was done using a 2 wt% solution of P(VDF-TrFE) with spinning parameters 1800rpm/70s. This gave us a 200nm thick film. Annealing at 137˚C/10min was applied, allowing for the ferroelectric phase transition in the copolymer.

The last step was to prepare the gate electrodes. Thermal-evaporated 100nm Au was deposited on the P(VDF-TrFE) and then covered by 1μm thick AZ1512 resist. A procedure of 112˚C/90s baking, 2.0s (15mJ/cm^2) exposure and 40s developing were applied. This resulted in the formation of the gate electrode with the pattern shown in green in Figure 3.8(b). Finally Au wet-etching and residual resist removal steps were done, similar to the step descriptions after *Photolithography III* in section 3.7.

3.9 Optimization trials for enhancing ferroelectric gate performance

3.9.1 Placing CYTOP buffer layer between the ferroelectric and the ferromagnetic films

CYTOP is an amorphous fluoropolymer made by Asahi Glass Co., Ltd., having the formula shown in Figure 3.9. With dielectric constant about 2, this material has very high volume resistivity over $10^{17}\Omega$/cm, in contrast to PVDF which has $5\times10^{14}\Omega$/cm. The most attractive feature of CYTOP is that it is a strong water and oil repellent. As water is a known cause of gate bias stress effects, this problem could be eliminated by employing a highly hydrophobic CYTOP gate buffer layer.[207,208] In our heterostructures, CYTOP was placed between (Ga,Mn)As and P(VDF-TrFE) to exclude any moisture on the interface. This helped to minimize polarization screening at the interface and improve field effect on ferromagnetic layer.

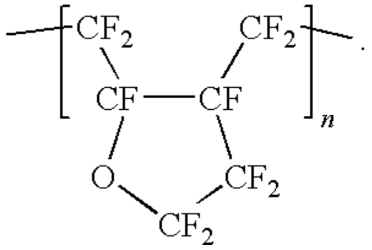

Figure 3.9: The chemical formula of CYTOP. Peripheral fluorine atoms offer excellent water repellent property.

15nm thick CYTOP layer with roughness less than 3nm was spin-coated on (Ga,Mn)As. However the smooth CYTOP layer shows an extremely poor adhesion for P(VDF-TrFE) polymer deposited on it. This problem was solved by moderate plasma treatment to roughen the CYTOP surface. 10W plasma for 1 min was optimal, not etching CYTOP thoroughly but allowing P(VDF-TrFE) solution to stay on it.

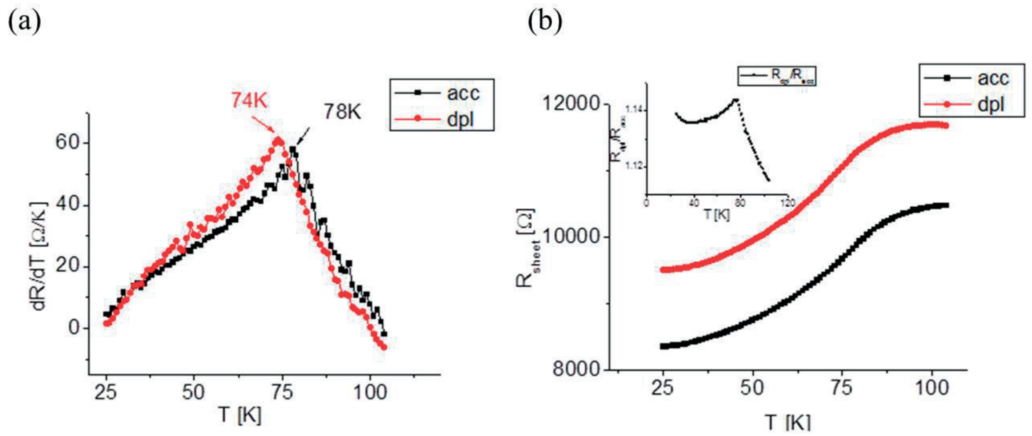

Figure 3.10: Magnetotransport measurement on (Ga,Mn)As/CYTOP/P(VDF-TrFE) sample. (a) T_C in accumulation (acc) and depletion (dpl) can be estimated from the tip of dR/dT plots. (b) R_{sheet} vs. T curves in accumulation (acc) and depletion (dpl) states. Inset: the gating efficiency (ratio of resistance with opposite polarizations) reached 14%.

Figure 3.10 displays the results of the magnetotransport measurements on (Ga,Mn)As/CYTOP/P(VDF-TrFE) heterostructures. Here we use the dR/dT singularity for estimation of T_C.[209] T_C was shifted by 4K (74K vs. 78K), and the gating effect (the difference of R_{sheet}) with polarization reversal reaches 14% near the phase transition temperature. As a reference, the results from conventional Hall bars demonstrated 3.8K T_C shift and 9% gating effect in the (Ga,Mn)As/P(VDF-TrFE) sandwich.[191] Even though the T_C shift stayed nearly the same, the gating effect on sheet resistance almost doubled; hence we could conclude that the interface was improved by CYTOP layer integration.

3.9.2 Mixture of P(VDF-TrFE) and PMMA as a new gate material

An alternative route of gate modification aimed at boosting the intrinsic resistance of P(VDF-TrFE) was the use of P(VDF-TrFE)/PMMA blend. With a higher resistivity, the internal leakage of the ferroelectric gate will be suppressed, resulting in a better retention performance.

In a perfect poled ferroelectric gate, the positive and negative charge should stay on the opposite surface permanently. In reality the finite resistivity of the ferroelectric material allows some amount of leakage charge driven by depolarization field, resulting in charge screening with time. Therefore with a higher resistance of the material a better retention performance of the gate is expected.

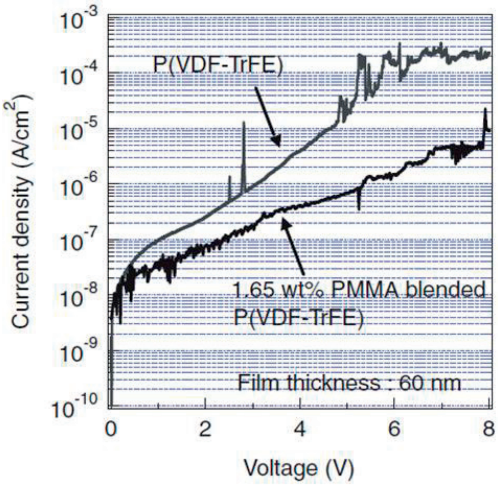

Figure 3.11: Leakage current-voltage curves of a Pt/1.65wt% PMMA-blended P(VDF-TrFE)/Pt multilayer and a Pt/P(VDF-TrFE)/Pt multilayer. Polymer layers are 60 nm thick.[210]

The mixture of P(VDF-TrFE) and PMMA [poly(methyl methacrylate)] could improve the ferroelectric gate, because the PMMA has a very high volume resistivity of over $10^{18}\Omega$/cm. After mixing with PMMA, the current through the ferroelectric layer can be decreased by almost two orders of magnitude (Figure 3.11) relative to that of single component P(VDF-TrFE).[210] At the same time, the polymer mixture still retains good ferroelectric properties, as the hysteresis loop of 200nm 10 wt% PMMA blended P(VDF-TrFE) thin film in Figure 3.12(a) shows. The remnant polarization shows a positive result from magnetotransport measurements in (Ga,Mn)As: T_C shift is about 6K and gating effect reaches 25% max, comparing to the previous results of 3.8K T_C shift and 9% gating effect. Thus the T_C shift value got a 50% increase while the gating effect tripled.

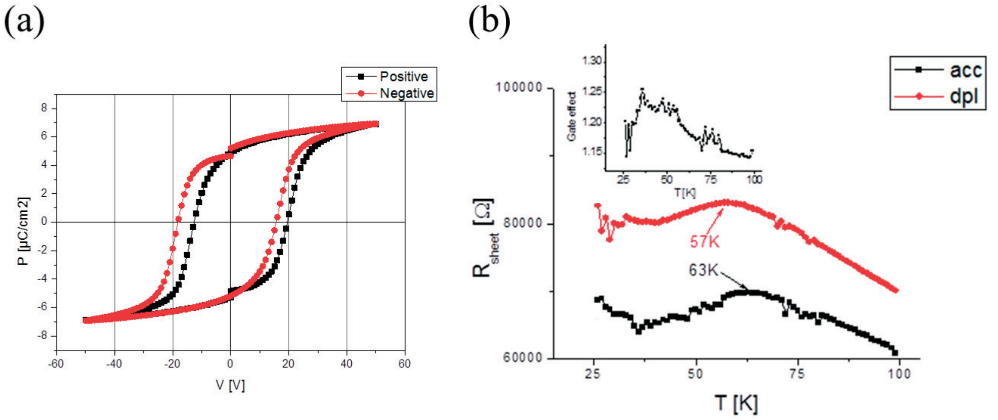

Figure 3.12: (a) Polarization hysteresis loops of 200nm P(VDF-TrFE)$_{0.9}$/PMMA$_{0.1}$ ferroelectric layer, sweeping electric field from opposite orientation. (b) R_{sheet} vs. T curves in accumulation (acc) and depletion (dpl) states. Inset: the gating efficiency (ratio of resistance with opposite polarizations) can reaches 25%.

In summary, two approaches for ferroelectric gate performance optimization were explored. With hydrophobic CYTOP layer inserted, the heterostructure showed higher gating effect than before indicating that the interface was improved. This effect blocked the gate performance deterioration due to the extra dielectric layer leading to overall gating improvement. The approach using the polymer mixture presented an enhancement of both resistance ratio under gating and T_C shifting, meaning a successful optimization.

3.10 The fabrication of μm/nm wide magnetic channels

For precise measurements of magnetic domain wall speed in presence of ferroelectric field effect, the magnetic media needs to be patterned as an array of channels. A convenient solution for V_{DW} measurement is to prepare magnetic domains in a relatively large “reservoir” and inject them in a narrow channel where 1D domain growth can be investigated.

For the fabrication of high-quality channels narrower than 1μm, we investigated the use of electron beam (E-beam) lithography.

E-beam lithography system creates designed patterns on the electron-sensitive resists by using focused electron beams. The biggest advantage of E-beam is its ultra-high resolution. However because E-beam system has to create the patterns pixel by pixel sequentially, the exposure procedure takes more time on large area compared to the photolithography procedure.

The resist thickness and substrate type influence the exposure result significantly. When electrons enter into the resist layer, the transverse scattering is inevitable, thus exposing the adjacent resist. The thicker the resist is, the larger is the area exposed due to transverse scattering, and the lower is the obtained resolution. The backscattered electrons from the substrate contribute to the exposure as well. As the simulation shows in Figure 3.13, 10kV beams have 1µm back-scattering range and 20kV beam results in 3µm back-scattering. These scattering issues must be taken into account when establishing process receipt.

All E-beam experiments presented here were accomplished by Vistec 100kV EBPG 5000 system in CMI (Center of Micro-Nanotechnology), EPFL.

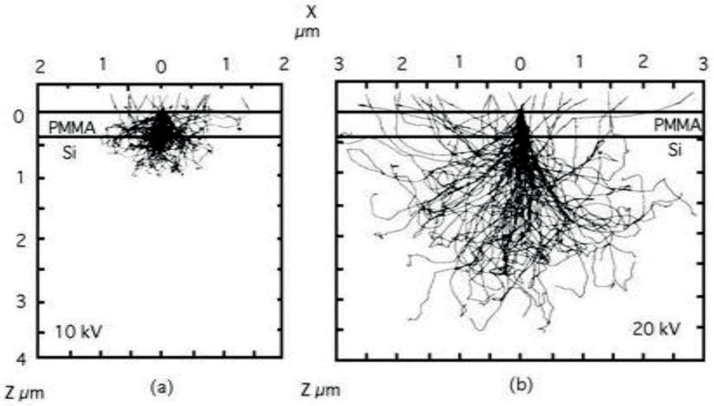

Figure 3.13: Monte-Carlo simulation of electron beams scattering on PMMA/Si sample. The higher energy beam has deeper penetration and broader back-scattering range.[211]

3.10.1 Resist selection and dose testing

Choosing suitable electron resist is an important part in E-beam lithography, which must take into account the sensitivity of both Co and P(VDF-TrFE). The final choice is a compromise of exposure resolution, thermal/chemical compatibility and process facility.

Four resists are provided at CMI: PMMA/MMA, ZEP, HSQ and nLOF. Their process conditions are listed in the following table:

Resist	Polarity	T_{baking} (˚C)	Resolution	Developer & Rinse	Remover
PMMA/ MMA	Positive	180	< 20nm	MiBK:IPA 1:3 & IPA	Acetone
ZEP	Positive	180	< 30nm	Amyl-Acetate & MiBK:IPA 90:10	Dry etching
HSQ	Negative	Room temperature	< 10nm	MF_CD_26 & DI water	BHF
nLOF	Negative	115	< 100nm	AZ726 MIF & DI water	Remover 1165

Table 3.1: The process conditions of all electron resists provided by CMI.

Normally PMMA/MMA is more suitable for lift-off while the other three work for wet or dry etching. As explained below, the lithography on the Co layer and the P(VDF-TRFE) film required different selection of resists.

Lithography receipt for nm-sized features preparation on Co layers

The need is to get 100nm feature size on the substrate. The stripes are made of sandwiches of the layers of Pt, Co and AlO_x placed on the 500nm SiO_2/Si substrate. Lift-off method with PMMA/MMA resist is chosen, avoiding the dry etching that risks to burn the ultra-thin Co layer or the wet etching solution that risks to corrode AlO_x. In addition, the 500nm insulating SiO_2 on the top of conductive Si is transparent to most of the 100keV electrons causing trapped charge issue.

The total thickness of Pt/Co/AlO_x layers is less than 10nm, so the height of resists should be as thin as possible for precise pattern projection. The thinnest receipt consists in deposition of 100nm MMA and 50nm PMMA on the substrate.

Scanning electron microscopy (SEM) was used to observe the nm-scale structures. Since the residual PMMA/MMA resist will melt and deform under electron beam exposure, the pattern fixation is necessary for precise characterization of lithography results in SEM. Thus before loading dose-test samples into SEM, 15nm Ti and 100nm Au were evaporated as the same as the “Metal deposition” step after *Photolithography I* in section 3.7 and followed by lift-off for fixing the exposed pattern on substrate (light grey patterns in Figure 3.14).

An array of polygons was exposed and the 50nm critical dimension was achieved as shown in the lower image of Figure 3.14. Through dose test, the right dose was determined for 100nm MMA/50nm PMMA on 500nm SiO_2/Si, and the 50nm resolution exposure was obtained. Hence, the narrow channels can be fabricated nicely with the various widths. In Figure 3.15, 200nm and 500nm wide channels are shown with precise edges that would be hardly imagined without E-beam lithography.

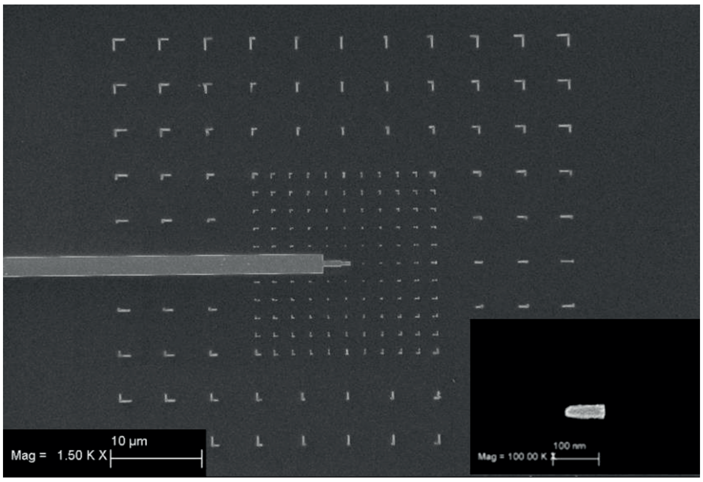

Figure 3.14: SEM images of test samples with location markers design. Upper: the whole array spreads in 50×50µm region. Inset: the smallest marker in the array, with critical dimension of 50nm.

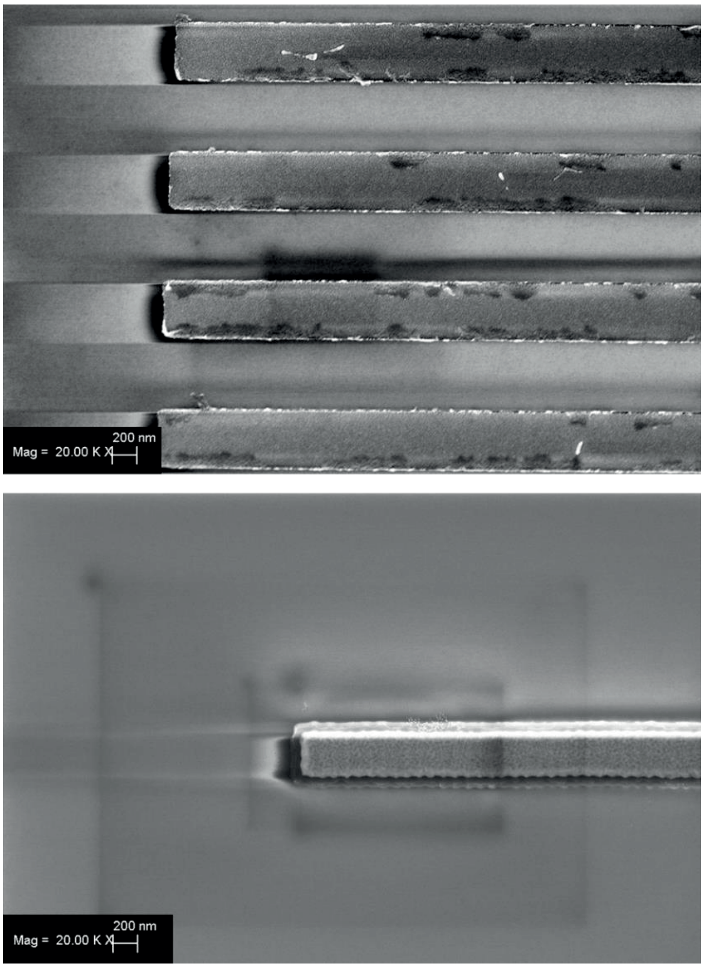

Figure 3.15: SEM images of 500nm (up) and 200nm (down) wide metal channels fabricated by E-beam lithography technique.

E-beam preparation of gate electrodes on the ferroelectric polymer

The lithography for gate electrode on P(VDF-TrFE) is totally different from that of the metals described above. P(VDF-TrFE) ferroelectric crystalline layer cannot survive above 180˚C baking, excluding the possibility of PMMA/MMA and ZEP. The use of nLOF is not possible due to its remover 1165, an organic solvent that could attack P(VDF-TrFE) when cleaning the remnant resist. Thus HSQ is the chosen resist for lithography above the ferroelectric copolymer, with no-baking procedure and the HF as resist remover safe to P(VDF-TrFE).

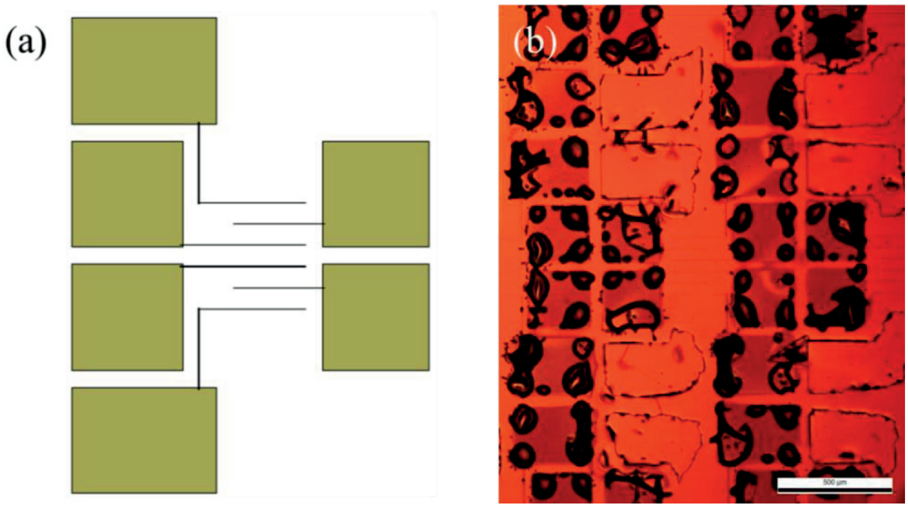

Figure 3.16: (a) Software design of gate electrodes, containing contacting pads (dark yellow) to external instrument, and 500nm wide channels (black lines) crossing the underneath Co channels. (b) Optical microscopy image after resist developing, showing huge bubbles at contact pad position.

Once all the steps described above successfully done, the residual gold on the P(VDF-TrFE) would form the gate electrode following the design pattern, as Figure 3.16(a) shows. The electrode lines from the contacting pads would be 500nm wide and would go across the Co channels. The P(VDF-TrFE) between the top gate lines and bottom metallic film would be polarized for probing the field effect locally.

Unfortunately, the P(VDF-TrFE) layer deteriorated under the 100keV electron beam exposure. Figure 3.16(b) clearly shows the bubbles appearing where the regions were exposed. After wet etching and HSQ removal, the bubble structures could still be observed implying that the bubbles are below the Au pads at the P(VDF-TrFE). Indeed the *P-E* hysteresis loop showed strong leakage in the P(VDF-TrFE) gate and the ferroelectricity in the copolymer was destroyed.

This lead us finally to use alternative poling techniques on P(VDF-TrFE), such as AFM poling, rather than E-beam fabricated narrow electrodes.

3.10.2 Hall measurements to evidence ferromagnetism in narrow channels

There are numerous experiments in the literature demonstrating a much lower ferromagnetic T_C in Co thin films compared to bulk Co.[148] Therefore it was important to verify whether the width reduction of the Co channel affected the ferromagnetism. A series of Co channels, of widths varying from 10μm to 200nm, were prepared to study this.

We measured the accumulated anomalous Hall effect from a compact array instead of measuring single channels in order to overcome the noise problem. To make the results comparable between the different channel widths, the Co arrays were made so that the total width of the channels stayed the same, with five 10μm channels, twenty-five 2μm channels, one hundred 500nm channels or 250 200nm channels. All the arrays are carefully chosen to have the same AlO_x wedge thickness therefore the same intrinsic magnetic properties.

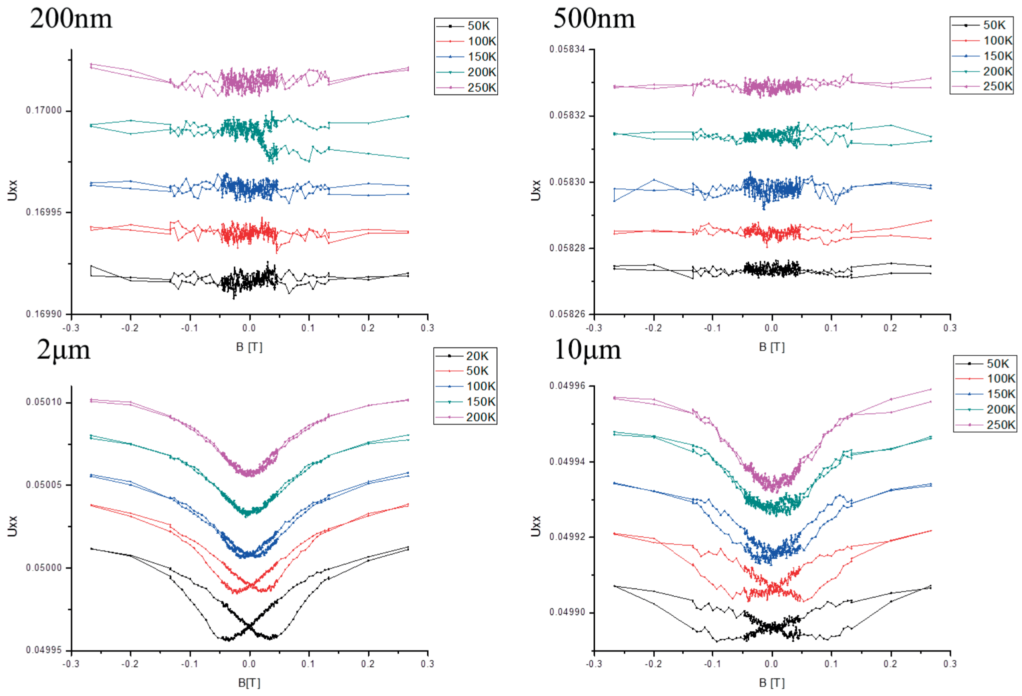

Figure 3.17: U_{xx} Hall voltage vs. field plots from 200nm, 500nm, 2μm and 10μm channel arrays. For the 200nm and 500nm wide channels, no hysteresis loop is observed, while butterfly-shape loops indicate ferromagnetism in 2μm and 10μm channels.

Figure 3.17 shows the Hall voltage vs. magnetic field at room temperature for four different arrays. The flat curves for 200nm and 500nm channels suggest the extinction of magnetic coupling between cobalt atoms while the butterfly-shape loops from 2µm and 10µm channels endorse their ferromagnetism.

The fading of ferromagnetism in the sub micrometer channels could be a result of lateral damage or uncontrolled oxidation from the bare edges of the narrow in 200nm and 500nm channels.

Thus E-beam fabrication of structures with 50nm resolution was possible; however the direct E-beam writing on the polymer film caused ferroelectricity degradation, hindering the preparation of the sub micrometer gate electrodes. Based on the results of magnetotransport characterization, the Co channels show a degradation of ferromagnetism with width decrease. Therefore the choice of the magnetic channel width for DW velocity experiments implies a tradeoff between 1D confinement of domain wall and reasonable ferromagnetism strength. Thus 10µm wide Co channels were chosen for the experiments in Chapter 6.

3.11 Summary

In conclusion, this chapter presents the experimental techniques used in this thesis and processing routines for experimental structure fabrication. The core experiments carried out in this work required fabrication of Hall bar devices with (Ga,Mn)As and Co channels. A number of routes were undertaken in order to optimize the magnetoelectric coupling and enhance the gate effect. Two approaches enhancing the gate involved either CYTOP layer integration or use of P(VDF-TrFE)/PMMA blend. Both modifications improved FeFET device operation. The E-beam technique was optimized to scale the magnetic channels down to 200nm; however this approach was not viable due to the severe degradation of ferromagnetism at room temperature. Therefore the micron-size Co channels were found to be optimal for exploring domain propagation in presence of non-volatile gate effect.

Chapter 4
Ferroelectric control on AMR symmetry in (Ga,Mn)(As,P) thin film

Recent studies of multiferroic heterostructures[191,212] demonstrated a clear effect of non-volatile change of the magnetic state driven by reversal of the spontaneous polarization of the ferroelectric gate. However, the ferromagnetic Curie temperature (T_C) shift associated with the polarization reversal is rather small, in agreement with the theoretical predictions of T_C dependence of the charge concentration.[142] On the other hand, the real physical picture of the magnetic response to the polarization reversal can be more complex. In particular it may involve magnetic anisotropy change including a change in the direction of the easy magnetization axis and other qualitative changes of the ferromagnetic system.

In this chapter anisotropic magnetoresistance (AMR) is used as a probe to detect profound changes of the magnetic state driven by the ferroelectric gate. Even though the quantitative theory describing AMR in those studied ultrathin DMS layers is not available, some very important conclusions about the magnetic state change can be made from phenomenological analysis of the AMR behavior. In particular this study demonstrates a strong qualitative change of sign and symmetry of AMR signal induced by ferroelectric gating in DMS channels. The experimental study of AMR presented in this chapter is a result of teamwork involving contributions of Evgeny Mikheev (Master project of 2011 done at LC under supervision of I. Stolichnov and N. Setter) and Z. Huang, the author of this PhD thesis. Specifically E. Mikheev has made major contribution to development of AMR setup, made initial steps in exploring transport properties of DMS and transferred his knowledge to Z. Huang who continued this work. The AMR study on DMS has been carried out jointly by E. Mikheev and Z. Huang and the major results were summarized in the *Applied Physics Letters* paper authored by both[213].

4.1 Magnetoresistance characterization in co-doped (Ga,Mn)(As,P) thin film

At the initial stage of experimental investigation on field effect control of magnetism in DMSs the focus was on (Ga,Mn)As, which is arguably the best established DMS material with well understood physics of magnetoelectric coupling.[214] Recently the introduced (Ga,Mn)(As,P) composition offered a new degree of freedom in tuning the ferromagnetic properties: magnetic anisotropy control through the lattice mismatch, as described in Chapter 3. Additionally these materials allow for optimization of change carrier concentration via annealing, which makes them strong candidates for ferroelectric control of ferromagnetism. For exploring these effects it is of particular interest to combine the monitoring of T_C with AMR measurements which are sensitive to delicate changes of magnetic anisotropy. This approach enables the sensing of delicate variations of the magnetic state that cannot be detected by simple Arrott plots or R_{xx} vs. T measurements.

In this series of experiments, thin films of two compositions: $(Ga_{0.94}Mn_{0.06})As$ and $(Ga_{0.94}Mn_{0.06})(As_{0.9}P_{0.1})$ were prepared by epitaxial growth by our co-workers at the University of Nottingham. For both compositions the thickness of magnetic layer was 7nm. The details of MBE growth of these magnetic layers are presented in Ref. 154. The Hall bar patterns were fabricated along the [1-10] crystalline direction, following the process described in section 3.7. Then a 300nm thick P(VDF-TrFE) layer used as ferroelectric gate was spin-coated and annealed. A top gate Au electrode was then deposited by thermal evaporation. The gate tests delivered systematically high quality sharp polarization hysteresis loops with remnant polarization of 8-9μC/cm^2 and coercive field of 550-650kV/cm.

Before analyzing AMR in gated (Ga,Mn)(As,P), the temperature dependence of the resistivity was investigated in order to clarify the conduction mechanism and estimate the ferromagnetic T_C. The four-probe resistance data for both compositions are summarized in Figure 4.1. Generally the composition containing phosphorus showed a pronounced insulating behavior and a strong resistive switching, with the ratio of depletion to accumulation state resistances, R_{dpl}/R_{acc} reaching 10 at very low temperatures (Figure 4.1(a)). Because of the insulating behavior of the layer, measurements below 15K were impossible for the depletion state. In the accumulation state, ferromagnetism below 31K was revealed using the well-established technique based on the cusp of sheet resistance derivative dR_{sheet}/dT (Figure 4.1(d)). This cusp was suppressed in depletion due to low conductivity, but a 3-4K downward shift of the ferromagnetic transition temperature T_C could be confirmed via Arrott plots and ferromagnetic switching signatures (Chapter 3).

For both compositions, the conductivity is characterized by thermally-activated behavior:

$$R_{sheet}^{-1} \propto exp(\frac{\Delta E}{k_B T}) \tag{4.1}$$

where ΔE is the activating energy barrier and k_B the Boltzmann constant.

This conduction behavior was confirmed by linear current-temperature dependence plotted in Arrhenius coordinates (log. R_{sheet}^{-1} against $1/T$) for accumulation and depletion states (Figure 4.1(b)). Such conduction regime is attributed to hopping conduction in $(Ga_{0.94}Mn_{0.06})(As_{0.9}P_{0.1})$, with ΔE corresponding to the energy for hole excitation between the localized Mn_{Ga} impurity level and the valence band.[215]

The activation energies extracted from both materials in accumulation and depletion states are shown in Figure 4.1(c). The phosphide-doped composition revealed a much higher activation energy compared to the classic (Ga,Mn)As composition. This observation is in agreement with earlier reports[214] showing that P-doping provokes a gradual metal-to-insulator transition associated with movement of impurity Mn-levels deeper into the band gap. The data in Figure 4.1(c) suggest that the activation energy in (Ga,Mn)(As,P) is remarkably sensitive to the polarization state of the gate, implying that the degree of hole localization can be tuned by the ferroelectric gate. The fact that the magnetic properties of the system are strongly sensitive to the degree of localization suggests that (Ga,Mn)(As,P) is a highly attractive system for probing ferroelectric control of magnetic anisotropy.

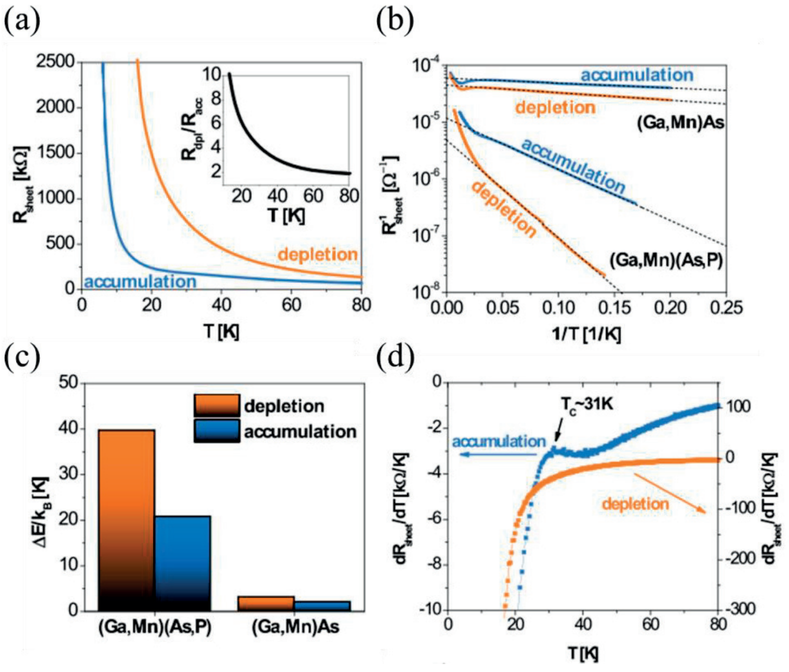

Figure 4.1: Electrical transport characteristics in the (Ga,Mn)(As,P) layer, in accumulation and depletion states of the ferroelectric poling. (a) Temperature dependence of R_{sheet} and the gating efficiency (inset). (b) Illustration of thermal activation behavior and comparison to a reference device without phosphorus co-doping. (c) Extracted activation energies for the two ferroelectric gate states in both devices. (d) Temperature derivatives of R_{sheet} in (Ga,Mn)(As,P) layer.[213]

4.2 AMR_{IP} in (Ga,Mn)(As,P) thin films under ferroelectric gating

AMR measurement is one of the central experiments carried out in this thesis work in order to understand the nature of response of the magnetic media to the electric field induced by the ferroelectric gate. The focus of this experiment is identifications of the qualitative changes such as reversed sign or altered symmetry of AMR signal and their interpretations in terms of the magnetic state change.

The most striking manifestation of gate effect on AMR occurs when the magnetic field is rotated in the sample plane. Therefore AMR_{IP} was probed by monitoring the longitudinal and transverse electrical resistances R_{xx} and R_{xy}, while rotating a magnetic field of constant magnitude in the plane parallel to the sample surface as illustrated by Figure 4.2(b). The angle between B and the [110] crystalline direction is denoted ψ, in accordance with the notation in Chapter 3. The field magnitude B=0.5T was found to be sufficient to saturate the magnetization and align its orientation along the magnetic field (in the plane, IP) even for the DMS film that had an out-of-plane (OOP) easy axis. The temperature range was between 15K (lowest T for which magneto-resistance was measurable) and 35K (slightly above T_C). The results of the AMR_{IP} measurements are shown in Figure 4.2(a), containing the whole data array collected at different temperatures, for both accumulation and depletion states.

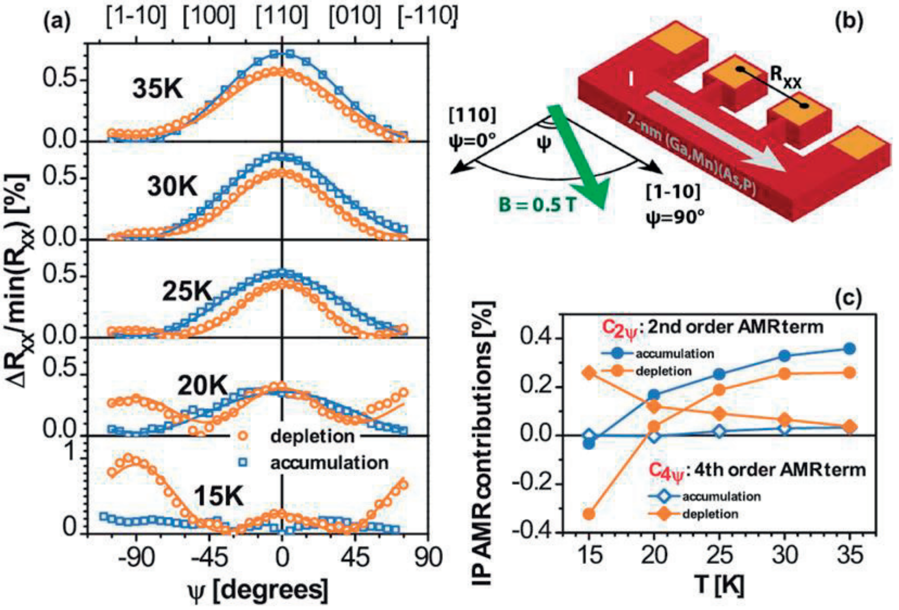

Figure 4.2: (a) Ferroelectric switching of AMR_{IP} under 0.5T magnetic field, swept 180° in the sample plane, as illustrated in (b). (c) Temperature dependence of the 2nd and 4th order terms ($C_{2\psi}$ and $C_{4\psi}$) of the AMR_{IP}.[213]

As expressed in equation (3.9), the angular dependence of R_{xx} on ψ can be described by:[169]

$$\frac{\Delta\rho_{xx}(\phi,\psi)}{avg(\rho_{xx})} = \left(C_U - C_I - C_{I,C}\right) cos(2\psi) + C_C\, cos(4\psi) \qquad (4.2)$$

where C_U and C_C are the uniaxial cubic and crystalline components, C_I the non-crystalline contribution, and $C_{I,C}$ the mixed crystalline/non-crystalline contribution. Therefore the angular dependence AMR can be represented as follows:

$$\frac{\Delta R_{xx}(\psi)}{min(R_{xx})} = \frac{R_{xx}(\psi) - min(R_{xx})}{min(R_{xx})} = C_{2\psi}\, cos\, 2\psi\; + C_{4\psi}\, cos\, 4\psi \qquad (4.3)$$

where $C_{2\psi}=C_U$-C_I-$C_{I,C}$ and $C_{4\psi}$ represents the purely crystalline cubic component.

The parameters $C_{2\psi}$ and $C_{4\psi}$ are treated as the experimentally observed contributions to longitudinal AMR from terms of 2nd and 4th order in ψ. They were extracted via fitting equation (4.3) from the experimental data as shown in Figure 4.2(a). The temperature dependence of AMR_{IP} exhibits striking differences between the accumulation and depletion states. Specifically, the gate effect induces very pronounced changes in the AMR shape. This is clear from Figure 4.2(c), where the values of $C_{2\psi}$ and $C_{4\psi}$ are plotted versus temperature. Poling the ferroelectric gate modulates the 2nd order component and deterministically switches the 4th order one *on* and *off*. This leads to a particularly remarkable situation at T=20K, where the near perfect 2-fold AMR symmetry in accumulation is broken in depletion, where the $C_{4\psi}$ component dominates. Equally noteworthy is the gated suppression of AMR at T=15K, where in accumulation AMR is not distinguishable above the thermal noise, while in depletion it reaches a large 1% amplitude.

The origin of the heavily modulated 4th order component lies in the crystalline AMR, to be distinguished from the non-crystalline AMR, which dominates in bulk (Ga,Mn)As as discussed above. The crystalline components of the AMR arise from modulations of the shape of the Fermi surface and the interplay with *k*-dependent scattering times as the magnetization is rotated in strongly spin-orbit coupled systems. The strong crystalline contribution to AMR observed in this experiments agrees with the earlier studies of ultra-thin (<10nm) (Ga,Mn)As films where the crystalline contribution to AMR was modulated by external stress[154]. The present experiment shows that it can be controlled electrostatically via field effect by reversing ferroelectric polarization of the gate.

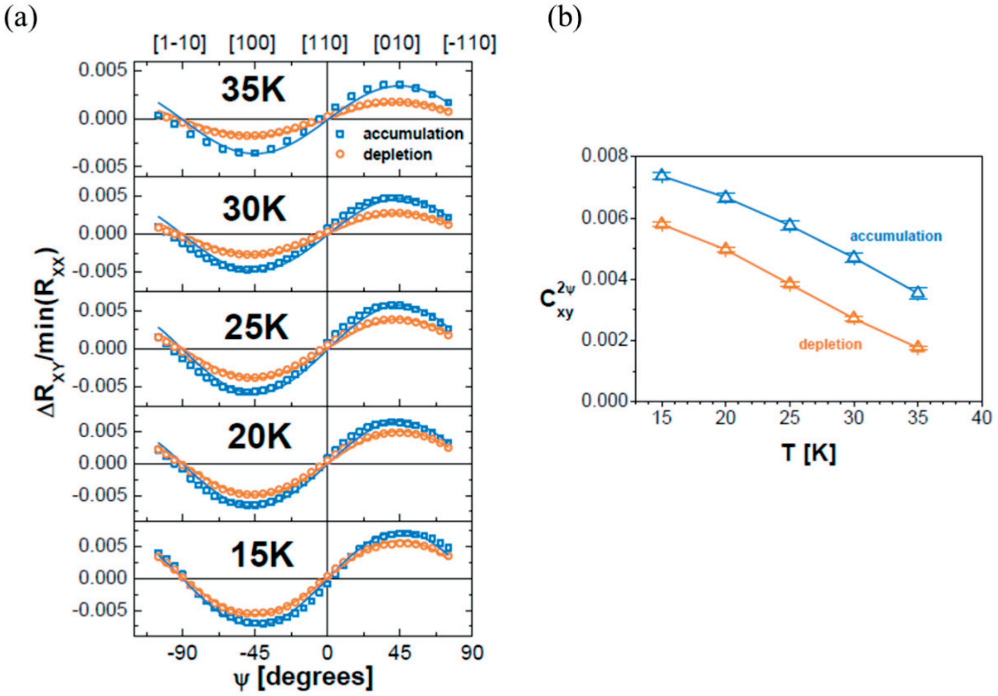

Figure 4.3: Transverse AMR with B=0.5T rotated in the channel plane. (a) The experimental data (open symbols) and fits using equation (4.4) (solid curves). (b) The 2nd order coefficient $C^{t}_{2\psi}$ extracted from the fitting.

Compared to the R_{xx} data discussed above, the component R_{xy} demonstrates a less striking AMR behavior; however it clearly reflects the ferroelectric gate effect with $C_{2\psi}$ magnitude modulation dependent on the poled state. The $C^{t}_{2\psi}$ for transverse AMR describes the dependence of R_{xy} on ψ as follows (equation (3.10)):

$$\frac{\Delta R_{xy}(\psi)}{min(R_{xx})} = \frac{R_{xy}(\psi) - avg(R_{xy})}{min(R_{xx})} = C^{t}_{2\psi}\, sin\, 2\psi \tag{4.4}$$

$$C^{t}_{2\psi} = -\,C_{I} + C_{I,C} \tag{4.5}$$

where *avg* stands for the average value of R_{xy} over a full rotation of B (extracted as the middle point between the two maxima). The experimental results for $C^{t}_{2\psi}$ are shown in Figure 4.3. As expected, $C^{t}_{2\psi}$ tends to increase with decreasing temperature and the gate effect is most pronounced around 35K (close to T_C) where a 2-fold modulation of $C^{t}_{2\psi}$ is observed.

4.3 AMR_{OOP} in (Ga,Mn)(As,P) thin film under ferroelectric gating

Further to showing the effect of ferroelectric gate on AMR_{IP} component we explored the behavior of AMR_{OOP} that represents the resistance variation for the magnetization change between the IP and OOP directions aligned by the strong magnetic field B. As shown in Figure 4.4(b), the magnetic field B sweeps between [1-10] and [001] orientations, and the current I flows along [1-10] direction. The direction of B is described by the angle θ between B and I vectors.

The conditions of AMR_{OOP} measurements are almost identical to the previous one: the constant field B=0.5T was rotating at different angles; the temperature range was between 15K and 30K. As in the AMR_{IP} study, the measurements for each temperature were carried out for two alternative polarization states of the gate. The AMR_{IP} results for the entire temperature range are shown in Figure 4.4(a).

For the data analysis, the longitudinal AMR_{OOP} was fitted to the following expression:

$$\frac{\Delta R_{xx}(\theta)}{min(R_{xx})} = \frac{R_{xx}(\theta)-min(R_{xx})}{min(R_{xx})} = C_{2\theta}\cos 2\theta + C_{4\theta}\cos 4\theta \qquad (4.6)$$

The extracted coefficients $C_{2\theta}$ and $C_{4\theta}$ are plotted in Figure 4.4(c). Obviously, $C_{4\theta}$ is very small and might originate from thermal noise rather than the true AMR contribution. Consequently AMR_{OOP} can be described in a relatively simple way using only one coefficient, which is 2nd order term $C_{2\theta}$.

The plots in Figure 4.4(c) clearly indicate that AMR_{OOP} is positive in the (Ga,Mn)(As,P) sample. Its magnitude reaches 3%. Furthermore the ferroelectric field effect results in a significant non-volatile change of AMR modulating its magnitude by a factor of 2-3.

The positive sign of $C_{2\theta}$ or AMR_{OOP} is likely to be a consequence of the tensile strain in the (Ga,Mn)(As,P) thin film MBE-grown on the Ga(As,P) buffer layer[154,156]. As discussed before, the sign for AMR_{OOP} reverses from negative to positive when strain is changed from compressive to tensile, which was predicted by theory[168] and observed experimentally on tensile-strained (Ga,Mn)As on (In,Ga)As buffer layers[216]. Therefore, this result of positive AMR_{OOP} is expected, even though positive AMR in (Ga,Mn)(As,P) has not yet been presented in earlier studies.

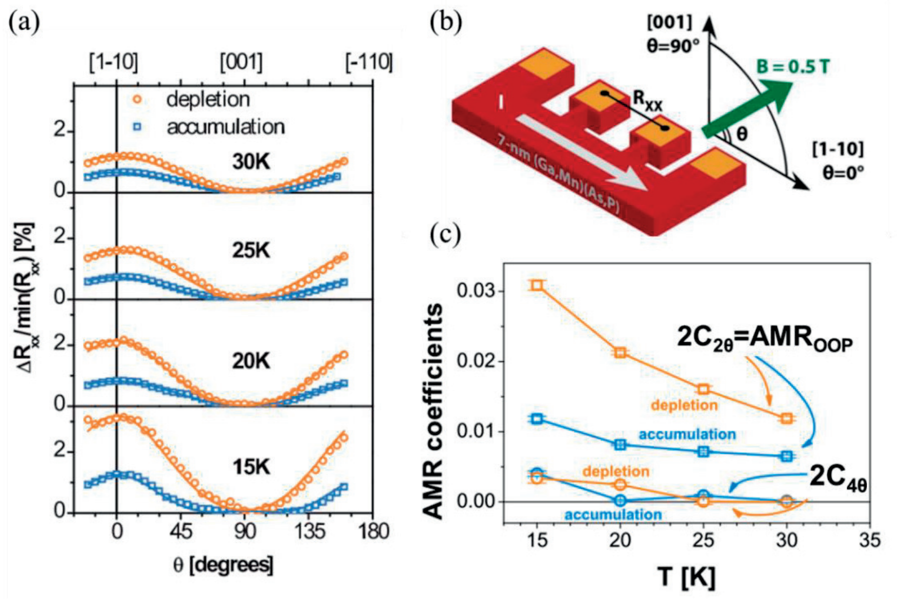

Figure 4.4: Longitudinal AMR with B=0.5T rotated between OOP and IP directions. (a) The experimental data (open symbols) and numerical fits using equation (4.6) (solid curves); (b) the geometrical arrangement used for the measurements.[213] (c) The extracted 2nd and 4th order coefficients $C_{2\theta}$ and $C_{4\theta}$.

As for the field-effect-induced change of AMR_{OOP}, this magnitude is remarkably high, reaching 3% at low temperature in depletion state, and suppressed to 1% by purely electrical control in accumulation. This is in contrast to the field-effect manipulation of less than 1% for AMR, reported in (Ga,Mn)As[166,217].

Apart from the characterization with fixed field strength, we gathered more information of AMR phenomena by applying magnetic field cycle. The typical R_{xx} dependences on B swept along [001] (OOP direction) and [110] (IP, along current) are illustrated in Figure 4.5(a); and the extracted AMR_{OOP} coefficient shows the variation with the magnitude of B in Figure 4.5(b).

The non-saturating behavior of AMR_{OOP} can be observed clearly from the diagram in Figure 4.5(c) and (d): along any horizontal line corresponding to a fixed temperature, the color continuously changes with the magnitude of B increasing. Another consistent trend in Figure 4.5(c) and (d) is higher AMR_{OOP} in the depletion state compared to the accumulation one.

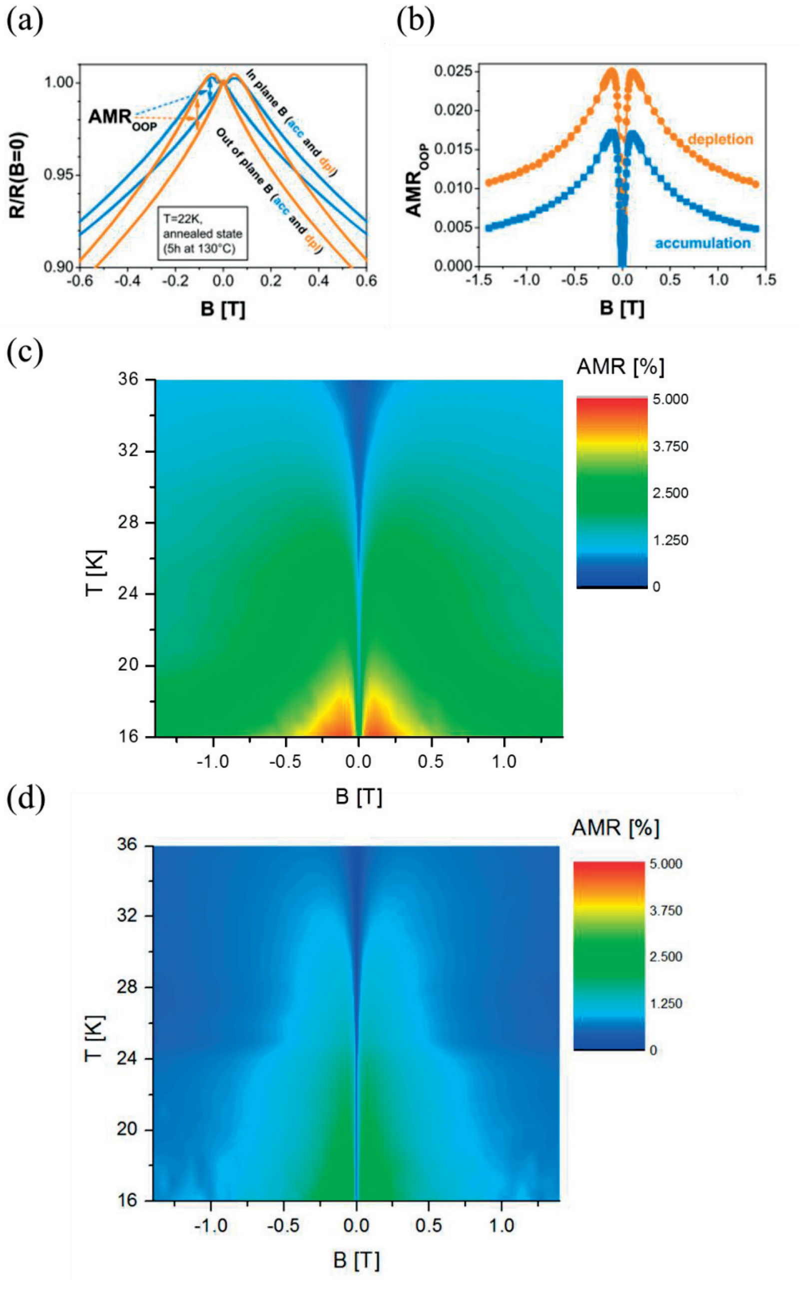

Figure 4.5: (a) Illustration of the extraction of $AMR_{OOP}(B)=(R_{xx}|_{B||[1\text{-}10]}-R_{xx}|_{B||[001]})/R_{xx}|_{B||[001]}$ from two B sweeps along [1-10] and [001]. (b) Representative extracted curve for AMR_{OOP} vs. B. AMR_{OOP} profiles depending on magnetic field, temperatures in depletion state (c) and accumulation state (d). The color scheme representing the AMR_{OOP} strength is shown on the sidebars.

The origin of the non-saturation behavior of magnetoresistance remains unclear. Obviously the maximum field of 1.4T used in this study was largely sufficient to fully align magnetization along both IP and OOP directions regardless the natural easy-axis orientation of anisotropy. Additionally the coercive fields extracted from AHE data for

(Ga,Mn)(As,P) films always never exceeded 0.1T. Thus the AMR_{OOP} variations at high field are unlikely to be related to non-saturated magnetization. Earlier the observation of the non-saturation behavior of the longitudinal magnetoresistance R_{xx} in (Ga,Mn)As was attributed to the suppression of spin disorder in metallic samples and the carrier localization in insulating regime.[216, 218 , 219] In our case, the (Ga,Mn)(As,P) film is highly insulating. Since AMR_{OOP} is defined as the difference between magnetoresistance with magnetic field along OOP and IP directions, it is likely that the non-saturating behavior originates from the anisotropic carrier delocalization behavior at high B. In other words, R_{xx} does not depend in the same way on high B applied along IP and OOP orientations.

4.4 The relation between AMR_{OOP} and R_{sheet}

In view of the possible role of carriers delocalization in the observed AMR features, it is of interest to explore the relation between AMR and sheet resistance in gated (Ga,Mn)(As,P). For this material the resistance can be conveniently tuned by annealing so that a full set of measurements for different resistance values can be performed using the same device. After annealing the device at T=130˚C for 1 and 5 hours (safe temperature for copolymer gate), R_{sheet} and AMR_{OOP} characterization were carried out following the same measuring procedure as before.

Figure 4.6 represents the ensemble of the data for AMR_{OOP} at B=0.5T. The AMR data are plotted against the value of R_{sheet} when B=0. The six plots show that there is a clear relation between the magnitude of AMR_{OOP} and R_{sheet}. For each annealing state, there is a universal curve behavior between the two polarization states, linear in a double-logarithmic scale.

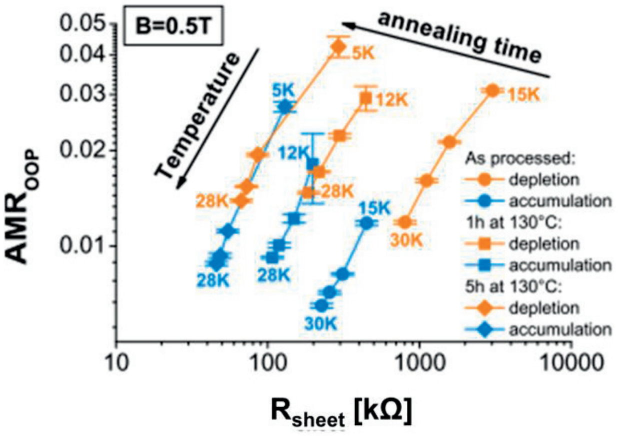

Figure 4.6: Ensemble of the data for AMR_{OOP} at B=0.5T. Each plot corresponds to one state of gate polarization and annealing; each data point represents a value at given temperature.

Within each plot, the relation between AMR_{OOP} and R_{sheet} can be written as:

$$AMR_{OOP} = CR_{sheet}^{\eta} \tag{4.7}$$

where C is a fitting constant and η is the governing exponent. Fitting to the plots in Figure 4.6, the results for the annealing processed devices in the same poling state are very close: approximately η=1 for accumulation and η=0.75 for depletion.

This regularity of η persists over a very wide range of R_{sheet} (almost two orders of magnitude) and thus of localization and effective concentration of holes, exaggerated by annealing process. This suggests that the origin of the gated tuning of η could be surface-related. If it were due to a modulation of "bulk" hole density, one would expect the perceived effect on η to quickly decrease with time, given the strong screening of electric field by carriers.

Consequently, it is very difficult to separate and extract the experimental parameters responsible for the sensitivity of AMR on field-effect gating. Phenomenologically, inducing 10% chemical modification of arsenide by phosphorus and changing interfacial strain from compressive to tensile results in a high sensitivity of AMR. AMR is known to be a strong function of strain from both theory and experiments.[216] Presence of P in place of As can change the band structure or the nature of exchange interactions between holes and Mn impurities.[167] All of these can contribute to change the asymmetry of scattering and thus on AMR.

4.5 Summary

AMR study carried out on ultra-thin DMS layers controlled by ferroelectric gate enabled an insight into very profound changes of the magnetic state which are associated with the persistent field effect.

For the (Ga,Mn)(As,P)/P(VDF-TrFE) multiferroic, the essential features included the possibility of non-volatile ferroelectric-gate-driven modulation/ suppression of the AMR signal. Additionally, it was demonstrated that the non-volatile field effect resulted in switching of the AMR symmetry with turning on/off the crystalline AMR component. In contrast to a relatively weak ferromagnetic T_C modulation, the AMR switching observed in this study has a deterministic character and implies strong changes of the magnetic anisotropy. From the device physics perspective, these results show a different mode of multiferroic device operation compared to the earlier reported ferroelectric control of ferromagnetic T_C.

Chapter 5

Ferroelectric control of ferromagnetism in ultra-thin Co film: insight through magnetotransport

Heterostructures for magnetoelectric coupling that are suitable for room temperature operation rely on electrical gating of magnetic metal channels. Their practical implementation is difficult because of the very high concentration of electrons even in thinnest metallic layers (1-2 monolayers). Additional complications originate from the very delicate character of ferromagnetism in such thin layers. Furthermore these layers do not easily lend themselves for integration of gate materials. In this context careful characterization of magnetic properties of the metal channels integrated in multiferroic structure is of made importance before any analysis of phenomena of magnetoelectric coupling can be. It is essential to assess first the magnetic properties of the channel in pristine devices (without any induced changes due to the by biased ferroelectric gate) and only then examine the modification of the magnetic properties due to the ferroelectric polarization switching.

This chapter presents first magnetotransport measurements of multiferroic heterostructures composed of Co magnetic channel and P(VDF-TrFE) gate. Since often magnetization measurements are problematic for devices of microscopic size with ultra-thin channels, magnetotransport is one of the most direct techniques to obtain the signatures of the magnetic state. This chapter presents magnetotransport data measured on FeFET structures with Co channel, demonstrating adequate characteristics of the magnetic channel and robust non-volatile magnetoelectric coupling at the room temperature.

5.1 Ferromagnetism in ultra-thin Co film and ferroelectric control on its magnetic hysteresis

In a heterostructure combining a thin metal layer and a gate (either conventional or ferroelectric) only a very weak electrical modulation of charge density is possible (generally less than 1%) because of too high electron density. However, even such a small relative modulation may impact significantly the magnetic properties. The reason is a delicate balance between different contributions to the magnetic anisotropy energy (MAE) that results in its high sensitivity to the changes of electronic structure at the interface.[189] Thus, a weak change of charge density induced by the electric field at the extremely narrow interface-adjacent layer is sufficient for a substantial change of T_C, coercivity, and other characteristics.

Cobalt in bulk form has a very high Curie temperature (1388K); however, as the thickness decreases to a few monolayers film, the magnetic interaction is significantly altered. As discussed in the previous section 2.2.2, a dramatic decrease of T_C in such films was observed: ~500K (2.5ML) and ~130K (1.5ML).[148] In contrast to the bulk, the interface and surface contributions to the magnetic properties in thin films are considerable.[151] For the study of the field effect control of magnetic properties in the ultra-thin Co film, it is necessary to clarify the temperature range where ferromagnetism exists in measured device structures.

In this experimental work, the existence of ferromagnetic phase was verified by examining the Hall resistance hysteresis behavior at 100K, 200K and 300K. Using the workflow described in section 3.8, the first Hall bar device was fabricated on 3nm Pt/0.6nm Co/~1.5nm Al wedge stack, without integrating any gate. The purpose of preparing this batch was to test the processing workflow on the ultra-thin sensitive metallic film; the goal of the measurements was to obtain some basic information on its properties including as T_C and coercive field, which may degrade during Hall bar fabrication. For magnetotransport tests, the sample with the electrically wired Hall bar was mounted on the cold finger of the closed-cycle Janis cryostat. The magnetic field was applied perpendicular to the magnetic film plane (Hall geometry), the Hall voltage was measured at magnetic fields changing within the range up to ±1.4T. The Hall bars chosen for the measurements were located in the part of the wedge with the out-of-plane easy magnetic axis as illustrated in Figure 3.8.

To verify that the channel is ferromagnetic, three Hall effect loops were measured from 100K to 300K. This enabled a conservative estimation of the T_C based on the information of Co thickness and the thickness-T_C diagram of Figure 2.7. In Figure 5.1, the R_{xy} hysteresis shows robust ferromagnetism at 100K. As the temperature increases, the remnant magnetization and the coercive field are decreasing. Remarkably AHE hysteresis is observed even at 300K confirming ferromagnetism at room temperature. However the weakness of the loop indicates a proximity of T_C where the ferromagnetic phase will disappear.

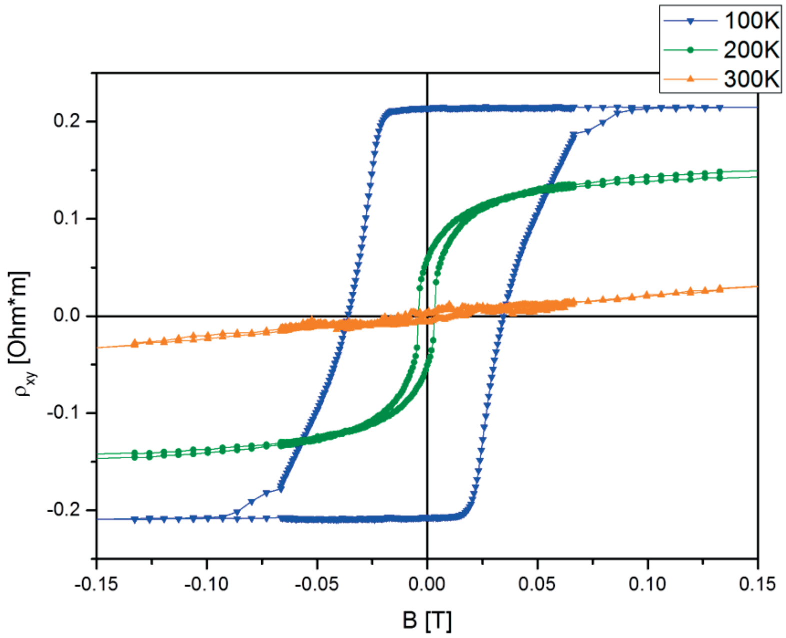

Figure 5.1: R_{xy} Hall resistance hysteresis loops on Co channel without gate covering. The measurements were performed at 100K, 200K and 300K.

Further to confirming ferromagnetism in the processed Co channel at 300K, the Hall bar devices were prepared with 200nm P(VDF-TrFE) gate covered with top Au electrodes. The ferroelectric field effect on the Hall resistance hysteresis was tested by recording the AHE hysteresis loops for the gate poled in different polarization states. The ferroelectric copolymer gate was subjected to "training" procedure with gradually increasing electric field and the polarization was fully reversed by applying ±20V/2s voltage pulse at room temperature. The data of Hall resistance R_{xy} measured after poling the ferroelectric gate are shown in Figure 5.2. The loops measured at 300K (Figure 5.2(d)) show a strong hysteresis behavior with coercive field about 5mT clearly indicating that T_C>300K in the gated Co layer. As expected, with the temperature decrease, the hysteresis loops demonstrate an increase of the coercive fields and the R_{xy} gap under the saturated magnetization, which is consistent with the ferromagnetic interaction strength enhancement illustrated in R_{Hall}-T plots in Figure 2.13(c).[179]

In Figure 5.2, for each temperature, the AHE hysteresis loops were measured for two opposite poled states of the ferroelectric gate. The black "0V" plots were recorded for the pristine gate before P(VDF-TrFE) was switched; the loops labeled "dpl" (red) correspond to the gate polarization pointing upwards (Co channel poled in the depletion state) ; the loops for the opposite polarization state, which correspond to the accumulation are labeled "acc" (blue). For each set of three loops "0V", "dpl" and "acc" there is an obvious trend of changing coercive field between depletion and accumulation states: the depleted Hall channel shows a lower coercive field compared to the accumulation state. This result agrees with expected higher magnetic anisotropy energy in the accumulation state as reported earlier.[179,183]

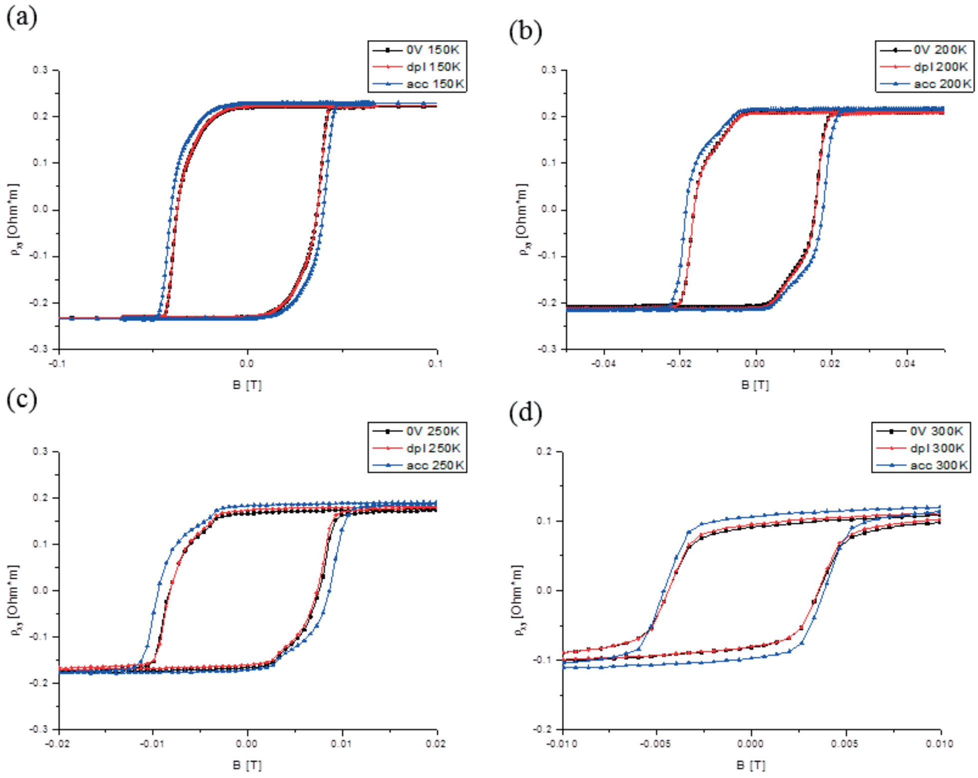

Figure 5.2: AHE measurements of R_{xy} in Co thin film taken at (a) 150K, (b) 200K, (c) 250K and (d) 300K. Within each panel, the "0V" black plot shows the data from the Hall bar with unpoled gate, the "dpl" and "acc" represent the depletion and accumulation states, respectively.[*]

Compared to the initial tests of the Hall bar without any gate (Figure 5.1) the AHE loops measured on the gated channel show a significant enhancement. This strengthening of ferromagnetism can be attributed to the slightly changed AlO_x thickness resulting in a stronger out-of-plane magnetic anisotropy.[†] The other remarkable feature in Figure 5.2 is a very small difference between the loops measured at "0V" and "dpl". A possible explanation of this effect is a polarization imprint of the as-deposited gate. Alternatively this effect can be attributed to the trapped charge that results in an additional non-ferroelectric built-in field. This trapped charge can significantly influence the ferroelectric gate performance and impact the reproducibility of the effect under repeated switching.

---

[*] The unsmooth magnetization reversing curves are considered as a manifestation of a multidomains switching pattern, discussed in page 114.

[†] With 5mm spacing between two Hall bars measured in Figure 5.1 and Figure 5.2, the estimation of AlO_x wedge thickness changing is about 0.5Å with the tangent of wedge angle 1Å/1cm.

To verify the reproducibility of the ferroelectric field effect, a series of AHE loops were taken after sequential reversal of the polarization in the gate. The polarization was switched at room temperature with ±30V/1s voltage pulses instead of the initially used ±20V pulses in order to create even stronger electrical stress and highlight the charge injection.

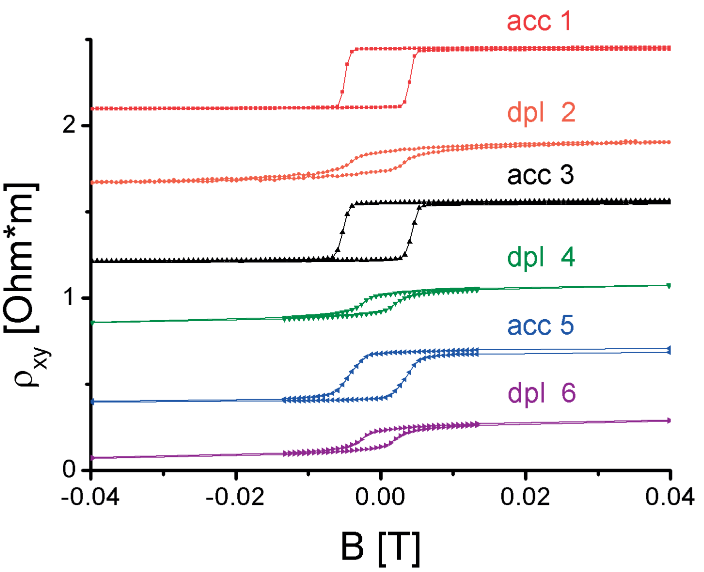

Figure 5.3: Sequential reversals of polarization in P(VDF-TrFE) gate inducing partial accumulation/depletion effects cause the Co layer to change its magnetic properties. The plots are shifted vertically for clarify.

Figure 5.3 shows the R_{xy} hysteresis loops in Co channel collected during this series of polarization reversals in P(VDF-TrFE) gate. The gate was initially poled in such a way as to induce the accumulation state, and then polarization was switched to the opposite state and *vice versa*, for six times in total. The reproducibility of the effect is confirmed by measuring the sequence of R_{xy} loops after each polarization reversal. Figure 5.3 clearly shows that every time the system is driven to the accumulation (depletion) state, the loop becomes wider (narrower), as expected.

On the other hand, a close examination of the sequential loops in Figure 5.3 shows some differences among the sequential accumulation/depletion poling states indicating that there is a slow evolution of the system during the gate polarization cycling. Specifically the “acc 5” loop is narrower and more tilted compared to the earlier loops “acc 1&3”. The most reasonable origin is the trapped charge in the dielectric AlO_x layer during the application of the voltage pulse. The strong field applied to the dielectric layer during polarization switching causes an injection of charge into the AlO_x layer. The charge is partially captured at deep traps, which results in a gradual formation of a charged layer. This layer influences both, field effect of the spontaneous polarization and switching ability of the gate ferroelectric.

In spite of some degradation of the ferroelectric gate performance that occurred under repeated switching, the phenomenon of ferroelectric control of ferromagnetism was found to be generally stable and reproducible. It was possible to systematically observe the ferroelectrically driven change of magnetic properties after tens of switchings. When exploring the impact of higher number of switching, one needs to take into account the polarization fatigue that reduces the available amount of switching charge. However, this problem is beyond the scope of the present study.

5.2 Magnetotransport signatures of switching magnetic domains in Co channel with ferroelectric gate

In addition to R_{xy} hysteresis, the longitudinal resistance R_{xx} carries also useful signatures of magnetic switching. A remarkable phenomenon observed from the R_{xx} plots as a function of magnetic field is the occurrence of antisymmetric spikes (Figure 5.4). Closer examination shows that the magnetic fields of the spikes are very close to the coercive field values extracted from the R_{xy} plots at the same temperature. Near room temperature, the two spikes get close to each other and finally collapse in a parallelogram-shaped loop. Such transformation is clearly seen in Figure 5.4(d) when the spikes are pushed together and merge for “0V” and “dpl” plots at 300K. At the same time, for the corresponding “acc” plot the two spikes remain well distinct indicating that the system is further from the phase transition, in agreement with the R_{xy} data (Figure 5.2).

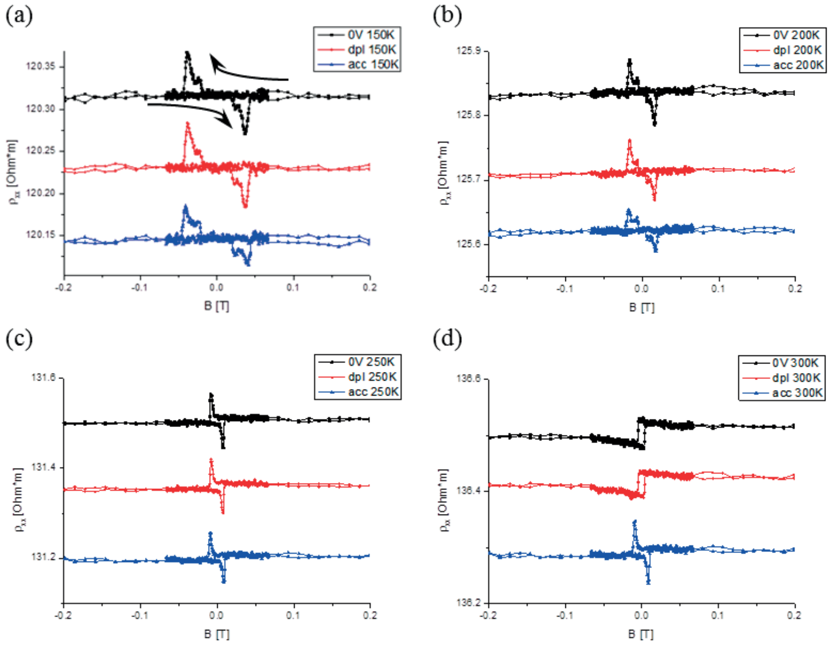

Figure 5.4: Magnetoresistance measurements on R_{xx} in cobalt Hall bar at (a) 150K, (b) 200K, (c) 250K and (d) 300K. The R_{xx} sheet resistance shows two antisymmetric spikes. The black arrows in (a) indicate the sequence of the data points collection.

The spikes of R_{xx} have been shown to be a signature of magnetic domains, which appear at the initial stage of magnetization switching during the external magnetic field sweep.[220,221,222] The origin of the spikes is linked to circulating components of the electrical currents passing through domain walls. These circulating components result in the admixture of AHE signal to the longitudinal resistance data R_{xx}. (Figure 5.5)

In the theoretical description of the R_{xx} spikes in Ref. 222, a single magnetic domain wall (DW) moving through the channel was considered. When the current is injected into a monodomain Hall bar channel, the current density vector ***j*** is uniform within the entire region. The DW presence in the channel causes deflection on the charge carrier movement as shown is Figure 5.5(a)-(c) illustrating the formation of eddy-like current distribution in the adjacent region of the DW. The ***j*** distributions due to a vertical DW and a 60° tilted DW are illustrated in Figure 5.5(d) and (e). Thus the presence of DW results in an admixture of R_{xy} to the longitudinal resistance, which is seen as the spikes in the plots of R_{xx}, when the current perturbation passes through the space between two electrodes. In practical experiments, several DWs moving in the channel at the same time represent a more likely scenario, which complicates the profile of the measured signal. In the spikes registered at 150K and 200K (Figure 5.4(a)&(b)), multiple peaks can be attributed to a complex multidomain switching pattern.

The magnitude of this domain-related resistance modulation is ~0.1Ω·m, i.e. about 0.1% of the background ρ_{xx} value (~120Ω·m), which is consistent with the data from the literature[223].

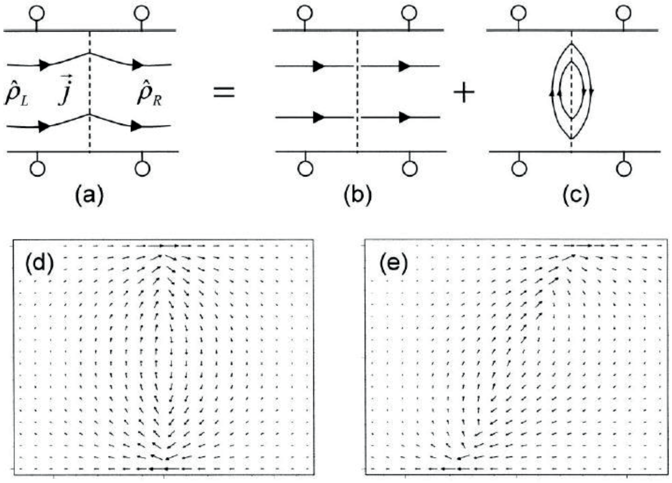

Figure 5.5: (a)-(c) Eddy-like non-uniform current distribution due to perturbation near the DW position. The current distribution can be decomposed as the sum of a uniform current (b) and a vortex-like circulation around DW (c). The simulation shows the vortex vectors near a vertical DW (d) and 60°tilted DW (e).[222]

The multidomain switching pattern can also be cross verified from the previous AHE measurements. Instead of a smooth magnetization reversing curve, the loops, in particular in Figure 5.4(b)&(c), demonstrate a fractured plots near the coercive field. The slope variation is interpreted as a manifestation of sequential reversal of several magnetic domains.

Regardless of the fine details of the switching process, the R_{xx} data confirm the trends earlier established from R_{xy} measurements. Specifically, R_{xx} measurements confirm ferromagnetism in the Co channel with polymer ferroelectric gate at room temperature and yield very similar magnetic coercive fields to those measured without the ferroelectric top layer. Furthermore it shows that the switching kinetics and magnetic domain behavior at the accumulation and depletion states are significantly different (confer “acc” and “dpl” curves in Figure 5.4(d)). This last result is particularly encouraging in context of the goal of this work to directly control the magnetic domains via the ferroelectric polarization domain patterns.

5.3 Polarization-driven shift of T_C: an insight using Arrott plots

In the previous sections, the experimental study carried out at 300K indicated that the ferromagnetic phase in Co ultrathin layer exists in both accumulation and depletion states. In order to quantitatively evaluate the ferroelectric control of ferromagnetism, it is important to accurately determine T_C value and its shift associated with the ferroelectric polarization reversal.

The method to determine T_C in magnetic layers based on magnetotransport measurements is known as Arrott plots. As described in section 3.3, to perform a complete Arrott plots analysis, one needs to carry out a series of R_{xx} and R_{xy} measurements under different magnetic fields at a wide range of temperatures, ideally including T_C. Due to the limitation of the experimental setup, the highest temperature reachable in the present study was 320K, which is below the Curie point regardless of the poling state of the ferroelectric gate. Therefore T_C has been determined from Arrott plots using an extrapolation procedure.

For each temperature within the range from 80K up to 320K, the resistances R_{xx} and R_{xy} were measured vs. the magnetic field B , which was cycled from +1.4T to -1.4T and *vice versa*. As described in Chapter 3 Arrott plots represent M^2 vs. B/M, hence a parameter proportional to the magnetization needs to be extracted from the magnetotransport measurements. According to the theoretical results discussed in Chapter 3, in this analysis M was replaced by ρ_{xy}/ρ_{xx}^2 (equation (3.4)). The value of ρ_{xy} was taken from the flat part of the hysteresis loop where the magnetization is close to its saturation value. After the P(VDF-TrFE) gate was poled by 20V/2s voltage pulse, the Arrott plots of the accumulated Hall bar were measured for the entire temperature range; then the ferroelectric polarization was reversed and the whole measurements procedure was repeated.

The Arrott plots of the Hall bar in both accumulation and depletion states are shown in Figure 5.6(a)&(b). It is clear from the figure that all the plots up to 320K give out a positive intercepts of the asymptotic from the linear part of the graph at high *B* values. The positive intercepts imply that the transition to the paramagnetic phase occurs above 320K. In order to get the estimated Curie temperature, the intercept values from Arrott plots were plotted vs. temperature for both accumulation and depletion states. The zero value of the intercept obtained via linear extrapolation as shown in Figure 5.6(c) gives the T_C.

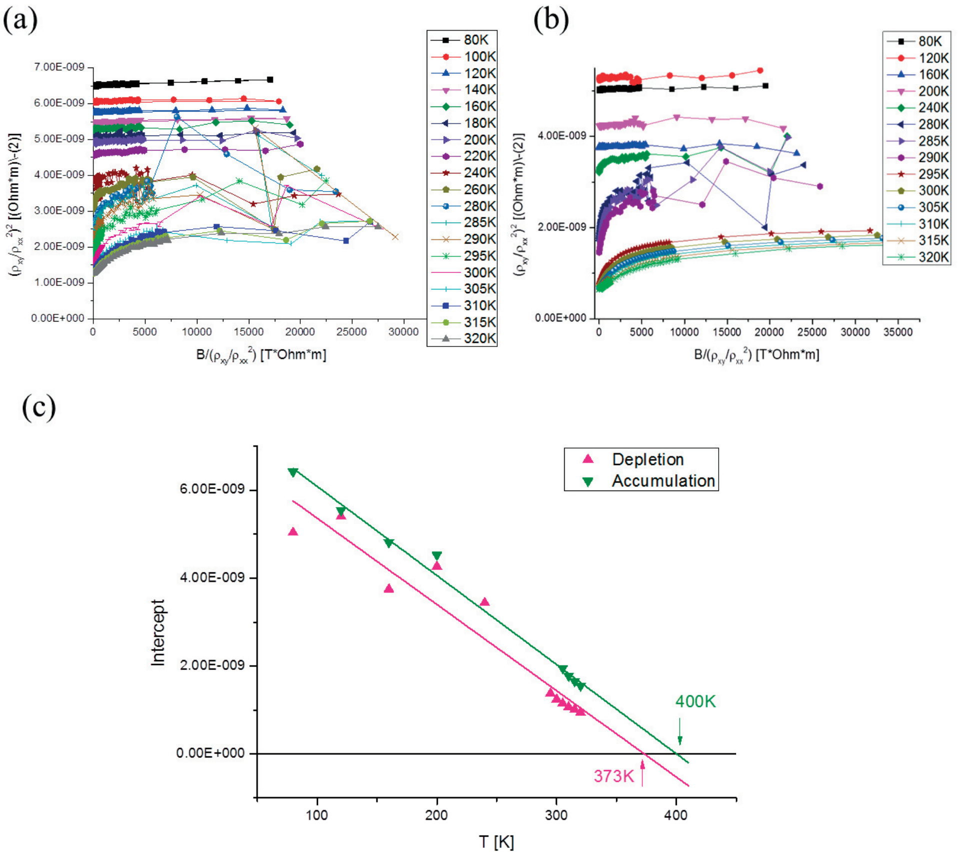

Figure 5.6: Arrott plots from the cobalt Hall bars poled in (a) accumulation and (b) depletion states achieved between 80K and 320K. (c) The temperature dependence of intercepts in accumulation (green line) and depletion (red line) are plotted excluding the obvious highly noisy "bad" plots (for depletion, the plots at T=280K-290K; for accumulation, the plots at T=240K-300K); and the linear extrapolation lines show the temperatures where the intercepts reach zero.

The evaluation of Curie temperature from the Arrott plots in Fig. 5.7 gives for the accumulation and depletion states T_C^{acc}=400K and T_C^{dpl}=373K, respectively. Thus the T_C shift induced by the gate polarization reversal reaches 27K! This significantly exceeds the results from heterostructures with (Ga,Mn)As channels, where the T_C shift was generally within the range of 4-6K.[191,142] However, for a T_C shift normalized to the T_C value (which is approximately 80K for (Ga,Mn)As and 400K for Co channels) both systems exhibit a similar magnitude of T_C modulation of 6-7% relatively. The fact that the non-volatile shift of T_C reachable at room temperature is comparable or even stronger than the results from the cryogenic temperatures is particularly inspiring. Generally, ferroelectric non-volatile gating at room temperature is much more difficult compared to low temperatures because of stronger charge injection and polarization screening. The present results show that for properly fabricated heterostructures, the screening effect can be overcome. The results showing such a strong degree of ferroelectric control of ferromagnetism at room temperature open the way for a number of experiments involving the interplay between ferroelectric and ferromagnetic domains. The key practical issue here is a possibility to get experimental devices out of cryostat and exercise complicate procedures of domain writing and optical and magnetoelectric measurements and different conditions.

It is of interest to compare the magnitude of the T_C shift associated with reversed polarization with the data obtained using conventional gates. As summarized in section 2.3.2, the results on Co thin film from D. Chiba *et al.* show 12K T_C shift by applying ±10V on 50nm HfO_2 (sheet charge density difference: 7μC/cm^2) [179]. The strongest shift ~100K T_C by applying ±2V was reported from ionic liquid film (sheet charge density difference: 50μC/cm^2)[183]. In this context the results from this study look fairly competitive with the shift of 27K T_C using ±20V voltage pulse that switches P(VDF-TrFE) gate in persistent non-volatile way. The maximum induced charge of reversed polarization is also comparable with the conventional gates and reaches 16μC/cm^2.

5.4 Summary

The experiments presented in this chapter clearly demonstrate that the concept of multiferroic heterostructure earlier proved for DMS at cryogenic temperatures works for magnetic metal channels at ambient conditions consistently. The Hall bar devices with ferroelectric gate integrated on the ultrathin cobalt channel have been tested by magnetotransport measurement. The data from AHE (R_{xy}), longitudinal resistance (R_{xx}) and Arrott plots are fully consistent and clearly show that: (i) the Co channel is ferromagnetic at room temperature; (ii) the magnetic state can be altered by ferroelectric polarization reversal. The magnetoresistance data show a substantial non-volatile 27K shift of ferromagnetic T_C associated with the ferroelectric gate operation. This magnitude of the effect is comparable or exceeds the best results observed using the conventional (non-ferroelectric) gates. The manifestations of the change of ferromagnetic state also include an altered domain dynamics, which is of high importance for ferroelectric manipulation of individual magnetic domains addressed in the next chapter.

Chapter 6

Ferroelectric field effect control of ferromagnetic domain kinetics at room temperature

Room temperature ferroelectric control of ferromagnetism demonstrated in Chapter 5 prepares the ground for the central experiments of this thesis, which are focused on direct local control of magnetic domains using the ferroelectric domains. Generally, magnetization in a ferromagnetic media switches in two ways: via nucleation of new domains or growth of already existing domains (known also as domain wall propagation). This chapter addresses ferroelectric control of both of these processes. Because of the local character of interplay between the individual ferroelectric and ferromagnetic domains, the magnetotransport methods used as a main tool in previous chapters need to be combined with a position-sensitive technique. Magneto-optic Kerr effect (MOKE) microscopy is used in these experiments as a major technique for exploring the dynamics of individual magnetic domains in relation with the local non-volatile gate effect associated with ferroelectric polarization domains. Direct measurements of domain wall (DW) velocity and the investigation on the energy of nucleation of new domains enable insight into the profound change of the magnetic properties of the metal channel induced by the persistent polarization switching. From practical perspective the chapter addresses an essential question for application of multiferroic heterostructures in information processing: is it possible to define the point of nucleation and control/stop/enhance magnetic domain propagation by writing/erasing/rewriting a ferroelectric domain at ambient conditions?

6.1 MOKE analysis of magnetic domain nucleation under ferroelectric control

In the series of the MOKE experiments exploring magnetic domain dynamics under ferroelectric control, the first step was to study the nucleation density in relation with the poling state of the gate. These measurements are relatively easy to implement since they do not require fine patterning of the magnetic layer. The experimental technique involving the use of optically transparent gate electrodes has been developed for real-time monitoring of the nucleation density. The numerical analysis using Monte-Carlo simulation enables an insight into the relationship between the measured density of nuclei and the nucleation energy.

6.1.1 Ferroelectric characteristics of P(VDF-TrFE) gate integrated on Co ferromagnetic thin film

In order to study nucleation density in a gated magnetic layer, one needs to monitor a large area covering a vast number of nuclei, where the ferroelectric switching occurs in a simultaneous and uniform way. Therefore the polarization needs to be switched using a broad gate electrode rather than a conductive probe of a scanning probe microscope. The electrode materials routinely used for P(VDF-TrFE) layers such as Pt, Au and Al are not suitable because an optical transparency is required to monitor the magnetic domain nuclei underneath. Thus conventional metal electrodes were replaced the transparent conductive oxide, indium tin oxide (ITO).

Because of the sensitivity of P(VDF-TrFE) to sputtering, a protection 3-7nm Al_2O_3 buffer layer was grown on top of P(VDF-TrFE) by atomic layer deposition (ALD). Then ITO transparent top electrodes were sputtered on top of this protection buffer layer.

In order to optimize the gate processing workflow, the test structures for evaluation of the ferroelectricity were prepared as follows. 100nm sputtered Au on surface-oxidized Si was used as bottom electrodes. Then P(VDF-TrFE) with thickness of 200nm was spin-coated and annealed. The top electrode consisted of Al_2O_3 grown by ALD in 20 and 50 cycles, and finally 100nm sputtered ITO was deposited on the top.

For evaluation of the ferroelectricity in P(VDF-TrFE) after ITO sputtering, *P-E* hysteresis loops were measured on samples with different Al_2O_3 thickness (20 and 50 ALD cycles equivalent to 3nm and 7nm respectively), the results are plotted in Figure 6.1. The two loops have almost same coercive voltage and remnant polarization, indicating that the Al_2O_3 thickness does not cause any degradation of P(VDF-TrFE). Thus the smaller thickness of 3nm (corresponding to 20 ALD cycles) was chosen for the gate fabrication in order to minimize the depolarization effects and enhance the polarization retention.

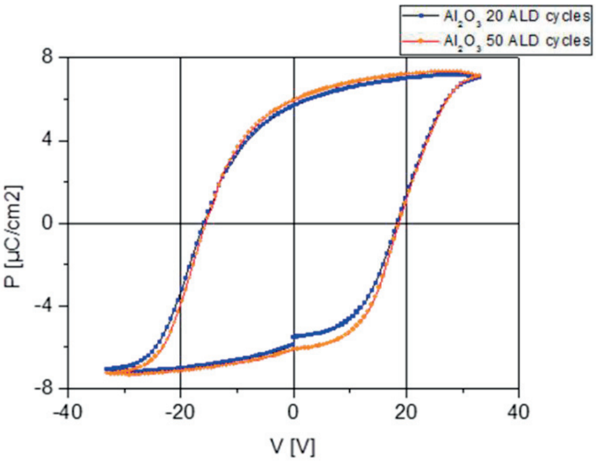

Figure 6.1: *P*-*E* hysteresis loops measured on P(VDF-TrFE) layers with top buffer layer of Al_2O_3 and ITO top electrodes. Al_2O_3 layers were deposited with 20 (blue) and 50 (orange) cycles, equivalent to the thickness of 3nm and 7nm, respectively.

The experimental sample was fabricated from the sputtered Pt/Co/AlO_x wedge multilayers on Si substrate with out-of-plane anisotropy, same as described in Chapter 5. 200nm P(VDF-TrFE) thin film was deposited by spin-coating. Al_2O_3 buffer layer of 3nm was deposited by 20 cycles ALD. Finally 100nm ITO was sputtered over the top using a shadow mask with 2000×550µm rectangular openings. The growth of Al_2O_3 and ITO was done by the group of Micro and NanoMagnetism, Institut Néel, CNRS, Grenoble.

After the sample fabrication, the ferroelectric gate was examined again by measuring *P*-*E* hysteresis that showed polarization of about 6-7µC/cm^2 typical for this material (Figure 6.2), with the coercive field of 800-900kV/cm (16-18V for 200nm co-polymer layer). Therefore the P(VDF-TrFE) gate was fully functional without signs of degradation after top electrode sputtering.

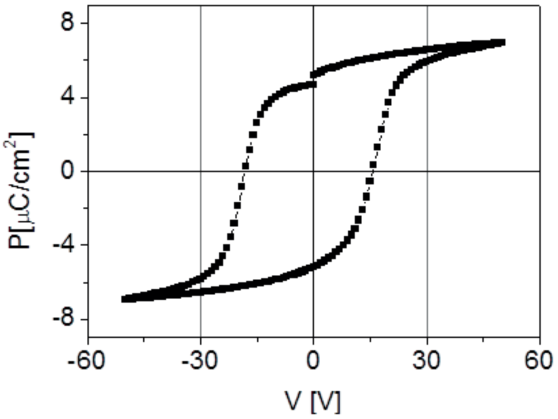

Figure 6.2: Ferroelectric hysteresis loop measured on P(VDF-TrFE)/ITO gate of the experimental structure used for MOKE experiments.

6.1.2 Control (enhancement or suppression) of magnetic domain nucleation in the Co layer by ferroelectric field effect.

In this experiment magnetic domain nuclei were detected by MOKE imaging in the multiferroic heterostructure described above, for both accumulation and depletion states. Non-volatile ferroelectric field effect was induced by poling the gate with voltage pulses of ±20V/2s. A strong magnetic field perpendicular to the surface was used in order to align all Co domains creating a monodomain state. The region where Co layer has an out-of-plane easy magnetic axis was chosen for the experiment. The MOKE image taken in this monodomain state was used as a reference in order to subtract the background during the data processing. This treatment helps separating the useful MOKE signal coming from magnetic domains from the parasitic contributions coming from the topography and surface profile inhomogeneities. Then by applying the opposite magnetic field as 50ms pulse close to the coercive value, the nucleation and expansion of new magnetic domains were monitored. The entire experiment was carried out at the room temperature.

Figure 6.3(a)&(b) illustrate the coupling between the polarization and magnetic domain nucleation that is readily observed in the wedge section with low magnetic anisotropy energy (MAE) where the nucleation density is high. The regions where magnetization was switched (non-switched) appear light grey (dark grey) in the images. Note that due to the thickness gradient, the color of central part of ITO electrodes appeared darker than the peripheral areas in Figure 6.3. This gradual change of brightness was also seen in the conventional optical microscopy image (Figure 6.3(a), inset) of the sample surface. This brightness gradient has to be ignored because it does not correspond to any magnetic domain pattern or property variation related to the magnetism. The variation of the nucleation density along the image in Figure 6.3(a) was due to the anisotropy variation in the sample because of the oxidation state changing along the AlO_x wedge.

P(VDF-TrFE) polarization promoted (impeded) the magnetic domain nucleation because of the partial depletion (accumulation) effect induced in the Co layer. This effect is clearly seen in Figure 6.3(a) and (b) where the MOKE image covers both gated (poled) and non-gated (non-poled) areas. The images taken after applying the opposite magnetic field pulse represent partially switched states and clearly show the contrast between the magnetic domains in the gated and non-gated areas. It was observed as a difference in both the nucleated domain size and density. The dynamics of the magnetic domain nucleation and growth in Figure 6.3 can be visualized in the Movies No. 1&2 of the supplementary material of our paper,[224] where the frames were taken versus time at constant magnetic field.

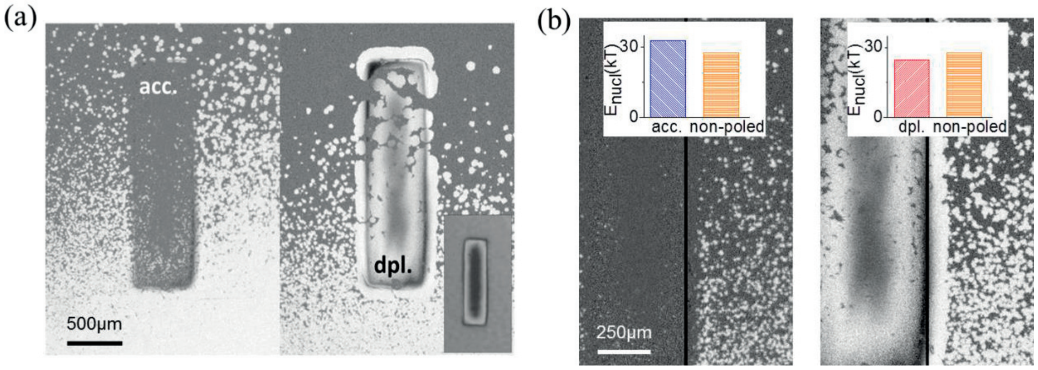

Figure 6.3: MOKE images representing the magnetization reversal (light grey regions) in the high nucleation density regime. The density and size of new magnetic domains occurring below the rectangular gate electrode are clearly different compared to the surrounding (non-poled) areas (the image is taken after applying the magnetic field pulse of 24mT/50ms). (a) The poled ferroelectric gate induced the effect of accumulation (left) or depletion (right). Inset: normal optical image of an ITO electrode. (b) Comparison of the nucleation density below the poled ferroelectric gate and the adjacent non-poled areas. Insets: nucleation energies extracted from the nucleation density for the corresponding areas. Adopted from Ref. 149.

Besides domain visualization, the MOKE technique offers a possibility of analyzing the magnetization hysteresis that can be represented as the normalized Kerr signal vs. magnetic field. During the magnetization reversal, the average grey scale level of the MOKE image is proportional to the net magnetization inside the selected view section. Thus the hysteresis of the ferromagnetic Co film was generated by plotting the grey scale value representing the Kerr signal, versus magnetic field (Figure 6.4). Note that the loops for Figure 6.4(a), (b) and (c) were taken from different locations with different MAE values. From Figure 6.4(a) and (b), it is clear that the accumulation state hardens the magnetism in cobalt, i.e. induces a higher coercive field and remnant magnetization, while depletion provokes the opposite effect. The interpretation of loops in Figure 6.4(c) is more complex. The red plot illustrates the average Kerr signal from the whole view of camera, including the poled area below the electrode and the neighboring region. During the magnetic field cycling, the magnetization always reversed under the electrode in advance (depletion state, lower MAE), and then the outer area followed. This two-steps switching resulted in a distorted hysteresis loop (as seen in Figure 6.4(c) in the red "Mixed" plot), which is actually a superposition of two loops.[‡]

[‡] This two-steps process is very similar to the Hall resistance hysteresis presented in Figure 5.2(b) and (c) which are interpreted as a convolution of loops coming from two domain walls propagating in the Hall bar successively. More discussions found in section 5.2.

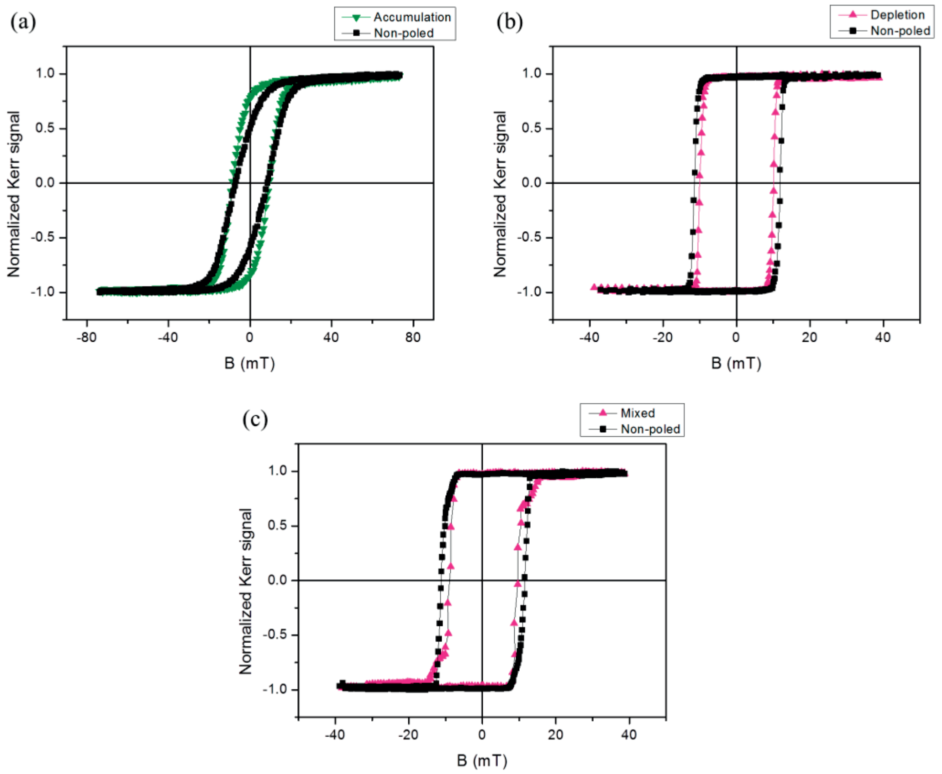

Figure 6.4: Kerr signal hysteresis loops taken on three different locations on the sample. The hysteresis loops are plotted in pairs for comparison: non-poled and accumulated region (a), non-poled and depleted region (b), non-poled region and the whole sight including poled and non-poled parts (c).

Reversing the polarization in P(VDF-TrFE), we could repeatedly change the magnetic domain nucleation density under the electrode. For each studied electrode the polarization had been reversed 4-5 times provoking the reproducible effect of increasing or reducing the magnetic domain nucleation density by this purely electrical manipulation.

In order to quantify the ferroelectric field effect on the magnetic switching, we have carried out a comparative analysis of the nucleation density for the magnetic domains in the poled and non-poled areas. These data were processed using the formalism of Néel-Brown model, which has been previously used for analyzing the thermally-activated nucleation in similar samples with conventional (non-ferroelectric) gate.[189] According to the model the nucleation probability reads as:

$$P(t) = 1 - e^{-t/\tau} \tag{5.1}$$

where the nucleation rate is:

$$\frac{1}{\tau} = \frac{1}{\tau_0} e^{-\frac{E_N}{k_B T}} \tag{5.2}$$

and $\tau_0 = 10^{-10}$s is the fixed attempt rate, E_N the energy barrier, and T=300K the environment temperature. The nucleation density within a fixed period (t=1s) can be obtained for varying nucleation energy E_N through Monte-Carlo simulation. These simulation data have been matched to the experimental Kerr images in order to obtain an estimation of E_N.

Comparing the E_N obtained as described above from poled and non-poled areas as shown in Figure 6.3(b) inset, we conclude that ferroelectric field effect causes E_N increase by $5k_BT$ in the accumulation state ($32.6k_BT$ vs. $27.6k_BT$) and decrease by $3k_BT$ in the depletion state ($24.7k_BT$ vs. $27.8k_BT$), i.e. the polarization switching induced a total energy shift $\Delta E_N=8k_BT$ (~0.2eV). This energy shift is of the same order of magnitude as the ΔE_N=0.07eV reported in Ref. 189 where the bias of 10V was applied to 7nm Al_2O_3 and 37nm HfO_2 dielectric gate. In addition, if we assume a typical nucleation volume of 10^3nm^3,[225] the MAE change is of the order of 10^4J/m^3 which is consistent with the anisotropy changes obtained in the same material for electric field of 0.1V/nm.[186]

A close examination of the depletion image in the Figure 6.3(a)&(b) revealed some enhancement of switching occurring at the electrode boundaries. The exact origin of this "outlining effect" could not be identified at the present stage, however most probably it is linked to the electrode deposition process. Specifically a possible explanation may be related to a polarization imprint which occurs near the electrode boundaries.

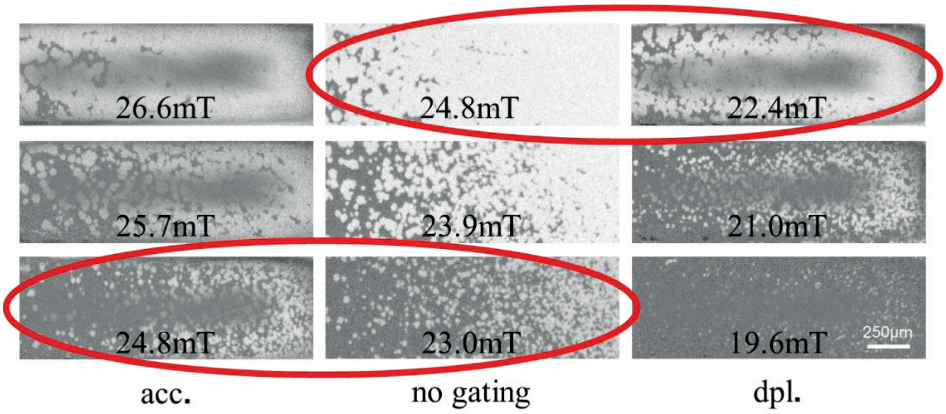

Figure 6.5: Comparison of the MOKE images taken after 50ms, at different magnetic field amplitudes and identification of the pairs of images with similar nucleation densities. Adopted from Ref. 149.

The observed non-volatile change of the domain nucleation energy implies a change of the magnetic field required to trigger the nucleation process. To further explore this effect we performed a series of MOKE measurements at different magnetic fields. Comparing these MOKE images, we attempted to find a pair of images, including one image from the poled and the other one from the non-poled area, where the nucleation densities are similar. This comparative analysis indicates that the nucleation density reached at 24.8mT/50ms in the accumulation state is the same as in the non-poled area at 23.0mT/50ms (Figure 6.5). The other pair of images in Figure 6.5 shows that the same nucleation density is reached for the non-poled area and the area poled in the depletion state at 24.8mT/50ms and 22.4mT/50ms, respectively. Thus the effect of poling the ferroelectric gate in the accumulation/depletion state was equivalent to the nucleation energy change induced by a magnetic field variation of approximately +/-2mT.

The experiments described above clearly show the ferroelectric control of the magnetic domain nucleation due to the sensitivity of MAE to the electric field. In other words, these results show that magnetic domain nucleation can be promoted/ inhibited locally by reversing polarization in the ferroelectric gate.

6.2 Magnetic domain growth in Co ultra-thin layers under ferroelectric control

The study of magnetic domain propagation under ferroelectric control was carried out using the same experimental structure as presented above in the domain nucleation analysis section. This experimental concept benefits from the Co/AlO_x wedge that offers a variable nucleation density that changes continuously along the AlO_x thickness gradient. For analyzing the nucleation probability, the regions with high nucleation density were privileged. On the other hand due to the high nucleation density, the growing domains tend to overlap. This complicates monitoring the growth of individual domains and accurate determining DW velocity. Therefore for DW velocity measurement we chose a different region of the wedge where the higher oxidation degree resulted in a higher MAE and a lower nucleation probability. In this region the ferromagnetic switching was triggered in a very few nucleation sites (Figure 6.6) and time-dependent evolution of each individual domain could be monitored.

The change of V_{DW} induced by the ferroelectric gate could be clearly noticed by bare-eye observation of the domain growth close to the edge of the ITO electrode. Once the nucleus started to expand, a section of DW immediately entered into the gated region in the depletion state while its remaining part propagated in the normal non-gated cobalt film. As shown in Figure 6.6, the boundary of this domain did not preserve the circular shape commonly observed under isotropic growth conditions. The origin of the domain shape distortion is the difference in the velocities of DW propagation, which is faster in the poled region (depletion) than in the surrounding unpoled area.

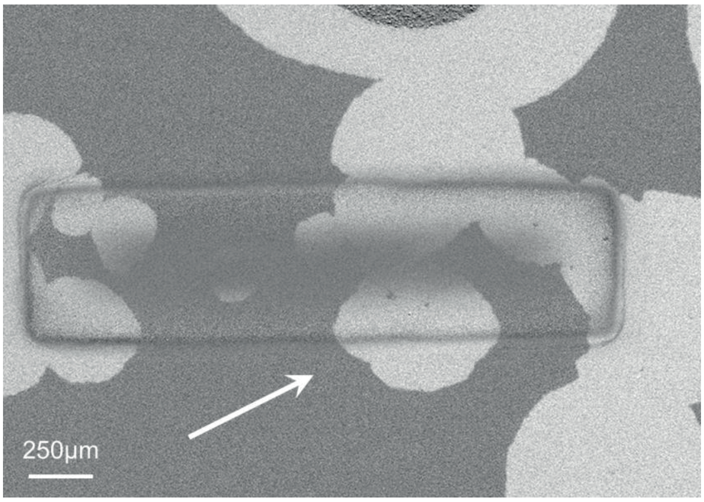

Figure 6.6: Domain expansion across the boundary between poled and unpoled areas. The distortion of the shape of the domain that nucleated close to the electrode boundary (marked with the arrow) reflects the V_{DW} difference in poled and unpoled areas.

A quantitative characterization on the field-effect modification of V_{DW} was done by detecting the domain wall position vs. time under a constant magnetic field. Two pairs of domain walls were chosen to compare the speed difference in unpoled, accumulation and depletion states. Each pair was chosen from the DWs moving at the same "altitude" of AlO_x wedge thickness to avoid an error related to MAE shifting. For better accuracy, domain boundary segments orthogonal to the direction of the domain propagation were selected for further analysis. Figure 6.7 displays four chronological series of images showing the two pairs of propagating DWs. Each pair includes the DWs captured from the same "altitude" of AlO_x wedge (the same MAE). The images of each set have been taken sequentially with identical time intervals of ~1s under constant magnetic field. First two series show DW movement measured in the accumulation (a) and non-poled (b) states under 12mT magnetic field, the dark grey color represents the switched region. Similarly, the series (c) and (d) show the propagation of domains for the depletion and non-poled states, respectively, measured at 13mT field, the bright color represents the switched region.

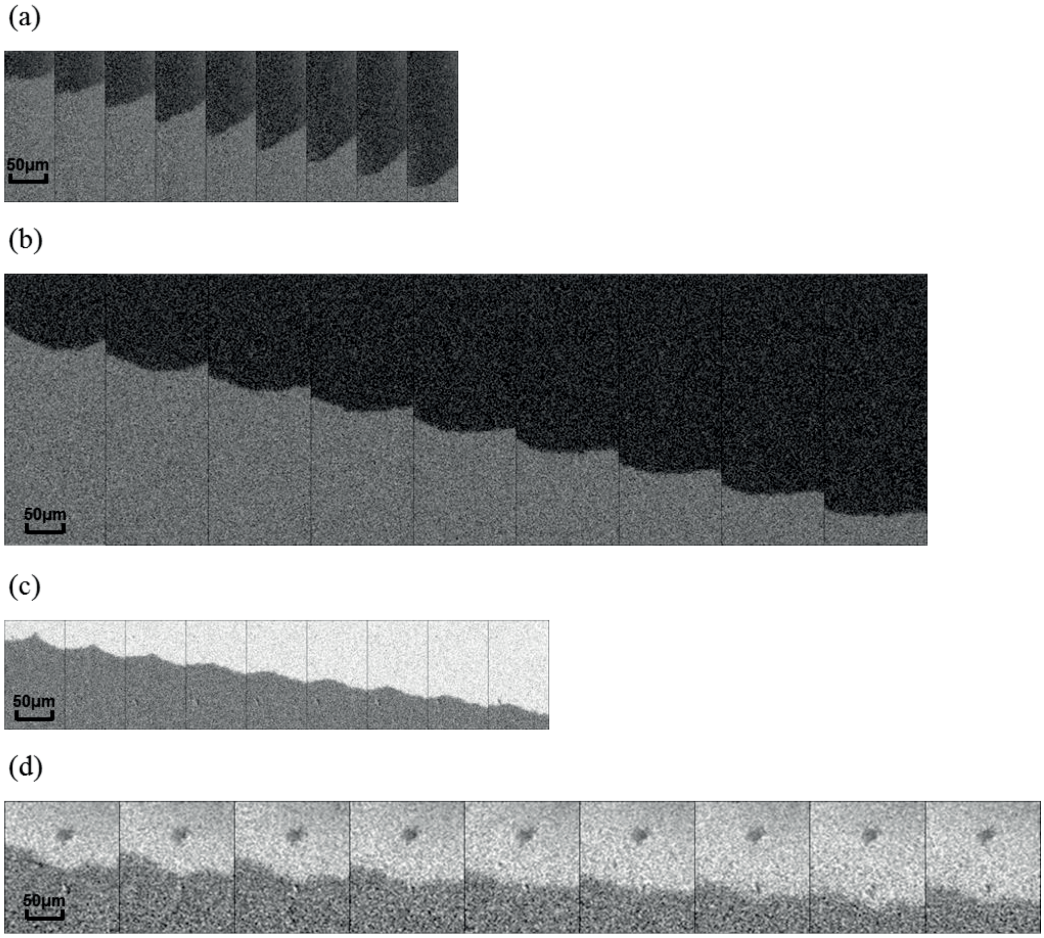

Figure 6.7: Four sets of images showing DW propagation for a low nucleation density region. The velocity comparisons are made between accumulated (a) and non-poled (b) areas, and between the depleted (c) and non-poled (d) areas.

As presented in Figure 6.8, all the plots of DW displacements vs. time show a good linearity, demonstrating constant DW speeds in all three poling states and endorsing the uniformity of polarization under ITO electrodes. After extracting the individual slopes of the four plots, we can conclude that in the depletion state the DW velocity increases by a factor of 2.2 while in the accumulation state it decreases by factor 1.6 with respect to the non-poled state.

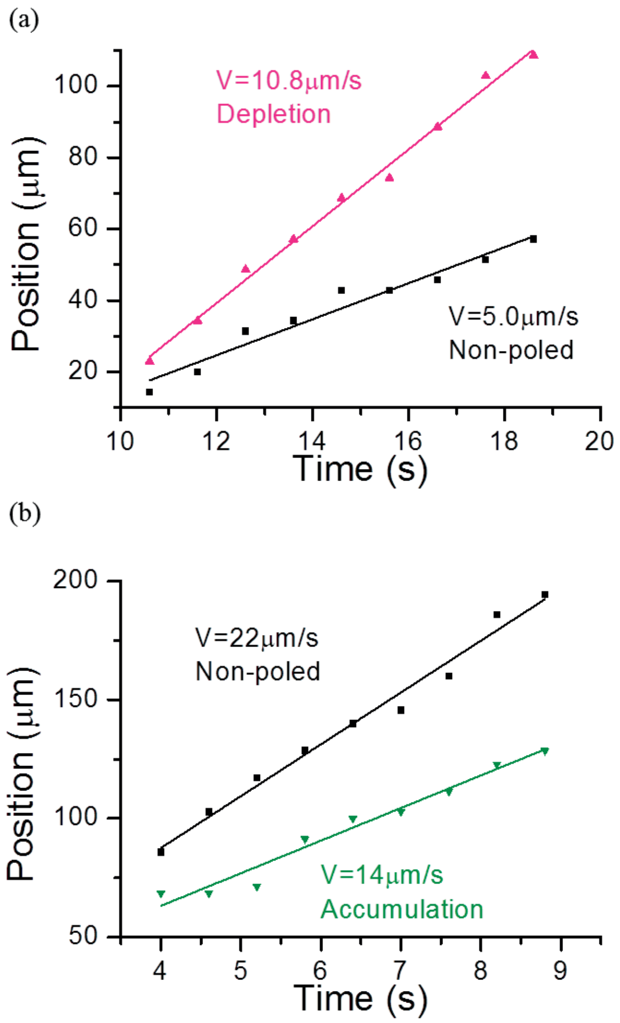

Figure 6.8: Plots of DW positions vs. time and linear fits for the four DWs shown in Figure 6.7. The slope comparisons show a factor of 2.2 of speed increasing for the depletion state (a) and 1.6 of decreasing for the accumulation state (b), respectively.[149]

The comparison of the DW velocity change in the identically grown magnetic layers with ferroelectric and dielectric gates enables us to estimate the magnitude of the net charge density associated with the spontaneous polarization. For instance, the DW velocity decrease by factor 1.6 shown in Figure 6.8(b) can be compared to a similar effect achieved by applying 2V to the 7nm Al_2O_3/37nm HfO_2 gate.[189] In case of this non-ferroelectric gate, the charge density induced at the interface between the dielectric layer and magnetic channel is about 0.7μC/cm^2. Hence, the induced charge at the P(VDF-TrFE)/Co interface is likely to be the same. In other words the ferroelectric polarization reversal provides about 1.4μC/cm^2 net charge.

On the other hand, polarization hysteresis measurements in Figure 6.2 show that the spontaneous polarization of the ferroelectric gate is close to 6μC/cm^2, and the switchable charge is about 12μC/cm^2 i.e. almost an order of magnitude higher than the estimate obtained from comparison with the dielectric gate. This discrepancy can be explained by a strong screening of the spontaneous polarization charge in the layer adjacent to the ferroelectric film interface. The fundamental origin of this effect is linked to the existence of so-called "dead layer" at the ferroelectric film interface[226]. The degradation of ferroelectricity in this layer resulted in a very high electric field occurring when P(VDF-TrFE) was poled as discussed in Chapter 1. The charge injection to the dead layer induced by this field caused screening of the spontaneous polarization and significantly reduced the gate effect. For P(VDF-TrFE) ferroelectric gates integrated on a wide range of materials, like wide-gap semiconductor heterostructures[46] and heavily doped magnetic semiconductors[192], similar effect of polarization screening has been observed. These results suggest that by improving the structural quality and dielectric strength of the interface-adjacent layers of ferroelectric films, the non-volatile gate effect has the potential to be significantly enhanced.

6.3 Ferroelectric control of magnetic anisotropy energy (MAE)

6.3.1 Analysis of MAE based on DW kinetics

Systematic measurements of DW velocity at different magnetic fields enable an insight into a fundamental property governing the behavior of the magnetic media, the magnetic anisotropy energy (MAE). The formalism that was used in order to quantify the effect of ferroelectric gate on MAE constant K is summarized below.

The measurements of DW velocity using MOKE imaging were carried out at low magnetic fields, where domain walls move in creep regime as described in Chapter 2. In the creep regime, the DW velocity depends on the magnetic field H and the properties of material as follows:[120]

$$V = V_0\, exp\left(-\frac{\alpha}{k_B T} H^{-\frac{1}{4}}\right) = V_0 exp\left[-\left(\frac{H^{eff}}{H}\right)^{\frac{1}{4}}\right] \tag{6.1}$$

where V_0 is the characteristic speed, α is the creep-scaling constant, k_B is the Boltzmann constant, T is the temperature and H^{eff} is the effective critical field.

To establish the relation between K and α, we adopt here the creep-scaling law proposed in Ref. 227 that yields the proportionality $\alpha \propto U_C H_{crit}^{1/4}$, where U_C and H_{crit} are the scaling energy constant and the critical field, respectively. According to Ref. 227, the quantities of U_C and H_{crit}, in turn, follow the relations:

$$U_C \propto \left(f_{pin}^2 \cdot \sigma_{DW}\right)^{1/3},\ H_{crit} \propto \left(f_{pin}^4 / \sigma_{DW}\right)^{1/3} \tag{6.2}$$

where f_{pin} and σ_{DW} are the local pinning force and the DW energy density per unit area, respectively.

Note that f_{pin} is inversely proportional to the DW width δ_{DW}. For ferromagnetic materials with a uniaxial magnetic anisotropy K, it is established[159] that σ_{DW} and δ_{DW} are linked to K as follows:

$$\sigma_{DW} \propto K^{\frac{1}{2}},\ \delta_{DW} \propto K^{-\frac{1}{2}} \tag{6.3}$$

Thus, one finally arrives at:[228]

$$\alpha \propto K^{5/8} \tag{6.4}$$

Therefore MAE can be evaluated based on the DW velocity data as follows: first one needs to measure the dependence of V_{DW} on magnetic field; then extract the creep-scaling constant α from equation (6.1); and use the relation (6.4) to quantify the relative strength of MAE from the value of α. Finally, through measuring the velocity change brought by the polarization reversal, the ferroelectric effect on MAE change can be extracted.

Typical plots of V_{DW} vs. H that were extracted from our MOKE experiments are shown in Figure 6.9. For the data plotted as log. V_{DW} vs. $H^{-1/4}$, the linear relations are clearly observed (Figure 6.9(b)), and the slopes of the fitting lines give the creep-scaling constant α.

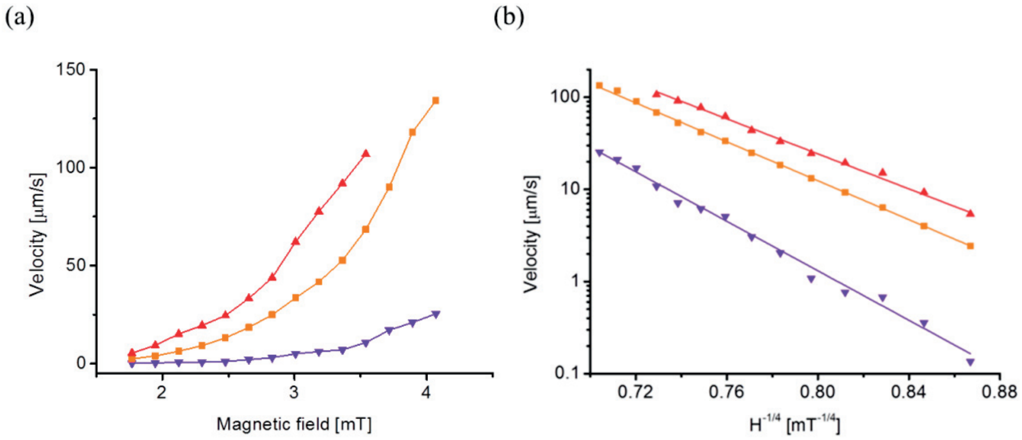

Figure 6.9: Typical V_{DW}-H characteristics for the domain growth in the creep regime measured on the Pt/Co/AlO$_x$ stack. The data are plotted in conventional linear coordinates (a) and as log. V_{DW} vs. $H^{-1/4}$ (b).

6.3.2 DW velocities under ferroelectric control measured at different magnetic fields: MAE change

In this series of experiments we measured directly the magnetic DW velocities at different magnetic fields and thereafter determined the MAE change in relationship with the non-volatile gate polarization. All experiments described above had been carried out on a continuous magnetic/ferroelectric multilayer where the spontaneous polarization was switched via large gate electrodes. In these measurements we used magnetic media patterned as channel arrays that enabled us to measure single magnetic DW velocity with a better accuracy. Additionally, the 1D channels allowed for exploring the interplay between the propagating magnetic domains and polarization domains that were individually created using AFM probe scanning.

As described in section 3.10 channel width of 10µm was chosen because of the severe degradation of ferromagnetism observed when the channel width was scaled down further. The preparation of Pt/Co/AlO_x wedge stack was the same as described in the previous section. Using photolithography and ion-beam etching, the multilayer was structured as arrays of parallel 10×1000μm^2 channels (Figure 6.10). The channel direction was perpendicular to the wedge axis so that the AlO_x thickness (and hence MAE) remained unchanged along the channel. After patterning the magnetic media, 100nm P(VDF-TrFE) ferroelectric layer was spin-coated on it, using 1.5 wt% solution of P(VDF-TrFE) at 1800rpm rotation speed and subsequently crystallized into ferroelectric phase at 130˚C for 1h.

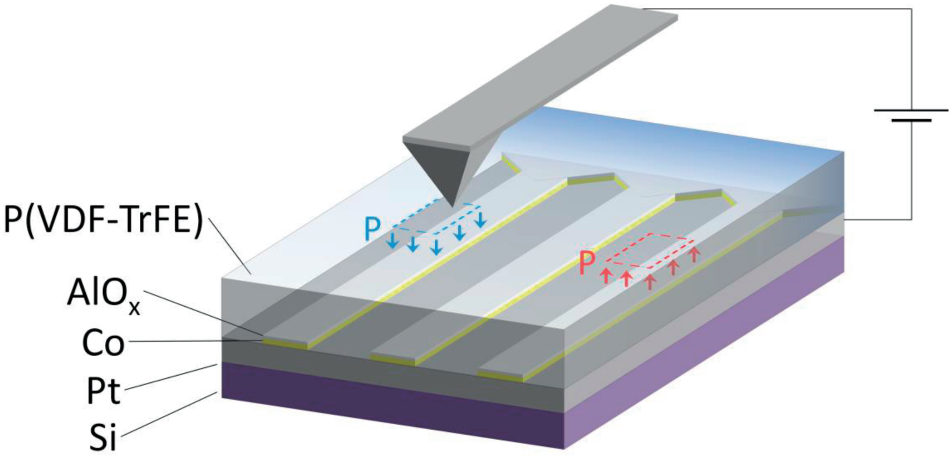

Figure 6.10: The schematic structure of Pt/Co/AlO_x channel array covered with P(VDF-TrFE) ferroelectric copolymer layer. The gate was locally poled using conductive AFM probe.

As shown in Figure 6.10, large millimeter-size regions connected to the channel arrays worked as “reservoirs” where the magnetic domains were nucleated and subsequently injected into the individual channels for MOKE monitoring. In absence of top solid electrodes P(VDF-TrFE) gate was poled using a conductive AFM probe with 2N/m spring constant. To pole a part of the selected 10µm wide channel, we scanned a 15×15μm^2 area while applying +/-10V to the AFM probe using an external voltage source. The poled sections of the channel had a length of 30µm achieved by sequential poling of two adjacent 15×15μm^2 regions, providing enough space to control DW movement and obtain sufficient number of images.

The movement of the magnetic DWs in the Co thin film was monitored with the magnetic field being applied out of plane and all the measurements were carried out at room temperature. The measurement started with detecting the speed of three adjacent channels under the same poling conditions; then two 15×30μm^2 regions with opposite polarization in P(VDF-TrFE) were prepared on the two channels by AFM, while the third channel in the middle remained unpoled. After preparing the channels this way, the DW velocity was extracted from MOKE images collected at fixed intervals (100ms).

In order to extract α and subsequently MAE, it is necessary to measure V_{DW} under several different magnetic fields within the DW creeping range. In this experiment V_{DW} was measured on each individual poled section for more than 10 magnetic field values ranging from 1.2mT to 3.8mT.

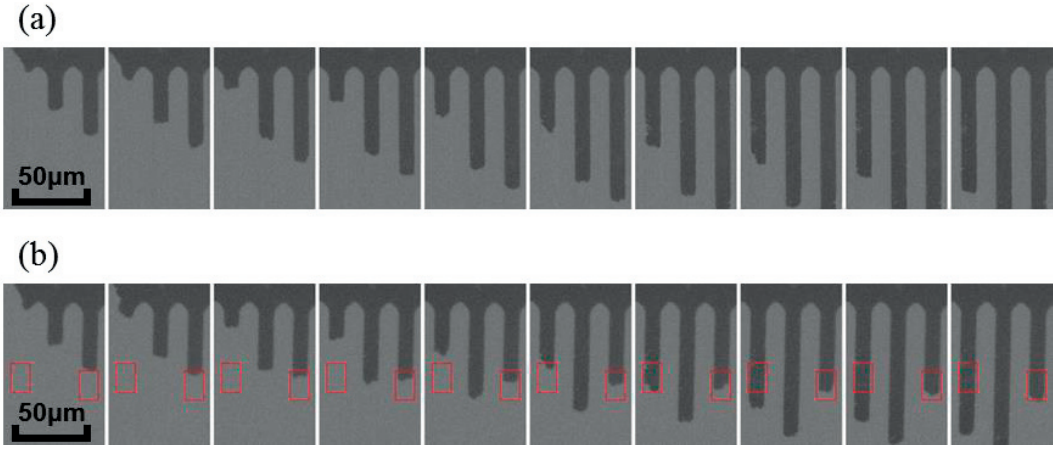

Figure 6.11: Sequential MOKE images captured with time intervals of 100ms under constant magnetic field with blank P(VDF-TrFE) gate (a) and two 15×30μm^2 poled regions marked by red frames (b). The red frame markers indicate the places where the top P(VDF-TrFE) layer was poled with the probe voltage of -10V (left) and +10V (right).

The MOKE data in Figure 6.11(a)&(b) extracted from the images measured with constant intervals of 100ms show propagation of switched magnetic domains (dark grey) under constant magnetic field. Figure 6.11(a) presents data from unpoled ferroelectric gate, showing similar DW propagation velocities in three adjacent channels. Moreover in agreement with previous results,[149,189] the accumulation/ depletion effect associated with the polarization reversal significantly impacts MAE, provoking a change of DW velocity. Concurrent observation of domain wall movement within the array of channels with identical geometry clearly demonstrates the ferroelectric gate effect. The areas marked with red rectangular frames in Figure 6.11(b) were poled by applying -10V (+10V) to the AFM probe for the left (right) channel. The MOKE images taken after poling reveal the DW velocity increase (decrease) within the poled regions of the left (right) channel with respect to the unpoled reference channel in the middle.

In order to represent V_{DW} profile across the channel including poled and non-poled sections, Figure 6.12 shows local V_{DW} vs. DW position. The velocity was calculated from the snapshots of DW positions at different times, for different positions along the magnetic channel. It is remarkable that the domain velocity is affected within the region of 30µm that is exactly the poled region length, whereas outside poled areas the DW velocity in both channels remains the same. The analysis shows a 4-times DW velocity difference (10µm/s vs. 40µm/s) between positively and negatively poled regions. And the velocity values indicate that the DW motion is in the creeping regime[185,189], allowing the application of the formalism presented in section 6.3.1.

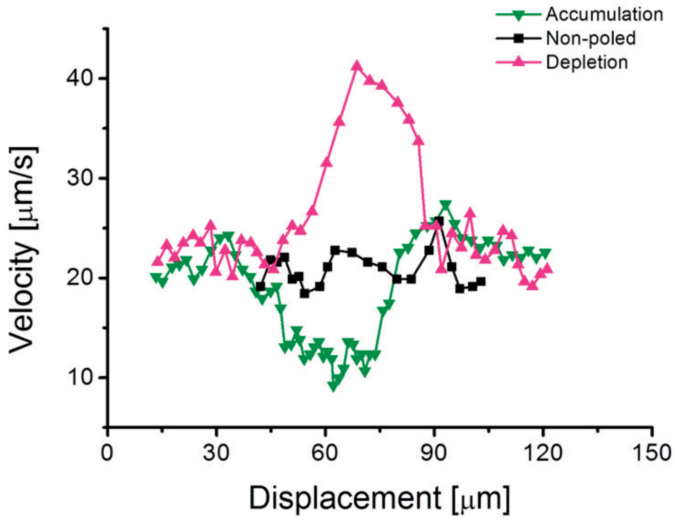

Figure 6.12: Domain wall velocity V_{DW} measured along the channels with unpoled gate (black) and with gates poled to the accumulation (green) and depletion (red) states. V_{DW} significantly changes within the 30 µm poled regions whereas outside these regions it is same for both channels.

The DW propagation measurements were repeated for different magnetic fields and the results were plotted as log. V_{DW} vs. $H^{-1/4}$ for the channels with two alternative polarization directions and non-poled reference channel (Figure 6.13(a)). V_{DW} follows the creeping law as expected, and H^{eff} changes by a factor 4 between the accumulation and depletion state as a consequence of the ferroelectric-gate-induced MAE change. The inset pillar diagram shows relative MAE calculated according to Equation (6.4). The change of K in the gated Co thin film in the accumulation state is 74% higher than that in the depletion state.

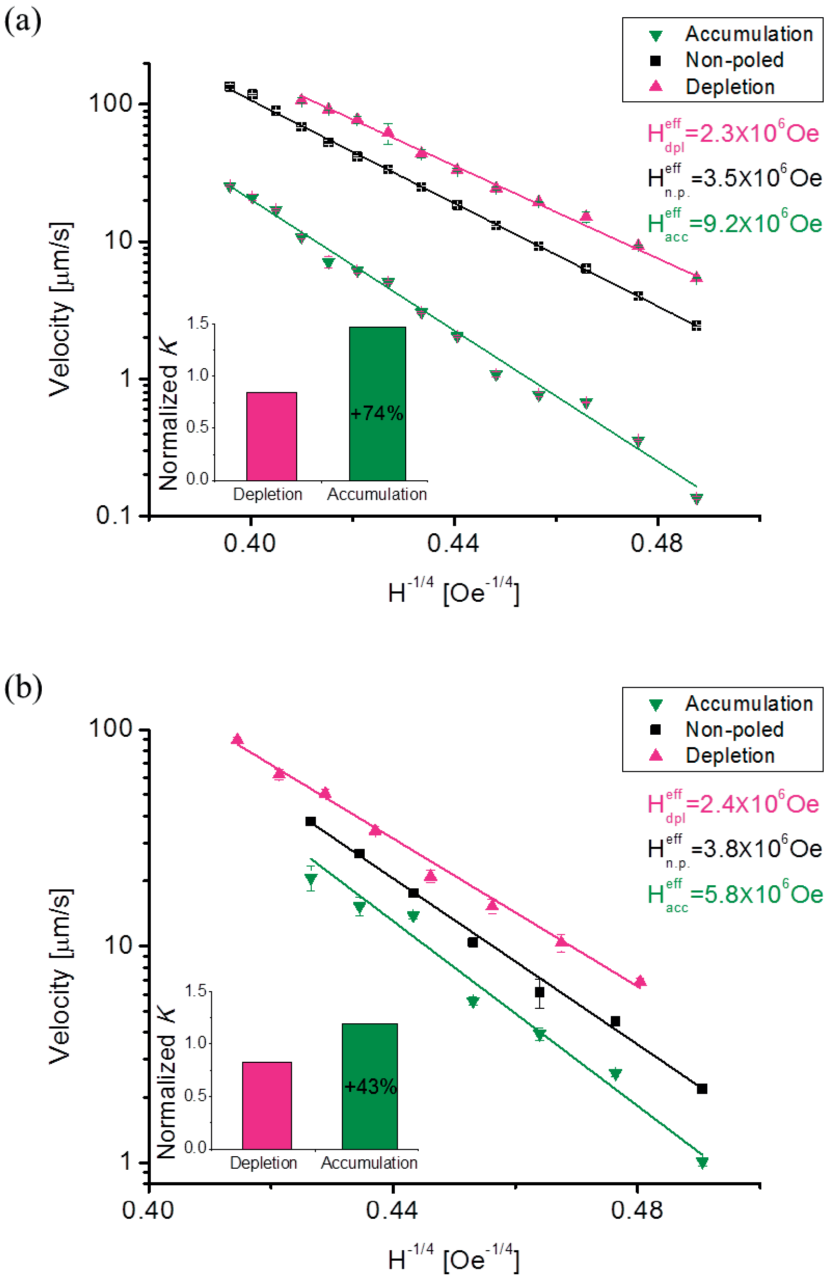

Figure 6.13: Extracting the change of anisotropy energy constant K from slopes of V_{DW}-$H^{1/4}$ plots. The black, red and green plots represent measurements for gates in non-poled state, depletion and accumulation states, respectively. The extracted H^{eff} values are listed under three different poling states. The measurements performed within 2 days after poling (a) show 74% difference of K between opposite polarizations, while the measurements repeated after 60 days delay (b) show the K difference of 43%.

The change of MAE entails a strong difference of DW velocity between the accumulation and depletion states that ranges from factor 4 to 20 (Figure 6.13(a)), depending on the external magnetic field. In particular, at the creeping speed range ~10-100μm/s, the non-volatile gate effect brings one order of magnitude difference.

This magnitude significantly exceeds the earlier observed ferroelectric gate effect in similar structure with ITO gate electrodes[149], where the DW velocity change reached a factor of 2.2 of speed increase for the depletion state and 1.6 times decrease for accumulation gating. This large ferroelectric gate effect enhancement can be attributed to two reasons: a weaker polarization screening due to the improved ferroelectric/ ferromagnetic interface consisting of a thin dielectric AlO_x wedge without ALD Al_2O_3 protection layer; and higher uniformity and stability of polarization domains created by AFM probe compared to the sub-millimeter gate electrode.

Direct comparison of the effect induced by ferroelectric gate and HfO_2/Al_2O_3 dielectric gate suggests that in our earlier results[149] in section 6.2 the net (non-compensated) switching polarization was about $0.7\mu C/cm^2$. In this section, the strong difference of DW velocity ranged from factor 4 to 20 depending on the applied magnetic field, and we take a factor 10 as an average value for estimating the effective charge density. As reported in Ref. 189, the 10 times V_{DW} change was achieved by 15V gate voltage that generates total charge density of $5\mu C/cm^2$. The net switching charge density of $5\mu C/cm^2$ is about 40% of the theoretical limit of the total switching polarization charge, i.e. double remnant polarization of P(VDF-TrFE) $2P_r=12\mu C/cm^2$. This huge enhancement of the ferroelectric gate performance compared to the switching charge of $1.4\mu C/cm^2$ reported in section 6.2 demonstrates a potential of the multiferroic heterostructures and the importance of optimization of the interface between the ferroelectric and ferromagnetic media.

Non-volatile memory effect represents an essential advantage of ferroelectric gate compared to the conventional dielectric gates. Generally in ferroelectric FET devices the stability of the switched state suffers from depolarization effects and spontaneous polarization screening. In order to evaluate the retention i.e. the ability of the channels to preserve the changed magnetic properties after poling, we have repeated the experiment described above 60 days after poling the gate. During this time the sample was stored at ambient conditions. The results in Figure 6.13 (b) show a strong retention effect with H^{eff} difference between the accumulation and depletion states about 250%. Comparing the values of K extracted using Equation (6.4) for the accumulation and depletion states one obtains a difference 43%. This result attests to a stability and true non-volatile character of ferroelectric control of ferromagnetism in the studied multiferroic heterostructure.

6.4 Summary

The experimental results reported in this chapter represent the most important part of the thesis. In the introductory statement of the chapter the essential question for future consideration of multiferroic heterostructures for information processing was formulated as follows: is it possible to define the point of nucleation and control/stop/enhance magnetic domain propagation by writing/erasing/rewriting a ferroelectric domain at ambient conditions? Based on the experimental results one can reply to this question positively.

The interplay between the reversed ferroelectric domains and dynamics of individual magnetic domains has been explored using a combination of magneto-electrical, magneto-optic and scanning probe experiments. The ferroelectric domains projected onto the magnetic channel were shown to change locally the magnetic anisotropy energy, resulting in significantly altered magnetic domain dynamics. The reversal of the gate polarization from the accumulation to depletion state resulted in a magnetic domain nucleation energy decrease by 0.2eV. The experimental data suggest that with further optimization of the ferroelectric/ ferromagnetic interface, the effect can be significantly enhanced.

A dramatic ferroelectric-gate-induced change of the DW velocity by factor 4-20 depending on the magnetic field range enables an insight into the field effect control of the magnetic anisotropy. The evaluation based on DW velocity data at different magnetic fields yields the magnetic anisotropy energy constant change by factor >1.7 driven by the ferroelectric gate switching. Direct writing of ferroelectric domains on selected micron size channels allowed for purely electrical acceleration/deceleration of individual magnetic domains within the selected segments of their tracks.

The magnitude of the gate effect was shown to be comparable with conventional dielectric gates integrated on magnetic metal channels for room temperature operation. The ability to preserve the field effect after the gate bias has been switched off is a major feature differentiating the ferroelectric gate from conventional dielectric gates. A strong 60 days retention performance shows that the ferroelectric gate effect is truly stable and non-volatile.

Conclusions and Outlook

The goals of the thesis were to understand and exploit the phenomena of magnetoelectric coupling in ferroelectric/ferromagnetic heterostructures in order to reach a robust ferroelectric control of ferromagnetism. The following major issues were addressed in this work:

- Extension of ferroelectric control of ferromagnetism from the cryogenic temperature range to the ambient conditions.
- Moving from a uniform switch of the magnetic state within the broad gated area to the non-volatile local control of individual magnetic domains using the individual ferroelectric domains.
- Upgrading from a weak modulation of the ferromagnetic state to a strong, ideally deterministic switching of the ferromagnetism driven by the polarization reversal.

The results of this thesis work constitute a significant advancement towards the major targets outlined above.

Room-temperature ferroelectric control of ferromagnetism has been demonstrated on ferromagnetic metal (Co) channels with ferroelectric polymer gate. Diverse techniques including magnetoelectric and magneto-optical measurements revealed the ferroelectric control of ferromagnetic Curie temperature and magnetic anisotropy energy. Rather than the magnetoelectric coupling via volatile dielectric gates or mechanical interfacial strain demonstrated earlier, this non-volatile effect is purely electrical, reversible and reproducible as expected for a ferroelectric field effect device.

The local character of the interplay between the individual ferroelectric and ferromagnetic domains has been demonstrated by showing control of nucleation and propagation processes of individual magnetic domains imprinted from the artificially controlled domain writing in the P(VDF-TrFE) layer. The experiments carried out at ambient conditions proved that nucleation of magnetic domains can be promoted (or impeded) at a selected place by poling the gate material; and local control of magnetic domain velocity has been achieved in 1D and 2D geometries. In particular, we were capable to accelerate/slow down the propagation of magnetic domains in a narrow channel by selectively poling chosen sections of the ferroelectric gate. The ferroelectric domains could be erased/rewritten ensuring a nondestructive and reversible tool to control the magnetic domain dynamics.

Electric-field-controlled persistent switching of the AMR has been observed in the FeFET structure with ultra-thin (Ga,Mn)(As,P). The essential features include the possibility of non-volatile, ferroelectric-gate-driven modulation/suppression of the AMR signal. A deterministic on/off switching of the crystalline AMR component associated with the polarization reversal in the gate has been demonstrated. From the application prospective, these results show a different mode of multiferroic device operation compared to magnetic domain control via tuning of magnetic anisotropy.

The quantitative characteristics of the ferroelectric control of ferromagnetism including the T_C shift, the change of magnetic domain nucleation energy and the magnetic anisotropy constant are comparable or exceed the results previously achieved using the conventional volatile (non-ferroelectric) gates.

From the processing and device implementation point of view, the important outcome of this thesis is a workflow for multiferroic heterostructure processing. A solution for ferroelectric gate integration without destroying ferromagnetism in the delicate ultrathin metal channel has been presented. Integration of transparent gate electrodes suitable for magneto-optical measurements is another addition to the experimental toolbox developed in this work. And the ferroelectric domain writing using a conductive AFM probe was accomplished in the multiferroic device, proven with high uniformity and stability. The optimal treatment of the ferroelectric layer resulted in a significant enhancement of the gate effect compared to previous reports.

These results confirm the viability of multiferroic heterostructures for spintronic devices. The demonstration of room-temperature operation of the multiferroic FET structure and local interplay between individual ferroelectric and ferromagnetic domains increase the confidence in a feasible future of novel multiferroic memories and logic elements. On the other hand ample challenges need to be overcome in order to make this development a reality. In spite of the significant enhancement of multiferroic coupling reported in this work, a true deterministic coupled ferroelectric/ferromagnetic switching is not yet achieved. Furthermore, for practical applications the ferroelectric control of magnetic domain velocity in the creep regime shown in this work needs to be extended to the high-field regime, which will require even stronger magnetic anisotropy control. Further progress in this direction will require a more responsive magnetic material and a higher net charge of the ferroelectric gating for a more predominant magnetoelectric coupling. The multiferroic heterostructure represents a type of FeFET device, therefore all issues of FeFETs including charge screening, retention loss and imprinting are of importance for the explored system. However, the results of this thesis demonstrate that there is a lot of unexploited potential for further improvement in both the ferroelectric and the ferromagnetic supplements. It is hoped that the experimental techniques and approaches developed in this work will provide a solid basis for further exploring ferromagnetic/ferroelectric heterostructures with strong multiferroic coupling.

Reference

1 J. Curie, P. Curie. Développement, par pression, de l'électricité polaire dans les cristaux hémièdres à faces inclinées. *Comptes Rendus de l'Academie des Sciences,* **91,** 383 (1880).

2 J. Valasek. Piezoelectric and allied phenomena in rochelle salt. *Physical Review,* **17,** 475 (1921).

3 V. Ginsburg. Dielectric properties of ferroelectric crystals and of barium titanate. *Zhurnal eksperimentalnoi i teoreticheskoi fiziki,* **15,** 739 (1945).

4 K. Nakamura, Y. Wada. Piezoelectricity, pyroelectricity, and the electrostriction constant of poly(vinylidene fluoride). *Journal of Polymer Science Part A-2: Polymer Physics,* **9,** 161 (1971).

5 J. Anderson. Ferroelectric storage elements for digital computers and switching systems. *Electrical Engineering,* **71,** 916 (1952).

6 A. Tagantsev, L. Cross, J. Fousek. *Domains in Ferroic Crystals and Thin Films.* Springer (2010).

7 J. Slater. The Lorentz Correction in Barium Titanate. *Physical Review,* **78,** 748 (1950).

8 D. Damjanovic. Ferroelectric, dielectric and piezoelectric properties of ferroelectric thin films and ceramics. *Reports on Progress in Physics,* **61,** 1267 (1998).

9 G. Goldsmith, J. White. Ferroelectric behavior of thiourea. *Journal of Chemical Physics,* **31,** 1175 (1959).

10 P. Szklarz, G. Bator. Pyroelectric properties of tricyclohexylmethanol (TCHM) single crystal. *Journal of Physics and Chemistry of Solids,* **66,** 121 (2005).

11 S. Horiuchi, Y. Tokura. Organic ferroelectrics. *Nature Materials,* **7,** 357 (2008).

12 M. Lines, A. Glass. *Principles and applications of ferroelectrics and related materials.* International series of monographs on physics. Clarendon Press (1977).

13 A. Devonshire. *Philosophical Magazine,* **40,** 1040 (1949).

14 A. Devonshire. Theory of ferroelectrics. *Advances in Physics,* **3,** 85 (1954).

15 M. Haun, E. Furman, S. Jang, H. McKinstry, L. Cross. Thermodynamic theory of $PbTiO_3$. *Journal of Applied Physics,* **62,** 3331 (1987).

16 W. Merz. Domain formation and domain wall motions in ferroelectric $BaTiO_3$ single crystals. *Physical Review,* **95,** 690 (1954).

17 E. Little. Dynamic behavior of domain walls in barium titanate. *Physical Review,* **98,** 978 (1955).

18 W. Merz. Switching time in ferroelectric $BaTiO_3$ and its dependence on crystal thickness. *Journal of Applied Physics,* **27,** 938 (1956).

19 R. Landauer. Electrostatic considerations in $BaTiO_3$ domain formation during polarization reversal. *Journal of Applied Physics,* **28,** 227 (1957).

20 G. Gerra, A. Tagantsev, N. Setter. Surface stimulated nucleation of reverse domains in ferroelectrics. *Physical Review Letters,* **94,** 107602 (2005).

21 F. Xu, S. Trolier-McKinstry, W. Ren, B. Xu, Z. Xie, K. Hemker. Domain wall motion and its contribution to the dielectric and piezoelectric properties of lead zirconate titanate films. *Journal of Applied Physics,* **89,** 1336 (2001).

22 I. Stolichnov, A. Tagantsev, N. Setter, J. Cross, M. Tsukada. Crossover between nucleation-controlled kinetics and domain wall motion kinetics of polarization reversal in ferroelectric films. *Applied Physics Letters,* **83,** 3362 (2003).

23 R. Miller, A. Savage. Velocity of sidewise 180˚ domain-wall motion in $BaTiO_3$ as a function of the applied electric field. *Physical Review,* **112,** 755 (1958).

24 R. Abe. Theoretical treatment of the movement of 180-degrees domain in $BaTiO_3$ single crystal. *Journal of the Physical Society of Japan,* **14,** 633 (1959).

25 R. Miller, G. Weinreich. Mechanism for the sidewise motion of 180˚ domain walls in barium titanate. *Physical Review,* **117,** 1460 (1960).

26 T. Tybell, P. Paruch, T. Giamarchi, J. Triscone. Domain wall creep in epitaxial ferroelectric $Pb(Zr_{0.2}Ti_{0.8})O_3$ thin films. *Physical Review Letters,* **89,** 097601 (2002).

27 Y. Shin, I. Grinberg, I. Chen, A. M. Rappe. Nucleation and growth mechanism of ferroelectric domain-wall motion. *Nature,* **449,** 881 (2007).

28 R. Mehta, B. Silverman, J. Jacobs. Depolarization fields in thin ferroelectric films. *Journal of Applied Physics*, **44,** 3379 (1973).

29 A. Tagantsev, G. Gerra. Interface-induced phenomena in polarization response of ferroelectric thin films. *Journal of Applied Physics*, **100,** 051607 (2006).

30 T. Mitsui, S. Nomura, M. Adachi, J. Harada, T. Ikeda, E. Nakamura, E. Sawaguchi, T.Shigenari, Y. Shiozagi, J. Tatsuzaki, K. Toyoda, T. Yamada, K. Gesi, Y. Marita, M. Marutake, T. Shiosaki, K. Wakino. *Oxides, Landolt-Boernstein: Numerical Data and Functional Relationships in Science and Technology, Group III.* Springer (1981).

31 K. Rabe, M. Dawber, C. Lichtensteiger, C. Ahn, J. Triscone. Modern physics of ferroelectrics: Essential background. *Physics of Ferroelectrics, Topics in Applied Physics,* **105,** Springer (2007).

32 K. Rabe, C. Ahn, J. Triscone. *Physics of Ferroelectrics: A Modern Perspective.* Springer (2007).

33 A. Solomon. Thiourea, a new ferroelectric. *Physical Review,* **104,** 1191 (1956).

34 D. Bordeaux, J. Bornarel, A. Capiomont, J. Lajzerowicz-Bonneteau. New ferroelastic-ferroelectric compound: tanane. *Physical Review Letters,* **31,** 314 (1973).

35 G. Lipscomb, A. Garito, T. Wei. An apparent ferroelectric transition in an organic diacetylene solid. *Ferroelectrics,* **23,** 161 (1980).

36 Y. Tokunaga, N. Furukawa, H. Sakai, Y. Taguchi, T. Arima, Y. Tokura. Composite domain walls in a multiferroic perovskite ferrite. *Nature Materials,* **8,** 558 (2009).

37 T. Lottermoser, T. Lonkai, U. Amann, D. Hohlwein, J. Ihringer, M. Fiebig. Magnetic phase control by an electric field. *Nature,* **430,** 541 (2004).

38 J. Wang, J. Neaton, H. Zheng, V. Nagarajan, S. Ogale, B. Liu, D. Viehland, V. Vaithyanathan, D. Schlom, U. Waghmare, N. Spaldin, K. Rabe, M. Wuttig, R. Ramesh. Epitaxial $BiFeO_3$ Multiferroic Thin Film Heterostructures. *Science,* **299,** 1719 (2003).

39 R. Ramesh, N. Spaldin. Multiferroics: progress and prospects in thin films. *Nature Materials,* **6,** 21 (2007).

40 N. Hill. Why Are There so Few Magnetic Ferroelectrics? *Journal of Physical Chemistry B,* **104,** 6694 (2000).

41 T. Wu, M. Zurbuchen, S. Saha, R. Wang, S. Streiffer, J. Mitchell. Observation of magnetoelectric effect in epitaxial ferroelectric film/manganite crystal heterostructures. *Physical Review B,* **73,** 134416 (2006).

42 W. Eerenstein, M. Wiora, J. Prieto, J. Scott, N. Mathur. Giant sharp and persistent converse magnetoelectric effects in multiferroic epitaxial heterostructures. *Nature Materials,* **6,** 348 (2007).

43 H. Molegraaf, J. Hoffman, C. Vaz, S. Gariglio, D. van der Marel, C. Ahn, J. Triscone. Magnetoelectric Effects in Complex Oxides with Competing Ground States. *Advanced materials,* **21,** 3470 (2009).

44 V. Garcia, M. Bibes, L. Bocher, S. Valencia, F. Kronast, A. Crassous, X. Moya, S. Enouz-Vedrenne, A. Gloter, D. Imhoff, C. Deranlot, N. Mathur, S. Fusil, K. Bouzehouane, A. Barthélémy. Ferroelectric Control of Spin Polarization. *Science,* **327,** 1106 (2010).

45 N. Yamauchi. A metal-insulator-semiconductor (MIS) device using a ferroelectric polymer thin film in the gate insulator. *Japanese Journal of Applied Physics*, **25**, 590 (1986).

46 L. Malin, I. Stolichnov, N. Setter. Ferroelectric polymer gate on AlGaN/GaN heterostructures. *Journal of Applied Physics*, **102**, 114101 (2007).

47 J. Kim, B. Park, H. Ishiwara. Fabrication and electrical characteristics of metal-ferroelectric-semiconductor field effect transistor based on poly(vinylidene fluoride). *Japanese Journal of Applied Physics,* **47,** 8472 (2008).

48 A. Mardana, S. Ducharme, S. Adenwalla. Ferroelectric control of magnetic anisotropy. *Nano Letters,* **11,** 3862 (2011).

49 H. Kawai. Piezoelectricity of poly(vinylidene fluoride). *Japanese Journal of Applied Physics,* **8,** 975 (1969).

50 S. Ducharme, T. Reece, C. Othon, R. Rannow. Ferroelectric polymer Langmuir-Blodgett films for nonvolatile memory applications. *IEEE Transactions on Device and Materials Reliability,* **5,** 720 (2005).

51 S. Bauer, S. Bauer-Gogonea, M. Dansachmuller, G. Dennler, I. Graz, M. Kaltenbrunner, C. Keplinger, H. Reiss, N. Sariciftci, T. Singh, R. Schwodiauer. Piezoelectric polymers. *Materials Research Society Symposium Proceedings,* **889,** 0889 (2006).

52 R. Gysel. Polarization reversal in ferroelectric PVDF and PZT films. *EPFL Doctoral Thesis,* No. 4097 (2008).

53 A. Lovinger. Ferroelectric polymers. *Science,* **220,** 1115 (1983).

54 M. Li, H. Wondergem, M. Spijkman, K. Asadi, I. Katsouras, P. Blom, D. de Leeuw. Revisiting the δ-phase of poly(vinylidene fluoride) for solution-processed ferroelectric thin films. *Nature Materials,* **12,** 433 (2013).

55 K. Tashiro. Crystal structure and phase transition of PVDF and related copolymers. *Ferroelectric Polymers*. Marcel Dekker Inc. (1995).

56 R. Hasegawa, Y. Takahash, H. Tadokoro, Y. Chatani. Crystal-structures of 3 crystalline forms of poly(vinylidene fluoride). *Polymer Journal,* **3,** 600 (1972).

57 N. Karasawa, W. Goddard III. Force fields, structures, and properties of poly(vinylidene fluoride) crystals. *Macromolecules,* **25,** 7268 (1992).

58 T. Furukawa. Ferroelectric properties of vinylidene fluoride copolymers. *Phase Transitions,* **18,** 143 (1989).

59 K. Koga, H. Ohigashi. Piezoelectricity and related properties of vinylidene fluoride and trifluoroethylene copolymers. *Journal of Applied Physics,* **59,** 2142 (1986).

60 K. Noda, K. Ishida, T. Horiuchi, K. Matsushige, A. Kubono. Structures of vinylidene fluoride oligomer thin films on alkali halide substrate. *Journal of Applied Physics,* **86,** 3688 (1999).

61 K. Noda, K. Ishida, A. Kubono, T. Horiuchi, H. Yamada, K. Matsushige. Structures and ferroelectric natures of epitaxially grown vinylidene fluoride oligomer thin films. *Japanese Journal of Applied Physics,* **39,** 6358 (2000).

62 T. Karaki, I. Chou, L. Cross. Electron-irradiation induced phase transition in poly(vinylidene fluoride-trifluoroethylene) copolymer. *Japanese Journal of Applied Physics,* **39,** 5668 (2000).

63 V. Bharti, Q. Zhang. Dielectric study of the relaxor ferroelectric poly(vinylidene fluoride-trifluoroethylene) copolymer system. *Physical Review B,* **63,** 184103

(2001).

64 C. Othon, S. Ducharme. Electron irradiation effects on the switching behavior of a ferroelectric polymer. *Ferroelectrics,* **304,** 9 (2004).

65 H. Dvey-Aharon, T. Sluckin, P. Taylor, A. Hopfinger. Kink propagation as a model for poling in poly(vinylidene fluoride). *Physical Review B,* **21,** 3700 (1980).

66 A. Salimi, A. Yousefi. FTIR studies of beta-phase crystal formation in stretched PVDF films. *Polymer Testing,* **22,** 699 (2003).

67 T. Hattori, M. Kanaoka, H. Ohigashi. Improved piezoelectricity in thick lamellar beta-form crystals of poly(vinylidene fluoride) crystallized under high pressure. *Journal of Applied Physics,* **79,** 2016 (1996).

68 J. Zheng, A. He, J. Li, C. Han. Polymorphism control of poly(vinylidene fluoride) through electrospinning. *Macromolecular Rapid Communications,* **28,** 2159 (2007).

69 A. Gradys, P. Sajkiewicz, S. Adamovsky, A. Minakov, C. Schick. Crystallization of poly(vinylidene fluoride) during ultra-fast cooling. *Thermochimica Acta,* **461,** 153 (2007).

70 V. Sencadas, R. Gregorio Filho, S. Lanceros-Méndez. Processing and characterization of a novel nonporous poly(vinylidene fluoride) films in the β phase. *Journal of Non-Crystalline Solids,* **352,** 2226 (2006).

71 H. Ye, W. Shao, L. Zhen. Crystallization kinetics and phase trans-formation of poly(vinylidene fluoride) films incorporated with functionalized $BaTiO_3$ nanoparticles. *Journal of Applied Polymer Science,* **129,** 2940 (2013).

72 D. Mandal, K. Kim, J. Lee. Simple synthesis of palladium nanoparticles, beta-phase formation, and the control of chain and dipole orientations in palladium-doped poly(vinylidene fluoride) thin films. *Langmuir,* **28,** 10310 (2012).

73 T. Wang, J. Herbert, A. Glass. *The Applications of Ferroelectric Polymers.* Blackie (1988).

74 P. Martinsa, A. Lopesa, S. Lanceros-Mendez. Electroactive phases of poly(vinylidene fluoride): Determination, processing and applications. *Progress in Polymer Science,* **39,** 683 (2014).

75 T. Furukawa, G. Johnson, H. Bair, Y. Tajitsu, A. Chiba, E. Fukada. Ferroelectric phase transition in a copolymer of vinylidene fluoride and trifluoroethylene. *Ferroelectrics,* **32,** 61 (1981).

76 T. Yagi, M. Tatemoto, J. Sako. Transition behavior and dielectric properties in trifluoroethylene and vinylidene fluoride copolymers. *Polymer Journal,* **12,** 209 (1980).

77 Y. Tajitsu, A. Chiba, T. Furukawa, M. Date, E. Fukada. Crystalline phase transition in the copolymer of vinylidenefluoride and trifluoroethylene. *Applied*

Physics Letters, **36,** 286 (1980).

78 S. Ducharme, S. Palto, V. Fridkin. Ferroelectric polymer Langmuir-Blodgett films. *Ferroelectric and Dielectric Thin Films,* Chapter 3. Academic Press (2002).

79 A. Kolmogorov. *Izv. Akad. Nauk, Ser. math.,* **3,** 355 (1937).

80 M. Avrami. Kinetics of phase change. I General theory. *Journal of Chemical Physics,* **7,** 1103 (1939).

81 R. Gysel, I. Stolichnov, A. Tagantsev, N. Setter, P. Mokrý. Restricted domain growth and polarization reversal kinetics in ferroelectric polymer thin films. *Journal of Applied Physics,* **103,** 084120 (2008).

82 P. Sharma, T. Reece, S. Ducharme, A. Gruverman. High-resolution studies of domain switching behavior in nanostructured ferroelectric polymers. *Nano Letters,* **11,** 1970 (2011).

83 S. Lim, A. Rastogi, S. Desu. Electrical properties of metal-ferroelectric-insulator-semiconductor structures based on ferroelectric polyvinylidene fluoride copolymer film gate for nonvolatile random access memory application. *Journal of Applied Physics,* **96,** 5673 (2004).

84 T. Reece, S. Ducharme, A. Sorokin, M. Poulsen. Non-volatile memory element based on a ferroelectric polymer Langmuir-Blodgett film. *Applied Physics Letters,* **82,** 142 (2003).

85 R. Naber, K. Asadi, P. Blom, D. de Leeuw, B. de Boer. Organic nonvolatile memory devices based on ferroelectricity. *Advanced materials,* **22,** 933 (2010).

86 K. Asadi, D. de Leeuw, B. de Boer, P. Blom. Organic non-volatile memories from ferroelectric phase-separated blends. *Nature Materials,* **7,** 547 (2008).

87 Y. Yuan, T. Reece, P. Sharma, S. Poddar, S. Ducharme, A. Gruverman, Y. Yang J. Huang. Efficiency enhancement in organic solar cells with ferroelectric polymers. *Nature Materials,* **10,** 296 (2011).

88 I. Ross. Semiconductive translating device. U.S. patent #2,791,760 (1957).

89 J. Moll, Y. Tarui. A new solid state memory resistor. *IEEE Transactions on Electron Devices,* **10,** 338 (1963).

90 S. Wu. A new ferroelectric memory device, metal-ferroelectric-semiconductor transistor. *IEEE Transactions on Electron Devices,* **21,** 499 (1974).

91 T. Rabson, T. Rost, H. Lin. Ferroelectric gate transistors. *Integrated Ferroelectrics,* **6,** 15 (1995).

92 S. Sinharoy, D. Lampe, H. Buhay, M. Francombe. UHV processing of ferroelectric barium magnesium fluoride films and devices. *Integrated Ferroelectrics,* **2,** 377 (1992).

93 S. Mathews, R. Ramesh, T. Venkatesan, J. Benedetto. Ferroelectric field effect

transistor based on epitaxial perovskite heterostructures. *Science,* **276,** 238 (1997).

94 H. Ishiwara. Recent progress of FET-type ferroelectric memories. *Integrated Ferroelectrics,* **34,** 1451 (2001).

95 I. Grekhov, L. Delimova, I. Liniichuk, D. Mashovets, I. Veselovsky. Strongly Modulated Conductance in Ag/PLZT/LSCO Ferroelectric Field-Effect Transistor. *Ferroelectrics,* 286 (2003).

96 J. Scott. New developments on FRAMs: [3D] structures and all-perovskite FETs. *Materials Science and Engineering B,* **120,** 6 (2005).

97 S. Sakai, M. Takahashi. Recent Progress of Ferroelectric-Gate Field-Effect Transistors and Applications to Nonvolatile Logic and FeNAND Flash Memory. *Materials,* **3,** 4950 (2010).

98 S. Yoon, H. Ishiwara. Memory operations of 1T2C-type ferroelectric memory cell with excellent data retention characteristics. *IEEE Transactions on Electron Devices,* **48,** 2002 (2001).

99 H. Cho, F. Nemati, R. Roy, R. Gupta, K. Yang, M. Ershov, S. Banna, M. Tarabbia, C. Sailing, D. Hayes, A. Mittal, S. Robins. A novel capacitor-less DRAM cell using thin capacitively-coupled thyristor (TCCT). *IEEE international electron devices meeting 2005, technical digest,* 311 (2005).

100 A. Gerber, M. Fitsilis, R. Waser, Timothy J. Reece, E. Rije, S. Ducharme, H. Kohlstedt. Ferroelectric field effect transistors using very thin ferroelectric polyvinylidene fluoride copolymer films as gate dielectrics. *Journal of Applied Physics,* **107,** 124119 (2010).

101 T. Reece, A. Gerber, H. Kohlstedt, S. Ducharme. Investigation of state retention in metal-ferroelectric-insulator-semiconductor structures based on Langmuir-Blodgett copolymer films. *Journal of Applied Physics,* **108,** 024109 (2010).

102 R. Gysel, I. Stolichnov, A. Tagantsev, S. Riester, N. Setter, G. Salvatore, D. Bouvet, A. Ionescu. Retention in nonvolatile silicon transistors with an organic ferroelectric gate. *Applied Physics Letters,* **94,** 263507 (2009).

103 S. Raghavan, I. Stolichnov, N. Setter, J. Heron, M. Tosun, A. Kis. Long-term retention in organic ferroelectric-graphene memories. *Applied Physics Letters,* **100,** 023507 (2012).

104 R. Naber, C. Tanase, P. Blom, G. H. Gelinck, A. Marsman, F. Touwslager, S. Setayesh, D. de Leeuw. High performance solution-processed polymer ferroelectric field-effect transistors. *Nature Materials,* **4,** 243 (2005).

105 M. Baibich, J. Broto, A. Fert, F. van Dau, F. Petroff, P. Etienne, G. Creuzet, A. Friederich, J. Chazelas. Giant magnetoresistance of (001)Fe/(001)Cr magnetic superlattices. *Physical Review Letters,* **61,** 2472 (1988).

106 P. Grünberg, R. Schreiber, Y. Pang, M. Brodsky, H. Sowers. Layered magnetic

structures: Evidence for antiferromagnetic coupling of Fe layers across Cr interlayers. *Physical Review Letters,* **57,** 2442 (1986).

107 P. Tannenwald, M. Seavey. Ferromagnetic Resonance in Thin Films of Permalloy. *Physical Review,* **105,** 377 (1957).

108 H. Wieder. Electrical and galvanomagnetic measurements on thin films and epilayers. *Thin Solid Films,* **31,** 123 (1976).

109 T. Gerrits, H. van den Berg, J. Hohlfeld, L. Bär, T. Rasing. Ultrafast precessional magnetization reversal by picosecond magnetic field pulse shaping. *Nature,* **418,** 509 (2002).

110 C. Kittle. *Introduction to Solid State Physics.* Wiley (2005).

111 A. Morrish. *The Physical Principles of Magnetism.* Wiley (1965).

112 L. Lévy. *Magnetism and superconductivity.* Springer (2000).

113 S. Riester. Ferroelectric polymer gates for persistent field effect control of ferromagnetism in (Ga, Mn)As layers. *EPFL Doctoral Thesis,* No. 4886 (2010).

114 K. Kopitzki, P. Herzog. *Einführung in die Festkörperphysik.* B. G. Teubner (2004).

115 T. Dietl, H. Ohno, F. Matsukura, J. Cibert, D. Ferrand. Zener model de- scription of ferromagnetism in zinc-blende magnetic semiconductors. *Science,* **287,** 1019 (2000).

116 T. Dietl, A. Haury, Y. d'Aubigne. Free carrier-induced ferromagnetism in structures of diluted magnetic semiconductors. *Physical Review B,* **55,** R3347 (1997).

117 C. Zener. Interaction between the d-shells in the transition metals. *Physical Review,* **81,** 440 (1951).

118 S. Blugel. Two-dimensional ferromagnetism of 3d, 4d, and 5d transition metal monolayers on noble metal (001) substrates. *Physical Review Letters,* **68,** 851 (1992).

119 B. Cullity. *Introduction to Magnetic Materials.* Addison-Wesley Publishing Company (1972).

120 P. Metaxas, J. Jamet, A. Mougin, M. Cormier, J. Ferré, V. Baltz, B. Rodmacq, B. Dieny, R. Stamps. Creep and Flow Regimes of Magnetic Domain-Wall Motion in Ultrathin Pt/Co/Pt Films with Perpendicular Anisotropy. *Physical Review Letters,* **99,** 217208 (2007).

121 N. Schryer, L. Walker. The motion of 180° domain walls in uniform dc magnetic fields. *Journal of Applied Physics,* **45,** 5406 (1974).

122 P. Chauve, T. Giamarchi, P. Le Doussal. Creep and depinning in disordered media. *Physical Review B,* **62,** 6241 (2000).

123 W. Thomson. On the electro-dynamic qualities of metals: Effects of magnetization

on the electric conductivity of nickel and iron. *Proceedings of the Royal Society,* **8,** 546 (1857).

124 K. Vyborny, J. Kucera, J. Sinova, A. W. Rushforth, B. Gallagher, T. Jungwirth. Microscopic mechanism of the noncrystalline anisotropic magnetoresistance in (Ga,Mn)As. *Physical Review B,* **80,** 165204 (2009).

125 T. McGuire, R. Potter. Anisotropic magnetoresistance in ferromagnetic 3d alloys. *IEEE Transactions on Magnetics,* **11,** 4 (1975).

126 A. Malozemoff. Anisotropic magnetoresistance of amorphous and concentrated polycrystalline iron-alloys. *Physical Review B,* **32,** 9 (1985).

127 O. Jaoul, I. Campbell, A. Fert. Spontaneous resistivity anisotropy in Ni alloys. *Journal of Magnetism and Magnetic Materials,* **5,** 23 (1977).

128 D. Baxter, D. Ruzmetov, J. Scherschligt, Y. Sasaki, X. Liu, J. Furdyna, C. Mielke. Anisotropic magnetoresistance in $Ga_{1-x}Mn_xAs$. *Physical Review B,* **65,** 21 (2002).

129 M. Weisheit, S. Fähler, A. Marty, Y. Souche, C. Poinsignon, D. Givord. Electric field-induced modification of magnetism in thin-film ferromagnets. *Science,* **315,** 349 (2007).

130 T. Maruyama, Y. Shiota, T. Nozaki, K. Ohta, N. Toda, M. Mizuguchi, A. Tulapurkar, T. Shinjo, M. Shiraishi, S. Mizukami, Y. Ando, Y. Suzuki. Large voltage-induced magnetic anisotropy change in a few atomic layers of iron. *Nature Nanotechnology,* **4,** 158 (2009).

131 J. Coey, M. Viret, S. von Molnár. Mixed-valence manganites. *Advances in Physics,* **48,** 167 (1999).

132 T. Dietl. Ferromagnetic semiconductors. *Semiconductor Science and Technology*, **17,** 377 (2002).

133 H. Ohno. Making nonmagnetic semiconductors ferromagnetic. *Science,* **281,** 951 (1998).

134 J. Blinowski, P. Kacman. Spin interactions of interstitial Mn ions in ferromagnetic GaMnAs. *Physical Review B,* **67,** R121204 (2003).

135 F. Maca, J. Masek. Electronic states in $Ga_{1-x}Mn_xAs$: Substitutional versus interstitial position of Mn. *Physical Review B,* **65,** 235209 (2002).

136 K. Yu, W. Walukiewicz, T. Wojtowicz, I. Kuryliszyn, X. Liu, Y. Sasaki, J. Furdyna. Effect of the location of Mn sites in ferromagnetic $Ga_{1-x}Mn_xAs$ on its Curie temperature. *Physical Review B,* **65,** R201303 (2002).

137 A. Macdonald, P. Schiffer, N. Samarth. Ferromagnetic semiconductors: moving beyond (Ga,Mn)As. *Nature Materials,* **4,** 195 (2005).

138 K. Wang, K. Edmonds, R. Campion, B. Gallagher, N. Farley, C. Foxon, M. Sawicki, P. Boguslawski, T. Dietl. Influence of the Mn interstitial on the magnetic and transport properties of (Ga,Mn)As. *Journal of Applied Physics,* **95,** 6512 (2004).

139 F. Matsukura, A. Shen, Y. Sugawara, T. Omiya, Y. Ohno, H. Ohno, *Compound Semiconductors 1998,* Chapter 10. IOP Conference Series (1999).

140 B. Sørensen, J. Sadowski, S. Andresen, P. Lindelof. Dependence of Curie temperature on the thickness of epitaxial (Ga,Mn)As film. *Physical Review B,* **66,** 233313 (2002).

141 M. Sawicki, D. Chiba, A. Korbecka, Y. Nishitani, J. Majewski, F. Matsukura, T. Dietl, H. Ohno. Experimental probing of the interplay between ferromagnetism and localization in (Ga, Mn)As. *Nature Physics,* **6,** 22 (2010).

142 I. Stolichnov, S. Riester, E. Mikheev, N. Setter, A. Rushforth, K. Edmonds, R. Campion, C. Foxon, B. Gallagher, T. Jungwirth, H. Trodahl. Enhanced Curie temperature and nonvolatile switching of ferromagnetism in ultrathin (Ga,Mn)As channels. *Physical Review B,* **83,** 115203 (2011).

143 Y. Nishitani, D. Chiba, M. Endo, M. Sawicki, F. Matsukura, T. Dietl, H. Ohno. Curie temperature versus hole concentration in field-effect structures of $Ga_{1-x}Mn_xAs$. *Physical Review B,* **81,** 045208 (2010).

144 M. Fisher, A. Ferdinand. Interfacial, boundary, and size effects at critical points. *Physical Review Letters,* **19,** 169 (1967).

145 A. Ferdinand, M. Fisher. Bounded and Inhomogeneous Ising Models. I. Specific-Heat Anomaly of a Finite Lattice. *Physical Review,* **185,** 832 (1969).

146 G. Allan. Critical Temperatures of Ising Lattice Films. *Physical Review B,* **1,** 352 (1970).

147 M. Fisher, M. Barber. Scaling Theory for Finite-Size Effects in the Critical Region. *Physical Review Letters,* **28,** 1516 (1972).

148 C. Schneider, P. Bressler, P. Schuster, J. Kirschner, J. de Miguel, R. Miranda. Curie temperature of ultrathin films of fcc-cobalt epitaxially grown on atomically flat Cu(100) surfaces. *Physical Review Letters,* **64,** 1059 (1990).

149 Z. Huang, I. Stolichnov, A. Bernand-Mantel, J. Borrel, S. Auffret, G. Gaudin, O. Boulle, S. Pizzini, L. Ranno, L. Herrera-Diez, N. Setter. Ferroelectric control of magnetic domains in ultra-thin cobalt layers. *Applied Physics Letters,* **103,** 222902 (2013).

150 S. Matar, A. Houari, M. Belkhir. *Ab initio* studies of magnetic properties of cobalt and tetracobalt nitride Co_4N. *Physical Review B,* **75,** 245109 (2007).

151 O. Sipr, S. Bornemann, J. Minar, S. Polesya, V. Popescu, A. Simunek, H. Ebert. Magnetic moments, exchange coupling, and crossover temperatures of Co clusters on Pt(111) and Au(111). *Journal of Physics: Condensed Matter,* **19,** 096203 (2007).

152 H. Munekata, H. Ohno, S. von Molnar, A. Segmüller, L. Chang, L. Esaki. Diluted magnetic III-V semiconductors. *Physical Review Letters,* **63,** 1849 (1989).

153 A. Shen, H. Ohno, F. Matsukura, Y. Sugawara, N. Akiba, T. Kuroiwa, A. Oiwa, A. Endo, S. Katsumoto, Y. Iye. Epitaxy of (Ga,Mn)As, a new diluted magnetic semiconductor based on GaAs. *Journal of Crystal Growth,* **175/176,** 1069 (1997).

154 A. Rushforth, M. Wang, N. Farley, R. Campion, K. Edmonds, C. Staddon, C. Foxon, B. Gallagher. Molecular beam epitaxy grown (Ga,Mn)(As,P) with perpendicular to plane magnetic easy axis. *Journal of Applied Physics,* **104,** 073908 (2008).

155 A. Lemaître, A. Miard, L. Travers, O. Mauguin, L. Largeau, C. Gourdon, V. Jeudy, M. Tran, J. George. Strain control of the magnetic anisotropy in (Ga,Mn)(As,P) ferromagnetic semiconductor layers. *Applied Physics Letters,* **93,** 021123 (2008).

156 A. Casiraghi, A. Rushforth, M. Wang, N. Farley, P. Wadley, J. Hall, C. Staddon, K. Edmonds, R. Campion, C. Foxon, B. Gallagher. Tuning perpendicular magnetic anisotropy in (Ga,Mn)(As,P) by thermal annealing. *Applied Physics Letters,* **97,** 122504 (2010).

157 P. Gambardella, S. Rusponi, M. Veronese, S. Dhesi, C. Grazioli, A. Dallmeyer, I. Cabria, R. Zeller, P. Dederichs. Giant magnetic anisotropy of single cobalt atoms and nanoparticles. *Science,* **300,** 1130 (2003).

158 C. Chappert , P. Bruno. Magnetic anisotropy in metallic ultrathin films and related experiments on cobalt films. *Journal of Applied Physics,* **64,** 5736 (1988).

159 R. O’Handley. *Modern magnetic materials: principles and applications.* Wiley (2000).

160 S. Monso, B. Rodmacq, S. Auffret, G. Casali, F. Fettar, B. Gilles, B. Dieny, P. Boyer. Crossover from in-plane to perpendicular anisotropy in Pt/CoFe/AlO_x sandwiches as a function of Al oxidation: A very accurate control of the oxidation of tunnel barriers. *Applied Physics Letters,* **80,** 4157 (2002).

161 B. Rodmacq, S. Auffret, B. Dieny, S. Monso, P. Boyer. Crossovers from in-plane to perpendicular anisotropy in magnetic tunnel junctions as a function of the barrier degree of oxidation. *Journal of Applied Physics,* **93,** 7513 (2003).

162 I. Oleinik, E. Yu. Tsymbal, D. Pettifor. Structural and electronic properties of Co/Al_2O_3/Co magnetic tunnel junction from first principles. *Physical Review B,* **62,** 3952 (2000).

163 K. Belashchenko, E. Tsymbal, I. Oleynik, M. van Schilfgaarde. Positive spin polarization in Co/Al_2O_3/Co tunnel junctions driven by oxygen adsorption. *Physical Review B,* **71,** 224422 (2005).

164 P. Bruno. Tight-binding approach to the orbital magnetic moment and magnetocrystalline anisotropy of transition-metal monolayers. *Physical Review B,* **39,** 865(R) (1989).

165 A. Manchon, C. Ducruet, L. Lombard, S. Auffret, B. Rodmacq, B. Dieny, S.

Pizzini, J. Vogel, V. Uhlíř, M. Hochstrasser, G. Panaccione. Analysis of oxygen induced anisotropy crossover in Pt/Co/MO_x trilayers. *Journal of Applied Physics,* **104,** 043914 (2008).

166 E. de Ranieri, A. Rushforth, K. Výborný, U. Rana, E. Ahmad, R. Campion, C. Foxon, B. Gallagher, A. Irvine, J. Wunderlich, T. Jungwirth. Lithographically and electrically controlled strain effects on anisotropic magnetoresistance in (Ga,Mn)As. *New Journal of Physics,* **10,** 065003 (2008).

167 T. Jungwirth, Jairo Sinova, J. Mašek, J. Kučera, A. MacDonald. Theory of ferromagnetic (III,Mn)V semiconductors. *Reviews of Modern Physics,* **78,** 809 (2006).

168 T. Jungwirth, M. Abolfath, J. Sinova, J. Kucera, A. MacDonald. Boltzmann theory of engineered anisotropic magnetoresistance in (Ga,Mn)As. *Applied Physics Letters,* **81,** 4029 (2002).

169 A. Rushforth, K. Výborný, C. King, K. Edmonds, R. Campion, C. Foxon, J. Wunderlich, A. Irvine, P. Vašek, V. Novák, K. Olejník, J. Sinova, T. Jungwirth, B. Gallagher. Anisotropic Magnetoresistance Components in (Ga,Mn)As. *Physical Review Letters,* **99,** 147207 (2007).

170 A. Rushforth, K. Vyborny, C. King, K. Edmonds, R. Campion, C. Foxon, J. Wunderlich, A. Irvine, V. Novak, K. Olejnik, A. Kovalev, J. Sinova, T. Jungwirth, B. Gallagher. The origin and control of the sources of AMR in (Ga,Mn)As devices. *Journal of Magnetism and Magnetic Materials,* **321,** 1001 (2009).

171 A. Kobs, S. Heße, W. Kreuzpaintner, G. Winkler, D. Lott, P. Weinberger, A. Schreyer, H. Oepen. Anisotropic Interface Magnetoresistance in Pt/Co/Pt Sandwiches. *Physical Review Letters,* **106,** 217207 (2011).

172 H. Ohno, D. Chiba, F. Matsukura, T. Omiya, E. Abe, T. Dietl, Y. Ohno, K. Ohtani. Electric-field control of ferromagnetism. *Nature,* **408,** 944 (2000).

173 D. Chiba, F. Matsukura, H. Ohno. Electric-field control of ferromagnetism in (Ga,Mn)As. *Applied Physics Letters,* **89,** 162505 (2006).

174 D. Chiba, M. Sawicki, Y. Nishitani, Y. Nakatani, F. Matsukura, H. Ohno. Magnetization vector manipulation by electric fields. *Nature,* **455,** 515 (2008).

175 T. Dietl, H. Ohno, F. Matsukura. Hole-mediated ferromagnetism in tetrahedrally coordinated semiconductors. *Physical Review B,* **63,** 195205 (2001).

176 M. Endo, S. Kanai, S. Ikeda, F. Matsukura, H. Ohno. Electric-field effects on thickness dependent magnetic anisotropy of sputtered MgO/$Co_{40}Fe_{40}B_{20}$/Ta structures. *Applied Physics Letters,* **96,** 212503 (2010).

177 D. Chiba, M. Yamanouchi, F. Matsukura, H. Ohno. Electrical manipulation of magnetization reversal in a ferromagnetic semiconductor. *Science,* **301,** 943 (2003).

178 M. Overby, A. Chernyshov, L. Rokhinson, X. Liu, J. Furdyna. GaMnAs based hybrid multiferroic memory device. *Applied Physics Letters,* **92,** 192501 (2008).

179 D. Chiba, S. Fukami, K. Shimamura, N. Ishiwata, K. Kobayashi, T. Ono. Electrical control of the ferromagnetic phase transition in cobalt at room temperature. *Nature Materials,* **10,** 853 (2011).

180 L. Onsager. Crystal statistics. I. A two-dimensional model with an order-disorder transition. *Physical Review,* **65,** 117 (1944).

181 S. Bramwell, P. Holdsworth. Magnetization and universal sub-critical behaviour in two-dimensional XY magnets. *Journal of Physics: Condensed Matter,* **5,** L53 (1993).

182 M. Wutting, X. Liu. *Ultrathin Metal Films.* Springer (2004).

183 K. Shimamura, D. Chiba, S. Ono, S. Fukami, N. Ishiwata, M. Kawaguchi, K. Kobayashi, T. Ono. Electrical control of Curie temperature in cobalt using an ionic liquid film. *Applied Physics Letters,* **100,** 122402 (2012).

184 M. Susan, T. Kaneko, A. Noda, M. Watanabe. Ion Gels Prepared by in Situ Radical Polymerization of Vinyl Monomers in an Ionic Liquid and Their Characterization as Polymer Electrolytes. *Journal of the American Chemical Society,* **127,** 4976 (2005).

185 D. Chiba, M. Kawaguchi, S. Fukami, N. Ishiwata, K. Shimamura, K. Kobayashi, T. Ono. Electric-field control of magnetic domain-wall velocity in ultrathin cobalt with perpendicular magnetization. *Nature Communications,* **3,** 888 (2012).

186 A. Schellekens, A. van den Brink, J. Franken, H. Swagten, B. Koopmans. Electric-field control of domain wall motion in perpendicularly magnetized materials. *Nature Communications,* **3,** 847 (2012).

187 J. Franken, Y. Yin, A. Schellekens, A. van den Brink, H. Swagten, B. Koopmans. Voltage-gated pinning in a magnetic domain-wall conduit. *Applied Physics Letters,* **103,** 102411 (2013).

188 S. Parkin, H. Masamitsu, L. Thomas. Magnetic domain-wall racetrack memory. *Science,* **320,** 190 (2008).

189 A. Bernand-Mantel, L. Herrera-Diez, L. Ranno, S. Pizzini, J. Vogel, D. Givord, S. Auffret, O. Boulle, I. Miron, G. Gaudin. Electric-field control of domain wall nucleation and pinning in a metallic ferromagnet. *Applied Physics Letters,* **102,** 122406 (2013).

190 A. van Esch, L. van Bockstal, J. de Boeck, G. Verbanck, A. van Steenbergen, P. Wellmann, B. Grietens, R. Bogaerts, F. Herlach, G. Borghs. Interplay between the magnetic and transport properties in the III-V diluted magnetic semiconductor $Ga_{1-x}Mn_xAs$. *Physical Review B,* **56,** 13103 (1997).

191 I. Stolichnov, S. Riester, H. Trodahl, N. Setter, A. Rushforth, K. Edmonds, R. Campion, C. Foxon, B. Gallagher, T. Jungwirth. Non-volatile ferroelectric control of ferromagnetism in (Ga,Mn)As. *Nature Materials*, **7,** 464 (2008).

192 I. Stolichnov, S. Riester, E. Mikheev, N. Setter, A. Rushforth, K. Edmonds, R. Campion, C. Foxon, B. Gallagher, T. Jungwirth, H. Trodahl. Ferroelectric polymer

gates for non-volatile field effect control of ferromagnetism in (Ga,Mn)As layers. *Nanotechnology,* **24,** 254004 (2011).

193 S. Riester, I. Stolichnov, H. Trodahl, N. Setter, A. Rushforth, K. Edmonds, R. Campion, C. Foxon, B. Gallagher, T. Jungwirth. Toward a low-voltage multiferroic transistor: Magnetic (Ga,Mn)As under ferroelectric control. *Applied Physics Letters,* **94,** 063504 (2009).

194 A. Tolstousov, R. Gaynutdinov, R. Tadros-Morgane, S. Yudin, A. Tolstikhina, H. Kliem, S. Ducharme, V. Fridkin. Ferroelectric Properties of Langmuir-Blodgett Copolymer Films at the Nanoscale. *Ferroelectrics,* **354,** 99 (2007).

195 K. Olejník, M. Owen, V. Novák, J. Mašek, A. Irvine, J. Wunderlich, T. Jungwirth. Enhanced annealing, high Curie temperature, and low-voltage gating in (Ga,Mn)As: A surface oxide control study. *Physical Review B,* **78,** 054403 (2008).

196 E. Mikheev, S. Riester, I. Stolichnov. N. Setter. Polarization Screening in Multiferroic (Ga,Mn)As/P(VDF-TrFE) Transistors. *Ferroelectrics,* **421,** 98 (2011).

197 E. Mikheev, I. Stolichnov, E. de Ranieri, J. Wunderlich, H. Trodahl, A. Rushforth, S. Riester, R. Campion, K. Edmonds, B. Gallagher, N. Setter. Magnetic domain wall propagation under ferroelectric control. *Physical Review B,* **86,** 235130 (2012).

198 P. Lukashev, T. Paudel, J. Lopez-Encarnacion, S. Adenwalla, E. Tsymbal, J. Velev. Ferroelectric control of magnetocrystalline anisotropy at cobalt/poly(vinylidene-fluoride) interfaces*, ACS Nano,* **6,** 9745 (2012).

199 J. Hong, R. Wu, J. Lindner, E. Kosubek, K. Baberschke. Manipulation of Spin Reorientation Transition by Oxygen Surfactant Growth: A Combined Theoretical and Experimental Approach. *Physical Review Letters,* **92,** 147202 (2004).

200 B. Jaffe, W. Cook, H. Jaffe. *Piezoelectric Ceramics*. Academic Press (1971).

201 S. Miller, R. Nasby, J. Schwank, M. Rodgers, P. Dressendorfer. Device modeling of ferroelectric capacitors. *Journal of Applied Physics,* **68,** 6463 (1990).

202 J. Smit. The spontaneous hall effect in ferromagnetics. *Physica*, **21,** 877 (1955).

203 L. Berger. Side-jump mechanism for the Hall effect of ferromagnets. *Physical Review B-Solid State,* **2,** 11 (1970).

204 J. Kerr. On Rotation of the Plane of Polarization by Reflection from the Pole of a Magnet. *Philosophical Magazine,* **3,** 321 (1877).

205 S. Bader. SMOKE. *Journal of Magnetism and Magnetic Materials,* **100,** 440 (1991).

206 A. Manchon, C. Ducruet, L. Lombard, S. Auffret, B. Rodmacq, B. Dieny, S. Pizzini, J. Vogel, V. Uhlir, M. Hochstrasser, G. Panaccione, *Journal of Applied Physics,* **104,** 043914 (2008).

207 W. Kalb, T. Mathis, S. Haas, A. Stassen, B. Batlogg. Organic small molecule

field-effect transistors with Cytop^{TM} gate dielectric: Eliminating gate bias stress effects. *Applied Physics Letters,* **90,** 092104 (2007).

208 T. Ha, J. Lee, S. Chowdhury, D. Akinwande, P. Rossky, A. Dodabalapur. Transformation of the electrical characteristics of graphene field-effect transistors with fluoropolymer. *ACS Applied Materials and Interfaces,* **5,** 16 (2013).

209 F. Matsukura, H. Ohno, A. Shen, Y. Sugawara. Transport properties and origin of ferromagnetism in (Ga,Mn)As. *Physical Review B,* **57,** R2037 (1998).

210 S. Fujisaki, H. Ishiwara, Y. Fujisaki. Organic ferroelectric diodes with long retention characteristics suitable for non-volatile memory applications. *Applied Physics Express,* **1,** 081801 (2008).

211 Introduction of E-beam lithography system, part "Electrons, resist and substrates". CMI website: https://cmi.epfl.ch/ebeam/Electrons,_resists_and_substrates.php

212 G. Srinivasan, E. Rasmussen, B. Levin, R. Hayes. Magnetoelectric effects in bilayers and multilayers of magnetostrictive and piezoelectric perovskite oxides. *Physical Review B,* **65,** 134402 (2002).

213 E. Mikheev, I. Stolichnov, Z. Huang, A. Rushforth, J. Haigh, R. Campion, K. Edmonds, B. Gallagher, N. Setter. Non-volatile ferroelectric gating of magnetotransport anisotropy in (Ga,Mn)(As,P). *Applied Physics Letters,* **100,** 262906 (2012).

214 J. Mašek, J. Kudrnovský, F. Máca, J. Sinova, A. MacDonald, R. Campion, B.. Gallagher, T. Jungwirth. Mn-doped Ga(As,P) and (Al,Ga)As ferromagnetic semiconductors: Electronic structure calculations. *Physical Review B,* **75,** 045202 (2007).

215 M. Scarpulla, B. Cardozo, R. Farshchi, W. Oo, M. McCluskey, K. Yu, O. Dubon. Ferromagnetism in $Ga_{1-x}Mn_xP$: Evidence for inter-Mn exchange mediated by localized holes within a detached impurity band. *Physical Review Letters,* **95,** 207204 (2005).

216 F. Matsukura, M. Sawicki, T. Dietl, D. Chiba, H. Ohno. Magnetotransport properties of metallic (Ga,Mn)As films with compressive and tensile strain. *Physica E: Low-Dimensional Systems and Nanostructures,* **21,** 1032 (2004).

217 M. Owen, J. Wunderlich, V. Novak, K. Olejnik, J. Zemen, K. Vyborny, S. Ogawa, A. Irvine, A. Ferguson, H. Sirringhaus, T. Jungwirth. Low-voltage control of ferromagnetism in a semiconductor p-n junction. *New Journal of Physics,* **11,** 023008 (2009).

218 Y. Iye, A. Oiwa, A. Endo, S. Katsumoto, F. Matsukura, A. Shen, H. Ohno, H. Munekata. Metal-insulator transition and magnetotransport in III-V compound diluted magnetic semiconductors. *Materials Science and Engineering B-Solid State Materials for Advanced Technology,* **63,** 88, (1999).

219 K. Edmonds, R. Campion, K. Wang, A. Neumann, B. Gallagher, C. Foxon, P.

Main. Magnetoresistance and Hall effect in the ferromagnetic semiconductor $Ga_{1-x}Mn_xAs$. *Journal of Applied Physics,* **93,** 6787, (2003).

220 G. Xiang, N. Samarth. Theoretical analysis of the influence of magnetic domain walls on longitudinal and transverse magnetoresistance in tensile strained (Ga,Mn)As epilayers. *Physical Review B,***76,** 054440 (2007).

221 X. Cheng, S. Urazhdin, O. Tchernyshyov, C. Chien, V. Nikitenko, A. Shapiro, R. Shull. Antisymmetric magnetoresistance in magnetic multilayers with perpendicular anisotropy. *Physical Review Letters,* **94,** 017203 (2005).

222 H. Tang, M. Roukes. Electrical transport across an individual magnetic domain wall in (Ga,Mn)As microdevices. *Physical Review B,* **70,** 205213 (2004).

223 A. Aziz, S. Bending, H. Roberts, S. Crampin, P. Heard, C. Marrows. Angular dependence of domain wall resistivity in artificial magnetic domain structures. *Physical Review Letters,* **97,** 206602 (2006).

224 Supplementary information of the paper: Z. Huang, I. Stolichnov, A. Bernand-Mantel, J. Borrel, S. Auffret, G. Gaudin, O. Boulle, S. Pizzini, L. Ranno, L. Herrera-Diez, N. Setter. Ferroelectric control of magnetic domains in ultra-thin cobalt layers. *Applied Physics Letters,* **103,** 222902 (2013).

225 J. Vogel, J. Moritz , O. Fruchart. Nucleation of magnetisation reversal, from nanoparticles to bulk materials. *Comptes Rendus Physique,* **7,** 12 (2006).

226 A. Tagantsev, I. Stolichnov, N. Setter, J. Cross. Nature of nonlinear imprint in ferroelectric films and long-term prediction of polarization loss in ferroelectric memories. *Journal of Applied Physics,* **96,** 6616 (2004).

227 S. Lemerle, J. Ferre, C. Chappert, V. Mathet, T. Giamarchi, P. Le Doussal. Domain wall creep in an ising ultrathin magnetic film. *Physical Review Letters,* **80,** 849 (1998).

228 D. Kim, S. Yoo, D. Kim, K. Moon, S. Je, C. Cho, B. Min, S. Choe. Maximizing domain-wall speed via magnetic anisotropy adjustment in Pt/Co/Pt films. *Applied Physics Letters,* **104**, 142410 (2014).

Acknowledgement

I am deeply grateful to my supervisor, MER. Dr. Igor Stolichnov, for all his advices, support and guidance during my 4 years doctoral research. And my gratitude is also for his creation of an inspiring working environment, for numerous fruitful discussions, for his helps on the cooperation with other researchers, and for his efforts in reading and discussing my thesis manuscript.

I am thankful to my thesis co-director, Prof. Nava Setter, for offering me the opportunity to perform my PhD research in this academic-worldly famous laboratory after my bachelor degree directly.

I would like to thank the jury president and members for my thesis defense: Prof. William Curtin, Prof. Jan Petzlet, Prof. Jean-Philippe Ansermet and Dr. Roman Gysel.

I am thankful to Eugène Mikheev for passing his knowledge of multiferroics and the experimental skills. And it is a pleasure to work with Dr. Anne Bernand-Mantel (Institut Néel, CNRS, Grenoble), for her knowledge on the ferromagnetic thin films.

Many thanks to Nicolas Leiser for his support in the clean room of ICMP, Zdenek Benes for his industrious maintenance of E-beam lithography system, Laszlo Pethö for his support of photolithography techniques in CMi, and Laurent Ranno (Institut Néel, CNRS) for the enjoyable cooperation on the MOKE microscopy.

I would like to thank my officemate, Dr. Petr Yudin, for the interesting daily discussion and weekend activities. I would like to express my sincere thanks to all colleagues of the Ceramics Laboratory for the productive work environment.

I am thankful to my friends around, making my life much happier. I really enjoy all the cooking, hiking and skiing days and the shared memories. I gratefully thank all of them: Li Jin, Yan Yan, Jin Wang, Shuangyi Zhao, Zhaolu Diao, Hui Yang, Liang Qiao, Hongyan Bi, Haiqiang Deng, Yu Lu, Cheng Yu, Peiyu Ge, Han Wu, Ji Cao, Shenqi Xie, Changru Ma, Ye Lou, Jianping Cheng, Qiang Lan, Rui Du, Xiaoyun Yu, Zongzhao Zhai, Chaobo Huang, Chen Yan, Kuang-Yu Yang, Yinong Lin, Qiuda Gu, Chien-Yi Wang, Yen-Cheng Kung, Ming-Wei Chen, Yingdi Zhu, Xiaoqin Zhong, Yan Deng, Tong Wu, Shiwei Zhou, *etc*

I express my gratitude to Tzu-En Lin, whose love and devotion make me brave and fulfilled.

Finally, I want to thank my parents for their unconditional support and everlasting our affection. Thank you!

Curriculum vitae

Zhen Huang

Date of birth: 07.08.1989

Place of birth: Wuhan (CHN)

Nationality: Chinese

Education

2007-2011	Peking University, Beijing, China Bachelor of Science in Physics

Academic Experience

2011-2015	Ceramics Laboratory, MER I. Stolichnov and Prof. N. Setter Doctoral School of Materials Science, EPFL, Lausanne, Switzerland PhD student
2009-2011	Nanostructure and low dimensional physics laboratory, Prof. D. Yu Peking University, Beijing, China Student researcher

Publications

1. Z. Huang, I. Stolichnov, A. Bernand-Mantel, J. Borrel, S. Auffret, G. Gaudin, O. Boulle, S. Pizzini, L. Ranno, L. Herrera-Diez, N. Setter. Ferroelectric control of magnetic domains in ultra-thin cobalt layers. *Applied Physics Letters,* **103,** 222902 (2013).
2. Z. Huang, I. Stolichnov, A. Bernand-Mantel, M. Schott, S. Auffret, G. Gaudin, S. Pizzini, L. Ranno, N. Setter. Non-volatile polarization switch of magnetic domain wall velocity. *Applied Physics Letters,* accepted on November 2015.
3. E. Mikheev, I. Stolichnov, Z. Huang, A. Rushforth, J. Haigh, R. Campion, K. Edmonds, B. Gallagher, N. Setter. Non-volatile ferroelectric gating of magnetotransport anisotropy in (Ga,Mn)(As,P). *Applied Physics Letters,* **100,** 262906 (2012).